



INSTITUTO  
SUPERIOR  
TÉCNICO

UNIVERSIDADE TÉCNICA DE LISBOA

INSTITUTO SUPERIOR TÉCNICO

# A Sparse Regression Approach to Hyperspectral Unmixing

Marian-Daniel Iordache

**Supervisor:** Doctor José Manuel Bioucas - Dias

**Co-supervisor:** Doctor Antonio J. Plaza

Thesis specifically prepared to obtain the PhD Degree in

Electrical and Computer Engineering

Draft

November 2011



# Abstract

Spectral unmixing is an important problem in hyperspectral data exploitation. It amounts at characterizing the mixed spectral signatures collected by an imaging instrument in the form of a combination of pure spectral constituents (endmembers), weighted by their correspondent abundance fractions. Linear spectral unmixing is a popular technique in the literature which assumes linear interactions between the endmembers, thus simplifying the characterization of the mixtures and approaching the problem from a general perspective independent of the physical properties of the observed materials. However, linear spectral unmixing suffers from several shortcomings. First, it is unlikely to find completely pure spectral endmembers in the image data due to spatial resolution and mixture phenomena. Second, the linear mixture model does not naturally include spatial information, which is an important source of information (together with spectral information) to solve the unmixing problem. In this thesis, we propose a completely new approach for spectral unmixing which makes use of spectral libraries of materials collected on the ground or in a laboratory, thus circumventing the problems associated to image endmember extraction. Due to the increasing availability and dimensionality of spectral libraries, this problem calls for efficient sparse regularizers. The resulting approach is called sparse unmixing, which represents a unique contribution of this research work and which opens a new direction in the field of spectral unmixing, which is a very active research topic in the hyperspectral image analysis literature. Another important contribution of this work is the inclusion of spatial information in sparse unmixing, which is achieved in this work by means of a Total Variation (TV) regularizer. In order to take advantage of the arrangement of spectral signatures in the form of groups of materials in available spectral libraries, the thesis also explores the use of sparse unmixing for groups of materials, resorting to the Sparse Group Lasso (SGL).

This technique focuses on obtaining sparse solutions for groups of signatures from the spectral library which correspond to the same type of materials, and not only with respect to the constituent endmembers of individual pixels. Finally, another innovative contribution of this thesis is the joint consideration of groups of pixels and groups of materials, using the Collaborative Hierarchical Lasso (CHL). Combined, these innovative contributions establish the field of sparse unmixing in hyperspectral analysis and offer a thoughtful perspective on the possibility of using sparse regression techniques in this context, leading to solutions to problems that could not be solved before in the context of linear spectral unmixing. The effectiveness of all the proposed techniques is illustrated by providing exhaustive comparisons with state-of-the-art methods for spectral unmixing using both simulated and real hyperspectral data sets.

**Keywords:**

Hyperspectral imaging, spectral unmixing, abundance estimation, sparse regression, convex optimization, total variation (TV), Sparse Group Lasso, Collaborative Hierarchical Lasso

# Resumo

Esta tese propõe técnicas para a separação de misturas hiperespectrais baseadas em regressão esparsa sobre bibliotecas espectrais. Tanto quanto o autor conhece, esta tese constitui a primeira abordagem à separação de misturas hiperespectrais usando regressão esparsa. Desenvolvem-se e testam-se com sucesso uma série de algoritmos rápidos de regressão esparsa baseados no método Alternating Direction Method of Multipliers (ADMM). Na ausência de uma biblioteca espectral, os métodos propostos podem ainda funcionar com assinaturas espectrais extraídas de imagem, tendo, assim, uma aplicabilidade de espectro largo. Para além da regressão esparsa convencional desenvolvem-se abordagens que exploram a informação espacial sempre presente nas imagens hiperespectrais, a esparsidade por grupos de materiais e a esparsidade colaborativa. Qualquer destas abordagens consiste na inclusão de regularizadores adequados na função objectivo a otimizar. Na informação espacial utiliza-se a variação total. Promovem-se, desta forma, soluções em que a pixels vizinhos correspondem soluções próximas. Na esparsidade por grupos utiliza-se uma norma mista  $\ell_{2,1}$  que promove a activação de grupos pré-definidos de materiais. Esta abordagem é motivada pelo facto das bibliotecas espectrais conterem, normalmente, grupos de assinaturas correspondentes a pequenas variações de um único material. Na esparsidade colaborativa utiliza-se uma norma mista  $\ell_{2,1}$  que promove a activação simultânea, isto é, em todos os pixels, de grupos pré-definidos de materiais. A motivação aqui é que numa dada imagem o conjunto de materiais activos é, normalmente, o mesmo em todos os pixels. A eficácia e o desempenho das técnicas propostas é documentada com base em comparações com o estado-da-arte usado dados simulados e reais.

## **Palavras-Chave:**

Imagem hiperespectral, separação espectral, estimação de abundância, regressão esparsa, otimização convexa, variação total, Sparse Group Lasso, Collaborative Hierarchical Lasso

# Acknowledgments

First of all, I would like to thank my supervisors, Professor José Manuel Bioucas Dias and Professor Antonio J. Plaza. On one hand, I thank them for their support, patience and friendship in all this years, and, on the other hand, for being great examples of professionalism and seriousness in the research activity. I feel lucky and grateful to have the opportunity to work with them.

I would like to thank from the bottom of my heart to Lumi, who was by my side all the time, encouraged me when I was on the right track and pushed me back on it every time when I was close to lose it.

I thank also my course professors from IST, for their dedication and for their effort in improving our knowledge: Professor Jorge Marques, Professor Mário Figueiredo, Professor João Xavier, and Professor Pedro Aguiar.

I am directing my best thoughts and sincere appreciation to the greatest friend that I could meet these years: José Marques Pais. For everything.

I thank Prof. Dumitru Stanciu, from Politehnica University of Bucharest, for his support and friendship and for being an example for me in everything. I am sending all my gratitude and appreciation to Prof. Daniel Ioan and to Prof. Gabriela Ciuprina from the Electrical Engineering Research Center (Bucharest, Romania), who guided my first steps on the exciting path of research.

For their kindness, friendship and the good times we spent together, I thank my colleagues from IST: Li, Manyá, André, João, Nuria, Gonçalo, Marta, Mariana, Rong, Liliana, Sónia, José Nascimento, David and my colleagues in HyperComp, UEX: Javier, Gabriel, Sergio, Inmaculada, Abel, Alberto, Maciel, Marta, Alessandro and all of the other colleagues I do not mention here who definitely deserve my sincere acknowledgments. The same thoughts are directed toward all

my friends from Romania and around the world, who are too many to be named here.

Last but not least, I would like to thank my family from Romania: my mother – Ioana, my father – Cristian, my sister – Irina, my brother-in-law – Elvis, my niece – Catalina, my nephew – Mihai, Buni and Nico. I thank all of them for being close to me, despite the distance that separated us, and for supporting me all the time.



*To Lumi*



# Table of Contents

<b>Chapter 1</b>	<b>Introduction</b>	<b>1</b>
1.1	Context and motivation	1
1.1.1	Context	1
1.1.2	Motivation	3
1.2	Thesis organization	8
1.3	The Main Contributions of the Thesis	12
<b>Chapter 2</b>	<b>Sparse Unmixing of Hyperspectral Data</b>	<b>15</b>
2.1	Introduction	16
2.2	Spectral Unmixing Reformulated as a sparse Regression Problem	23
2.2.1	Exact solutions	24
2.2.2	Approximate solutions	28
2.3	Algorithms	30
2.3.1	Orthogonal Matching Pursuit Algorithms	31
2.3.2	Basis Pursuit and Basis Pursuit Denoising Algorithms	32
2.3.3	Unconstrained Basis Pursuit and Basis Pursuit Denoising Algorithms	32
2.3.4	Iterative Spectral Mixture Analysis (ISMA)	34
2.4	Experiments with simulated data	35
2.4.1	Spectral Libraries Used in Simulated Data Experiments	36
2.4.2	Performance Discriminators	38
2.4.3	Calculation of Approximate Solutions Without Imposing the ASC Constraint	42
2.4.4	Comparison of Unmixing Algorithms with Regards to Computational Complexity	46
2.4.5	Comparison of Unmixing Algorithms in the Presence of Different Noise Levels	46
2.4.6	Calculation of Approximate Solutions Imposing the ASC Constraint	49
2.4.7	Application of sparse unmixing techniques to image-derived endmembers	53
2.4.8	Summary and Main Observations	55
2.5	Experiments with Real Data	57
2.6	Conclusions and Future Research	65
<b>Chapter 3</b>	<b>Total Variation Spatial Regularization for Sparse Hyperspectral Unmixing</b>	<b>71</b>
3.1	Introduction	72
3.2	Linear versus sparse unmixing	73
3.3	Total Variation for Sparse Unmixing – The SUnSAL-TV Algorithm	75
3.4	Experiments with simulated data	79
3.4.1	Simulated data sets	80
3.4.2	Results and discussion	81
3.5	Experiments with Real Data	94

3.6	Conclusions and future work . . . . .	99
<b>Chapter 4</b>	<b>Hyperspectral Unmixing with Sparse Group Lasso and Collaborative Hierarchical Lasso . . . . .</b>	<b>105</b>
4.1	Introduction . . . . .	106
4.2	Algorithms . . . . .	108
4.2.1	Group Sparse Regression . . . . .	108
4.2.2	Collaborative Hierarchical Sparse Regression . . . . .	109
4.2.3	Short illustration of the regularization processes . . . . .	110
4.3	Results with Synthetic Data . . . . .	110
4.3.1	Simulated datacubes . . . . .	112
4.3.2	Performance in datasets affected by white noise . . . . .	113
4.3.3	Performance in datasets affected by correlated noise . . . . .	115
4.3.4	Discussion . . . . .	116
4.4	Results with real data . . . . .	118
4.5	Conclusions and future work . . . . .	121
<b>Chapter 5</b>	<b>Conclusions and Future Work . . . . .</b>	<b>123</b>
	<b>Bibliography . . . . .</b>	<b>128</b>

# Chapter 1

## Introduction

### 1.1 Context and motivation

#### 1.1.1 Context

The work presented in this thesis was supported by the European Community's Marie Curie Research Training Networks Program under contract MRTN-CT-2006-035927 (Hyperspectral Imaging Network, HYPER-I-NET) and by the Spanish Ministry of Science and Innovation (HYPERCOMP/EODIX project, reference AYA2008-05965-C04-02). The HYPER-I-NET project has been awarded funding of 2.3 million Euro and supported 12 early-stage researchers and 5 experienced researchers, with the goal of creating a European network on hyperspectral imaging research and encouraging the mobility of young researchers working in this area across Europe. The consortium which carried out the HYPER-I-NET project along the four years of its duration (2007–2011) was formed by 15 partners from 12 European countries:

- University of Extremadura (UEX), Cáceres, SPAIN
- Instituto Superior Técnico (IST), Lisbon, PORTUGAL
- German Remote Sensing Data Center (DLR), Wessling, GERMANY
- Norwegian Defence Research Establishment (FFI), Kjeller, NORWAY
- Academy of Sciences of the Czech Republic (ISBE), Brno, CZECH REPUBLIC
- Kayser-Threde GmbH (KT), Munich, GERMANY

- Institut Natioanl Polytechnique de Grenoble (INPG), Grenoble, FRANCE
- Centre National de la Recherche Scientifique (CNRS), Nantes, FRANCE
- Norsk Electro Optikk AS (NEO), Lorenskog, NORWAY
- University of Zurich (UZH), Zurich, SWITZERLAND
- Spectral Imaginf Oy Ltd. (SPECIM), Oulu, FINLAND
- University of Pavia (UNIPV), Pavia, ITALY
- University of Iceland (UNIS), Reykjavik, ICELAND
- Wageningen University (WUR), Wageningen, NETHERLANDS
- Warsaw University (WURSEL), Warsaw, POLAND

The core strategy of HYPER-I-NET was to create a powerful interdisciplinary synergy between different domains of expertise within Europe, and use it to break new grounds in areas related with remotely sensed hyperspectral imaging. A well structured multidisciplinary training programme was developed to cover all the different aspects that comprise the hyperspectral data processing chain, ranging from sensor design and flight operation to data collection, processing, interpretation, and dissemination. As a result, the theme of HYPER-I-NET placed itself at the confluence of heterogeneous disciplines, such as sensor design and calibration, aerospace engineering, remote sensing, high performance computing, image/signal processing and Earth observation related products.

The author of this PhD thesis joined HYPER-I-NET as an early-stage researcher in February 2008, when he started his research activity at Instituto Superior Técnico (IST), Lisbon, Portugal, under the joint supervision of Prof. José M. Bioucas Dias (IST) and Prof. Antonio Plaza from University of Extremadura (UEX), Cáceres, Spain. He was registered as a PhD student at IST in July 2008. According to his appointment path, after 18 months spent at IST, he moved to UEX for a period of the same length. His contract with the HYPER-I-NET project ended in January 2011. Then, he was contracted as a researcher with the Hyperspectral Computing Laboratory

(HyperComp) research group coordinated by Prof. Antonio J. Plaza at the Department of Technology of Computers and Communications, at the same University, funded by the Spanish Ministry of Science and Innovation under the HYPERCOMP/EODIX project, also focused on the development of advanced processing techniques for hyperspectral image analysis.

### 1.1.2 Motivation

The term “remote sensing” was first used in the 1950s by Ms. Evelyn Pruitt of the U.S. Office of Naval Research and its general meaning refers to the science of observing, identifying and measuring an object or a scene without coming into direct contact with it. In other words, the goal is to obtain information about a given scene which is observable, but not available to direct exploration. Later, remotely sensed hyperspectral imaging (also called *imaging spectroscopy*) was defined as the science concerned with the measurement, analysis and interpretation of spectra acquired from a given scene (or specific object) at a short, medium or long distance by an airborne or satellite sensor [73].

Modern hyperspectral sensors are able to sample the electromagnetic spectrum in hundreds of spectral bands [52]. For instance, the Airborne Visible Infra-Red Imaging Spectrometer (AVIRIS)<sup>1</sup> is now able to record the visible and near-infrared spectrum (wavelength region from 400 to 2500 nanometers) of the reflected light of an area 2 to 12 kilometers wide and several kilometers long, using 224 spectral bands. Although AVIRIS is a widely used platform, it constitutes only one source of hyperspectral data. Table 1.1 summarizes other international Earth observation missions with hyperspectral sensors already launched or to be launched in the near future. The data volume resulting from hyperspectral instruments can be seen as a data cube with two spatial dimensions and one spectral dimension. As a result, each pixel is represented by its spectral fingerprint or signature (*observed spectrum*). The observed spectrum is thus a vector comprising the values of reflected radiation at each wavelength.

The number and variety of processing tasks in hyperspectral remote sensing is enormous [24]. However, the majority of algorithms can be organized according to the following specific

---

<sup>1</sup><http://aviris.jpl.nasa.gov>

Table 1.1: Overview of some present and future remote sensing missions including hyperspectral sensors.

	<b>Hyperion<sup>*</sup></b>	<b>Prisma<sup>†</sup></b>	<b>EnMAP<sup>‡</sup></b>	<b>HyspIRI<sup>§</sup></b>
<i>Country of origin</i>	USA	Italy	Germany	USA
<i>Spatial Resolution</i>	30 meters	5-30 meters	30 meters	60 meters
<i>Revisit Time</i>	16 days	3/7 days	4 days	18 days
<i>Spectral Range</i>	400-2500 nanometers	400-2500 nanometers	420-2450 nanometers	380-2500 nanometers
<i>Spectral Resolution</i>	10 nanometers	10 nanometers	6.5-10 nanometers	10 nanometers
<i>Swath width</i>	7.7 kilometers	30 kilometers	30 kilometers	120 kilometers
<i>Earth coverage</i>	Partial	Full	Full	Full
<i>Launch</i>	2000	2010	2012	2018
<i>Lifetime</i>	10 years	$\approx$ 6 years	$\approx$ 6 years	$\approx$ 6 years

<sup>\*</sup><http://eo1.gsfc.nasa.gov> <sup>†</sup>[http://www.asi.it/en/flash\\_en/observing/prisma](http://www.asi.it/en/flash_en/observing/prisma) <sup>‡</sup><http://www.enmap.org>

<sup>§</sup><http://hyspiri.jpl.nasa.gov>

tasks [73]:

- *Dimensionality reduction* consists of reducing the dimensionality of the input hyperspectral scene in order to facilitate subsequent processing tasks.
- *Target and anomaly detection* consist of searching the pixels of a hyperspectral data cube for “rare” (either known or unknown) spectral signatures.
- *Change detection* consists of finding the “significant” (i.e., important to the user) changes between two hyperspectral scenes of the same geographic region.
- *Classification* consists of assigning a label (class) to each pixel of a hyperspectral data cube.
- *Spectral unmixing* consists of estimating the fraction of the pixel area covered by each material present in the scene.

In particular, spectral unmixing has been an alluring exploitation goal since the earliest days of hyperspectral image and signal processing [61]. No matter the spatial resolution, the spectral signatures collected in natural environments are invariably a mixture of the signatures of the various materials found within the spatial extent of the ground instantaneous field view of the imaging instrument. However, the very fine spectral resolution available from hyperspectral instruments allows us to compensate the relatively coarse spatial resolution (which can vary from tens to hundreds of meters) and perform sub-pixel characterization [61] by taking advantage of



the fact that the observed spectrum of a pixel can be interpreted as a combination of the spectra of a set of pure spectral constituents (called *endmembers* in the related literature [77]). Thus, a pixel containing only one constituent material is called *pure pixel*, while a pixel containing more than one material is called *mixed pixel*. In practice, most of the pixels in a scene are mixed.

In this thesis, we specifically focus on the *spectral unmixing* problem, which currently represents a very active area in remote sensing in general and in hyperspectral data analysis in particular. The goal of spectral unmixing is to estimate the materials present in one pixel, their pure signatures and the relative area that they occupy (i.e., their *fractional abundance*) in a given pixel. In the following, we review several relevant topics in state-of-the art spectral unmixing research.

## **Linear versus nonlinear spectral unmixing**

Linear spectral unmixing [85] is the most standard technique for spectral unmixing. It is based on inferring a set of endmembers (generally from the hyperspectral image scene [41]), and their abundance fractions. This model assumes that the spectra collected by the imaging spectrometer can be expressed in the form of a linear combination of endmembers, weighted by their corresponding abundances. Because each observed spectral signal is the result of an actual mixing process, it is expected that the driving abundances satisfy two constraints, i.e., they should be non-negative [26], and the sum of abundances for a given pixel should be unity [24]. Although the linear model has practical advantages, such as ease of implementation and flexibility in different applications, nonlinear unmixing describes mixed spectra (in physical [15, 64], or statistical [78] sense) by assuming that part of the source radiation is multiply scattered before being collected at the sensor. The distinction between linear and nonlinear unmixing has been widely studied in recent years [75]. In this thesis, we focus on linear spectral unmixing due to its generality and ease of implementation (not without acknowledging that nonlinear unmixing may provide better results in terms of spectral characterization in many applications).

## Endmember determination and pure class modelling

Early approaches to endmember determination were principally manual [5, 6]. More recent development of automatic or semi-automatic endmember extraction algorithms has resulted in significant steps forward. While many available approaches associate a single spectral signature to each endmember, multiple endmembers have also been used to account for within (pure) class spectral variation [37, 84, 87, 94]. When multiple spectra are used to represent a pure class, the term endmember refers to all spectra in the modelled pure class.

Notwithstanding the importance of multiple endmember-based approaches, a majority of algorithms have been designed under the pure pixel assumption, i.e., they assume that the remotely sensed data contain one pure observation for each distinct material present in the scene. This allows validation of extracted endmembers with regards to reference signatures using different distance metrics [31]. Perhaps due to their ease of computation and clear conceptual meaning, these are the most widely used class of algorithms for endmember determination, with a plethora of algorithms designed under this assumption (see [7, 14, 16, 27–30, 40, 42, 43, 54, 56, 69, 71, 74, 80, 83, 86, 89, 93, 95, 95, 97–100], among several others). It should be noted, however, that some of the aforementioned algorithms require a dimensionality estimation step [51]. Under the linear mixture assumption, this amounts to estimating the number of endmembers [12, 25].

Although the maximum volume procedure adopted by N-FINDR and related algorithms is successful when pure signatures are present in the data, given the available spatial resolution of state-of-the-art imaging spectrometers and the presence of the mixture phenomenon at different scales (even at microscopic levels), in some cases the pure pixel assumption may not be valid. To address this issue, several endmember determination techniques have been developed without assuming the presence of pure signatures in the input data. These methods aim at generating *virtual* endmembers [33] (not necessarily present in the set comprised by input data samples) by finding the simplex with minimum volume that encompasses all observations [8, 9, 13, 23, 36, 67].

## **Incorporation of spatial information into endmember determination and spectral unmixing**

Most of the techniques discussed so far for endmember determination and spectral unmixing rely on the exploitation of spectral information alone. However, one of the distinguishing properties of remotely sensed data is the multivariate information coupled with a two-dimensional (pictorial) representation amenable to image interpretation. Subsequently, unmixing techniques can benefit from an integrated framework in which both the spectral information and the spatial arrangement of pixel vectors are taken into account. This aspect has been widely studied in the unmixing literature [60, 65, 66, 76, 81, 90, 101].

### **Sparse regression-based unmixing**

In this thesis, we develop a new linear spectral unmixing approach which is intended to tackle the aforementioned problems related to the unavailability of pure spectral signatures in the hyperspectral data, and to include the spatial information in spectral unmixing techniques. Specifically, we propose a new strategy to model mixed pixel observations as linear combinations of spectra from a library collected on the ground by a field spectro-radiometer, thus avoiding the endmember extraction step. As mentioned before, techniques which assume the presence of pure pixels in the data have to deal with the fact that, due to spatial resolution issues and the fact that the mixture problem happens at every scale (even at the intimate mixture level), the most common situation is that the hyperspectral image has no pure pixels at all. While endmember identification techniques that do not assume the presence of pure pixels circumvent this problem, the endmember signatures obtained are *virtual* and often lack physical meaning. In turn, unmixing with spectral libraries allows us to avoid these issues since the library signatures correspond to pure endmember spectra measured on the field, and thus retaining the physical meaning. Further, unmixing with spectral libraries also allows us to avoid the estimation of the number of endmembers in the scene, which is also a very challenging step. As a result, sparse unmixing amounts to finding the optimal subset of signatures in a (potentially very

large) spectral library that can best model each mixed pixel in the scene [58]. In practice, this is a combinatorial problem that calls for efficient sparse regression techniques based on sparsity-inducing regularizers, since the number of endmembers participating in a mixed pixel is usually very small compared with the (ever-growing) dimensionality and availability of spectral libraries. Another advantage of our proposed approach is that it is not necessary to estimate *a priori* the number of endmembers in the scene. The thesis also proposes a new technique to take into account the rich spatial information offered by the hyperspectral images, which is based on the *total variation* (TV) regularizer [59]. Finally, the thesis also proposes a new framework to exploit the group structure of spectral libraries, which are often organized in the form of groups of spectra describing variations of the same material. The techniques developed in this direction are based on the *sparse group Lasso* [57] and on the *collaborative hierarchical lasso* [88], which impose sparsity not only at the endmember level but also at the group level (per pixel and per groups of pixels, respectively).

## 1.2 Thesis organization

The structure of the thesis is summarized in Fig. 1.1. As shown by Fig. 1.1, the thesis comprises three main chapters. In Chapter 2, we describe the core of the sparse unmixing approach. In Chapter 3, we describe how to incorporate spatial information into sparse unmixing. Finally, Chapter 4 describes how to take advantage of the arrangement of spectra in the form of groups in spectral libraries in order to improve sparse unmixing. Finally, Chapter 5 draws the main conclusions and future research lines derived from the present study. In the following we provide a more detailed description of each chapter of the thesis.

### Chapter 2: Sparse Unmixing of Hyperspectral Data

Chapter 2 is the core of this thesis. The chapter first introduces the adopted model for characterizing mixed pixels, which is the linear mixture model. Then, it reviews current approaches

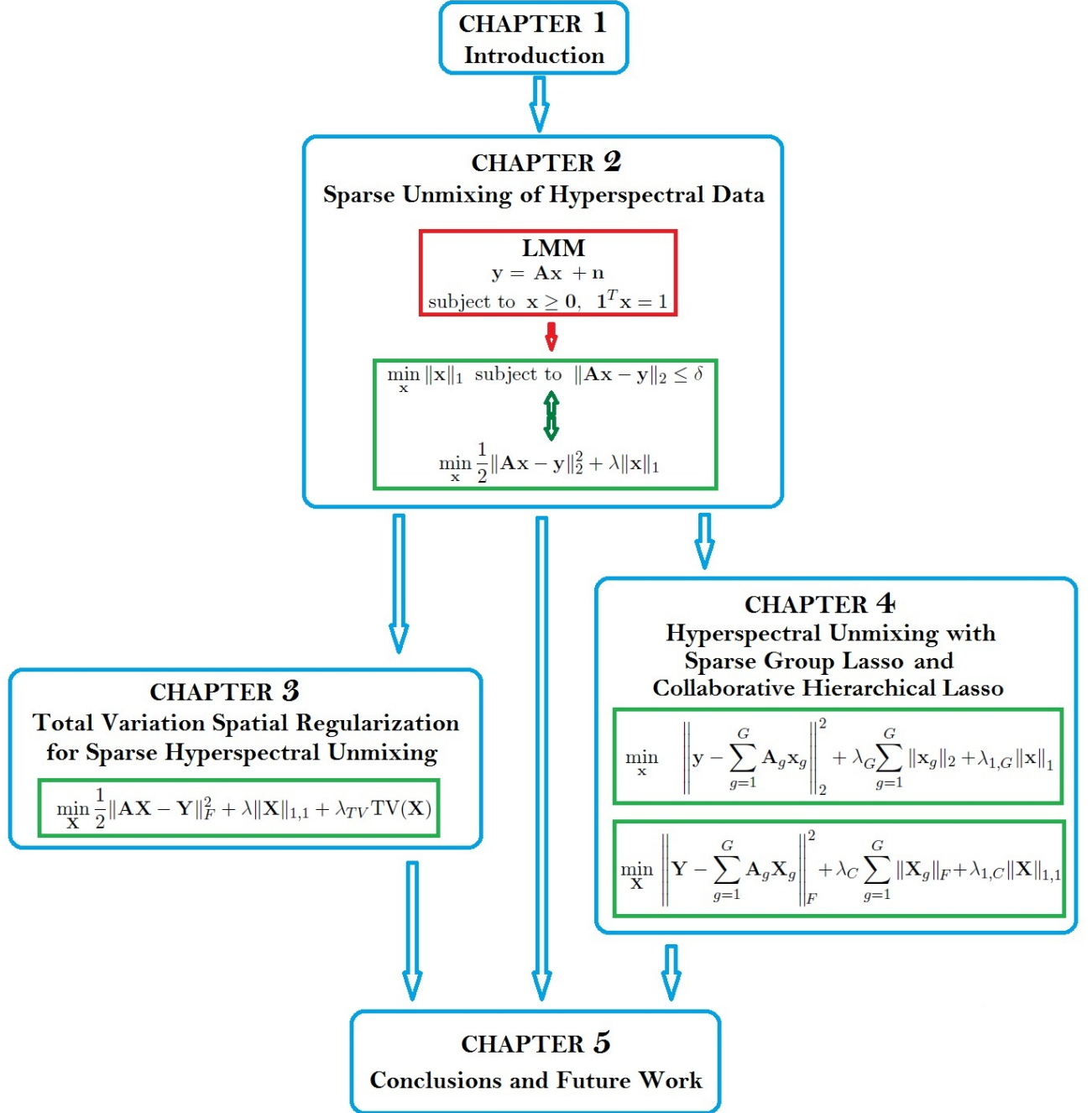


Figure 1.1: Thesis Structure.

for linear spectral unmixing in the literature and presents a completely new framework for this purpose presented in this work, which is based on the use of spectral libraries. Due to the large number of spectra available in such libraries, the spectral unmixing problem needs to be reformulated as a sparse regression problem. A detailed mathematical formulation is provided for this new approach. A section is then explicitly devoted to computational issues and to the presentation of fast algorithms used to solve the sparse unmixing problem. The chapter then presents an extensive experimental validation of sparse regression-based unmixing approaches using both synthetic and real hyperspectral data. Conclusions and future lines of research are presented and discussed at the end of the chapter.

### **Chapter 3: Total Variation Spatial Regularization for Sparse Hyperspectral Unmixing**

While in Chapter 2 we presented the sparse unmixing framework and considered only the spectral information available in the data (i.e., we work with the hyperspectral data on a pixel by pixel basis), in this chapter we include the image representation in the analysis by taking into account the existing spatial correlations between neighboring image pixels. For this purpose, we reformulate sparse regression-based unmixing approaches by including spatial constraints, which are shown to improve the mixed pixel characterization results. This is done by including the TV regularizer [21] [22] in the sparse unmixing formulation. Both isotropic and non-isotropic versions of this regularizer are explored, and detailed experimental comparisons using both synthetic and real hyperspectral data are presented in order to further analyze the advantages of including spatial information in the sparse unmixing formulation. The chapter concludes with a summary of the main achievements and a discussion of the most relevant future directions of research under this topic.

### **Chapter 4: Hyperspectral Unmixing with Sparse Group Lasso and Collaborative Hierarchical Lasso**

As discussed before, spectral libraries are usually large and made up of many spectral signatures which are spectrally similar. This is because available spectral libraries have been constructed in a way that they describe different variations or alterations of the spectral signature of the same material, i.e. the number of distinct materials represented in the library is smaller than the number of spectra, with many spectra associated to the same material with subtle variations. As a result, the spectra in the library can be grouped by materials. Due to the similarity between the spectra contained in one single group, it is likely that the selection of several spectra from the group when conducting the sparse unmixing can improve the mixed pixel characterization results, as the pixel observation is often affected by noise and other interferers that can be usually characterized by using group of spectral materials. In this chapter, we exploit this concept and further explore the advantages that can be gained by including group representations when conducting the sparse unmixing approach. For this purpose, we use the *sparse group Lasso* (SGL) [48] approach in order to impose sparsity both at the individual and group levels. This technique acts individually over each pixel of the image. On the other hand, we also apply a technique which uses the *collaborative hierarchical Lasso* (CHL) to impose sparsity across the pixels in the image, given the specific structure of spectral libraries. The CHL approach is based on the fact that the pixels in the image are generated by the same (small) set of endmembers. Given this, CHL imposes sparsity not only at endmember/group level, but constraints the pixels in the image to share the same set of endmembers. In other words, while SGL acts over individual pixels and imposes sparsity both at member and group level, CHL acts along the pixels, forcing the groups of pixels to share the same endmembers. This chapter also includes experiments with both synthetic and real hyperspectral data sets, followed by a discussion and conclusions. In the final chapter of the thesis, the main contributions of this work and the future lines of research are summarized.

### 1.3 The Main Contributions of the Thesis

To conclude this introductory chapter, we summarize the main contributions of this thesis work.

In the first part of the thesis, we propose a new approach for spectral unmixing of remotely sensed hyperspectral data: the exploitation of the sparse characteristic of the mixtures by formulating the unmixing problem as a sparse regression problem, jointly with the use of (large) *spectral libraries* (which are collections of spectra of pure materials) to avoid some of the difficulties encountered in classical approaches. The proposed methodology uses recently introduced fast algorithms, based on the alternating direction method of multipliers (ADMM) [44] [10].

The next part of the thesis is dedicated to the exploitation of the rich spatial information that the hyperspectral images contain, by enforcing in the sparse regression problem a total variation [21] [22] based term which accounts for spatial regularization.

As the spectral libraries usually contain many similar signatures (variations of the signatures of materials belonging to the same class), their components can be grouped according to some similarity measure. This way, the libraries become structured in groups of materials and the goal of the unmixing process is to find the correct groups present in the mixture, not specifically the exact endmembers. We propose in the last part of thesis a methodology to deal with this type of problem based on a Sparse Group Lasso (SGL) [48] approach. We apply also a new method, based on the Collaborative Hierarchical Lasso [88] and proposed by Bioucas-Dias and Figueiredo in [11], in our unmixing problem. This approach takes advantage of the fact that all the pixels in the hyperspectral image are generated by the same (small) set of endmembers.

Last, but not least, we mention that the optimization problems solved in the thesis imply a huge number of variables, which makes them very difficult to solve. The algorithms that we apply and propose along the thesis were designed to deal with large amounts of data, as it is the case in the hyperspectral applications (in which we work with thousands or hundreds of thousands of spectra when processing an image). These algorithms, dedicated to sparse regression, part of them proposed by Bioucas-Dias and Figueiredo [10] [11], part of them developed in the framework of the thesis, are based on the Alternating Direction Method of Multipliers (ADMM)



[44] framework, which aims at solving iteratively a complex problem after decomposing it in sub-problems easier to solve. The principal goal is to obtain accurate solutions, but we prove, in this thesis, the superiority of these new algorithms over the previous ones, not only in terms of accuracy, but, many times, also in terms of running time. This contribution of the thesis is very important, as it offers the possibility of solving efficiently problems with a huge number of variables.



## Chapter 2

# Sparse Unmixing of Hyperspectral Data

**Abstract** – Linear spectral unmixing is a popular tool in remotely sensed hyperspectral data interpretation. It aims at estimating the fractional abundances of pure spectral signatures (also called *endmembers*) in each mixed pixel collected by an imaging spectrometer. In many situations, the identification of endmember signatures in the original data set may be challenging due to insufficient spatial resolution, mixtures happening at different scales, and unavailability of completely pure spectral signatures in the scene. However, the unmixing problem can also be approached in semi-supervised fashion, i.e. by assuming that the observed image signatures can be expressed in the form of linear combinations of a number of pure spectral signatures known in advance (e.g. spectra collected on the ground by a field spectro-radiometer). Unmixing then amounts to finding the optimal subset of signatures in a (potentially very large) spectral library that can best model each mixed pixel in the scene. In practice, this is a combinatorial problem which calls for efficient linear sparse regression techniques based on sparsity-inducing regularizers, since the number of endmembers participating in a mixed pixel is usually very small compared with the (ever-growing) dimensionality – and availability – of spectral libraries.

Linear sparse regression is an area of very active research with strong links to compressed sensing, basis pursuit, basis pursuit denoising, and matching pursuit. In this work, we study the linear spectral unmixing problem under the light of recent theoretical results published in those referred to areas. Furthermore, we provide a comparison of several available and new linear sparse regression algorithms with the ultimate goal of analyzing their potential in solving the

spectral unmixing problem by resorting to available spectral libraries.

Our experimental results, conducted using both simulated and real hyperspectral data sets collected by the NASA Jet Propulsion Laboratory’s Airborne Visible Infra-Red Imaging Spectrometer (AVIRIS) and spectral libraries publicly available from U.S. Geological Survey (USGS), indicate the potential of sparse regression techniques in the task of accurately characterizing mixed pixels using library spectra. This opens new perspectives for spectral unmixing, since the abundance estimation process no longer depends on the availability of pure spectral signatures in the input data nor on the capacity of a certain endmember extraction algorithm to identify such pure signatures.

**Index Terms** – Hyperspectral imaging, spectral unmixing, abundance estimation, sparse regression, convex optimization.

## 2.1 Introduction

Hyperspectral imaging has been transformed from being a sparse research tool into a commodity product available to a broad user community [49]. The wealth of spectral information available from advanced hyperspectral imaging instruments currently in operation has opened new perspectives in many application domains, such as monitoring of environmental and urban processes or risk prevention and response, including – among others – tracking wildfires, detecting biological threats, and monitoring oil spills and other types of chemical contamination. Advanced hyperspectral instruments such as NASA’s Airborne Visible Infra-Red Imaging Spectrometer (AVIRIS) [52] are now able to cover the wavelength region from 0.4 to 2.5  $\mu\text{m}$  using more than 200 spectral channels, at nominal spectral resolution of 10 nm. The resulting hyperspectral data cube is a stack of images (see Fig. 2.1) in which each pixel (vector) is represented by a spectral signature or *fingerprint* that characterizes the underlying objects.

Several analytical tools have been developed for remotely sensed hyperspectral data processing in recent years, covering topics like dimensionality reduction, classification, data compression, or spectral unmixing [24, 62]. The underlying assumption governing clustering and classifica-

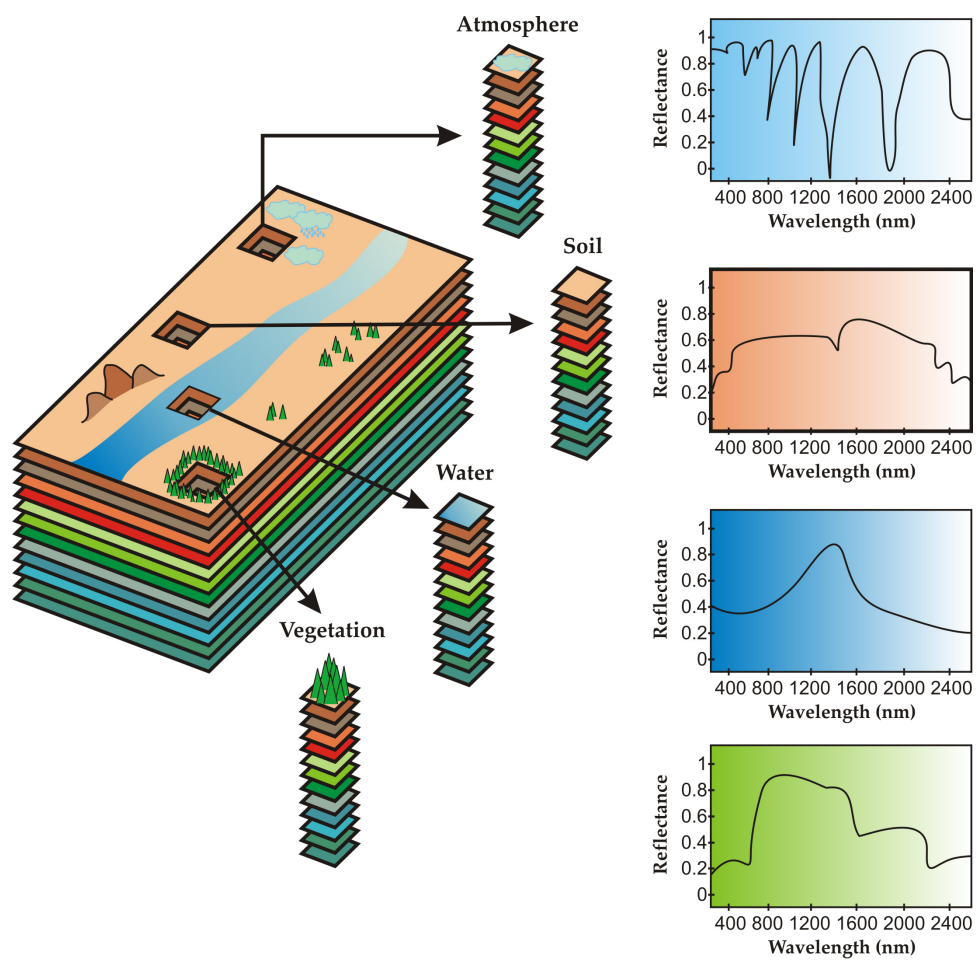


Figure 2.1: Concept of hyperspectral imaging and presence of mixed pixels.

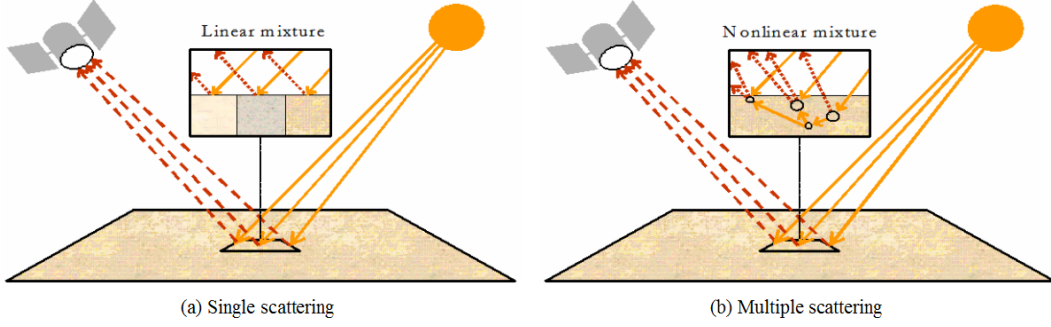


Figure 2.2: Linear (a) versus nonlinear (b) mixture models.

tion techniques is that each pixel vector comprises the response of a single underlying material. However, if the spatial resolution of the sensor is not high enough to separate different materials, these can jointly occupy a single pixel. For instance, it is likely that the pixel collected over a vegetation area in Fig. 2.1 actually comprises a mixture of vegetation and soil. In this case, the measured spectrum may be decomposed into a linear combination of pure spectral signatures of soil and vegetation, weighted by abundance fractions that indicate the proportion of each *macroscopically* pure signature in the mixed pixel [61].

To deal with this problem, linear spectral mixture analysis techniques first identify a collection of spectrally pure constituent spectra, called *endmembers* in the literature, and then express the measured spectrum of each mixed pixel as a linear combination of endmembers weighted by fractions or abundances that indicate the proportion of each endmember present in the pixel [1]. It should be noted that the linear mixture model assumes minimal secondary reflections and/or multiple scattering effects in the data collection procedure, and hence the measured spectra can be expressed as a linear combination of the spectral signatures of materials present in the mixed pixel [see Fig. 2.2(a)]. Quite opposite, the nonlinear mixture model assumes that the endmembers form an intimate mixture inside the respective pixel, so that incident radiation interacts with more than one component and is affected by multiple scattering effects [see Fig. 2.2(b)]. Nonlinear unmixing generally requires prior knowledge about object geometry and physical properties of the observed objects. In this work we will focus exclusively on the linear mixture model due to its computational tractability and flexibility in different applications.

The linear mixture model assumes that the spectral response of a pixel in any given spectral

band is a linear combination of all the endmembers present in the pixel, at the respective spectral band. For each pixel, the linear model can be written as follows:

$$y_i = \sum_{j=1}^q m_{ij} \alpha_j + n_i, \quad (2.1)$$

where  $y_i$  is the measured value of the reflectance at spectral band  $i$ ,  $m_{ij}$  is the reflectance of the  $j$ -th endmember at spectral band  $i$ ,  $\alpha_j$  is the fractional abundance of the  $j$ -th endmember, and  $n_i$  represents the error term for the spectral band  $i$  (i.e. the noise affecting the measurement process). If we assume that the hyperspectral sensor used in data acquisition has  $L$  spectral bands, Eq. (2.1) can be rewritten in compact matrix form as:

$$\mathbf{y} = \mathbf{M}\boldsymbol{\alpha} + \mathbf{n}, \quad (2.2)$$

where  $\mathbf{y}$  is an  $L \times 1$  column vector (the measured spectrum of the pixel),  $\mathbf{M}$  is an  $L \times q$  matrix containing  $q$  pure spectral signatures (endmembers),  $\boldsymbol{\alpha}$  is a  $q \times 1$  vector containing the fractional abundances of the endmembers, and  $\mathbf{n}$  is an  $L \times 1$  vector collecting the errors affecting the measurements at each spectral band. The so-called abundance non-negativity constraint (ANC):  $\alpha_i \geq 0$  for  $i = 1, \dots, q$ , and the abundance sum-to-one constraint (ASC):  $\sum_{i=1}^q \alpha_i = 1$ , which we respectively represent in compact form by:

$$\boldsymbol{\alpha} \geq \mathbf{0}, \quad (2.3)$$

$$\mathbf{1}^T \boldsymbol{\alpha} = 1, \quad (2.4)$$

where  $\mathbf{1}^T$  is a line vector of 1's compatible with  $\boldsymbol{\alpha}$ , are often imposed into the model described in Eq. (2.1) [55], owing to the fact that  $\alpha_i$ , for  $i = 1, \dots, q$ , represent the fractions of the endmembers present in the considered pixel.

In a typical hyperspectral unmixing scenario, we are given a set  $\mathbf{Y} \equiv \{\mathbf{y}_i \in \mathbb{R}^L, i = 1, \dots, n\}$  of  $n$  observed  $L$ -dimensional spectral vectors, and the objective is to estimate the mixing ma-

trix  $\mathbf{M}$  and the fractional abundances  $\boldsymbol{\alpha}$  for every pixel in the scene. This is a blind source separation problem and, naturally, independent component analysis methods come to mind to solve it. However, the assumption of statistical independence among the sources (the fractional abundances in our application), central to independent component analysis methods, does not hold in hyperspectral applications, since the sum of fractional abundances associated to each pixel is constant. Thus, sources are statistically dependent, which compromises the performance of independent component analysis algorithms in hyperspectral unmixing [68].

We note the constraints (2.3) and (2.4) define the set  $\mathcal{S}_{q-1} \equiv \{\boldsymbol{\alpha} \in \mathbb{R}^q \mid \boldsymbol{\alpha} \geq \mathbf{0}, \mathbf{1}^T \boldsymbol{\alpha} = 1\}$ , which is the probability simplex in  $\mathbb{R}^q$ . Furthermore, the set  $\mathcal{S}_M \equiv \{\mathbf{M}\boldsymbol{\alpha} \in \mathbb{R}^L \mid \boldsymbol{\alpha} \in \mathcal{S}_{q-1}\}$  is also a simplex whose vertices are the columns of  $\mathbf{M}$ . Over the last decade, several algorithms have exploited this geometrical property by estimating the “smallest” simplex set containing the observed spectral vectors [74, 77]. Some classic techniques for this purpose assume input data set contains at least one pure pixel for each distinct material present in the scene, and therefore a search procedure aimed at finding the most spectrally pure signatures in the input scene is feasible. Among the *endmember extraction* algorithms working under this regime we can list some popular approaches such as the pixel purity index (PPI) [14], N-FINDR [95], orthogonal subspace projection (OSP) technique in [79], and vertex component analysis (VCA) [69]. However, the assumption under which these algorithms perform may be difficult to guarantee in practical applications due to several reasons:

1. First, if the spatial resolution of the sensor is not high enough to separate different pure signature classes at a macroscopic level, the resulting spectral measurement can be a composite of individual pure spectra which correspond to materials that jointly occupy a single pixel. In this case, the use of image-derived endmembers may not result in accurate fractional abundance estimations since it is likely that such endmembers may not be completely pure in nature.
2. Second, mixed pixels can also result when distinct materials are combined into a microscopic (intimate) mixture, independently of the spatial resolution of the sensor. Since the



mixtures in this situation happen at the particle level, the use of image-derived spectral endmembers cannot accurately characterize intimate spectral mixtures.

In order to overcome the two aforementioned issues, other advanced *endmember generation* algorithms have also been proposed under the assumption that pure signatures are not present in the input data. Such techniques include optical real-time adaptive spectral identification system (ORASIS) [16], convex cone analysis (CCA) [56], iterative error analysis (IEA) [71], automatic morphological endmember extraction (AMEE) [76], iterated constrained endmembers (ICE) [7], minimum volume constrained non-negative matrix factorization (MVC-NMF) [67], spatial-spectral endmember extraction (SSEE) [81], sparsity-promoting ICE (SPICE) [97], minimum volume simplex analysis (MVSA) [63], and simplex identification *via* split augmented Lagrangian (SISAL) [8]. A necessary condition for these endmember generation techniques to yield good estimates is the presence in the data set of at least  $q - 1$  spectral vectors on each facet of the simplex set  $\mathcal{S}_M$  [8]. This condition is very likely to fail in highly mixed scenarios, in which the above techniques generate *artificial* endmembers, i.e. not necessarily associated to physically meaningful spectral signatures of true materials.

In this work, we adopt a novel semi-supervised approach to linear spectral unmixing which relies on the increasing availability of spectral libraries of materials measured on the ground, for instance, using advanced field spectro-radiometers. Our main assumption is that mixed pixels can be expressed in the form of linear combinations of a number of pure spectral signatures known in advance and available in a library, such as the well-known one publicly available from U.S. Geological Survey (USGS)<sup>1</sup>, which contains over 1300 mineral signatures, or the NASA Jet Propulsion Laboratory’s Advanced Spaceborne Thermal Emission and Reflection Radiometer (ASTER) spectral library<sup>2</sup>, a compilation of over 2400 spectra of natural and man-made materials. When the unmixing problem is approached using spectral libraries, the abundance estimation process no longer depends on the availability of pure spectral signatures in the input data nor on the capacity of a certain endmember extraction algorithm to identify

---

<sup>1</sup>Available online: <http://speclab.cr.usgs.gov/spectral-lib.html>

<sup>2</sup>Available online: <http://speclib.jpl.nasa.gov>

such pure signatures. Quite opposite, the procedure is reduced to finding the optimal subset of signatures in the library that can best model each mixed pixel in the scene. Despite the appeal of this semi-supervised approach to spectral unmixing, this approach is also subject to a few potential drawbacks:

1. One risk in using library endmembers is that these spectra are rarely acquired under the same conditions as the airborne data. Image endmembers have the advantage of being collected at the same scale as the data and can, thus, be more easily associated with features on the scene. However, such image endmembers may not always be present in the input data. In this work, we rely on the use of advanced atmospheric correction algorithms which convert the input hyperspectral data from at-sensor radiance to reflectance units.
2. The ability to obtain useful sparse solutions for an under-determined system of equations depends, mostly, on the degree of coherence between the columns of the system matrix and the degree of sparseness of original signals (i.e., the abundance fractions) [18], [17], [20], [19]. The most favorable scenarios correspond to highly sparse signals and system matrices with low coherence. Unfortunately, in hyperspectral applications the spectral signatures of the materials tend to be highly correlated. On the other hand, the number of materials present in a given scene is often small, say, less than 20 and, most importantly, the number of materials participating in a mixed pixel is usually on the order of 4–5 [61]. Therefore, the undesirable high coherence of hyperspectral libraries can be mitigated, to some extent, by the highly sparse nature of the original signals.
3. The sparse solutions of under-determined systems are computed by solving optimization problems containing non-smooth terms [17]. The presence of these terms introduces complexity because the standard optimization tools of the gradient and Newton family cannot be directly used. To make the scenario even more complex, a typical hyperspectral image has hundreds or thousands of spectral vectors, implying an equal number of independent optimizations to unmix the complete scene. To cope with this computational complexity,

we resort to recently introduced (fast) algorithms based on the augmented Lagrangian method of multipliers [10].

In this work, we specifically address the problem of sparsity when unmixing hyperspectral data sets using spectral libraries, and further provide a quantitative and comparative assessment of several available and new optimization algorithms in the context of linear sparse problems. The remainder of the chapter is organized as follows. Section 2.2 formulates the sparse regression problem in the context of hyperspectral unmixing. Section 2.3 describes several available and new unmixing algorithms with the ultimate goal of analyzing their potential in solving sparse hyperspectral unmixing problems. Section 2.4 provides an experimental validation of the considered algorithms using simulated hyperspectral mixtures from real and synthetic spectral libraries. The primary reason for the use of simulated data is that all details of the simulated mixtures are known and can be efficiently investigated because they can be manipulated individually and precisely. As a complement to simulated data experiments, Section 2.5 presents an experimental validation of the considered sparse regression and convex optimization algorithms using a well-known hyperspectral scene collected by the AVIRIS instrument over the Cuprite mining district in Nevada. The USGS spectral library is used for conducting extensive semi-supervised unmixing experiments on this scene. Finally, Section 2.6 concludes with some remarks and hints at plausible future research. An Appendix is devoted to the description of the parameter settings used in our experiments and to the strategies followed to infer these parameters.

## **2.2 Spectral Unmixing Reformulated as a sparse Regression Problem**

In this section, we revisit the classic linear spectral unmixing problem and reformulate it as a semi-supervised approach using sparse regression (SR) terminology. Furthermore, we review the SR optimization problems relevant to our unmixing problem, their theoretical characterization,

their computational complexity, and the algorithms to solve them exactly or approximately.

Let us assume that the spectral endmembers used to solve the mixture problem are no longer extracted nor generated using the original hyperspectral data as input, but instead selected from a library containing a large number of spectral samples available *a priori*. In this case, unmixing amounts to finding the optimal subset of samples in the library that can best model each mixed pixel in the scene. This means that a searching operation must be conducted in a (potentially very large) library, which we denote by  $\mathbf{A} \in \mathbb{R}^{L \times m}$ , where  $L$  and  $m$  are the number of spectral bands and the number of materials in the library, respectively. All libraries herein considered correspond to under-determined systems, i.e.,  $L < m$ . With the aforementioned assumptions in mind, let  $\mathbf{x} \in \mathbb{R}^m$  denote the fractional abundance vector with regards to the library  $\mathbf{A}$ . As usual, we say that  $\mathbf{x}$  is a  $k$ -sparse vector if it has at most  $k$  components different from zero. With these definitions in place, we can now write our SR problem as:

$$\min_{\mathbf{x}} \|\mathbf{x}\|_0 \text{ subject to } \|\mathbf{y} - \mathbf{Ax}\|_2 \leq \delta, \mathbf{x} \geq \mathbf{0}, \mathbf{1}^T \mathbf{x} = 1, \quad (2.5)$$

where  $\|\mathbf{x}\|_0$  denotes the number of non-zero components of  $\mathbf{x}$  and  $\delta \geq 0$  is the error tolerance due to noise and modeling errors. A solution of problem (2.5), if any, belongs to the set of sparsest signals belonging to the  $(m-1)$ -probability simplex satisfying error tolerance inequality  $\|\mathbf{y} - \mathbf{Ax}\|_2 \leq \delta$ . Prior to addressing problem (2.5), we consider a series of simpler related problems.

### 2.2.1 Exact solutions

Let us first start by assuming that noise is zero and ANC and ASC constraints are not enforced.

Our SR optimization problem is then:

$$(P_0): \min_{\mathbf{x}} \|\mathbf{x}\|_0 \text{ subject to } \mathbf{Ax} = \mathbf{y}. \quad (2.6)$$

If the system of linear equations  $\mathbf{Ax} = \mathbf{y}$  has a solution satisfying  $2\|\mathbf{x}\|_0 < \text{spark}(\mathbf{A})$ ,

where  $\text{spark}(\mathbf{A}) \leq \text{rank}(\mathbf{A}) + 1$  is the smallest number of linearly dependent columns of  $\mathbf{A}$ , it is necessarily the unique solution of  $(P_0)$  [38], [50]. The spark of a matrix gives us a very simple way to check the uniqueness of a solution of the system  $\mathbf{Ax} = \mathbf{y}$ . For example, if the elements of  $\mathbf{A}$  are independent and identically distributed (i.i.d.), then with probability 1 we have  $\text{spark}(\mathbf{A}) = m + 1$ , implying that every solution with no more than  $L/2$  entries is unique.

In our SR problem, we would like then to compute the spark of the hyperspectral library being used, to have an idea of what is the minimum level of sparsity of the fractional abundance vectors that can be uniquely determined by solving  $(P_0)$ . Computing the spark of a general matrix is, however, a hard problem, at least as difficult as solving  $(P_0)$ . This complexity has fostered the introduction of entities simpler to compute, although providing less tight bounds. The *mutual coherence* is such an example; denoting the  $k^{\text{th}}$  column in  $\mathbf{A}$  by  $\mathbf{a}_k$  and the  $\ell_2$  norm by  $\|\cdot\|_2$ , the mutual coherence of  $\mathbf{A}$  is given by:

$$\mu(\mathbf{A}) \equiv \max_{1 \leq k, j \leq m, k \neq j} \frac{|\mathbf{a}_k^T \mathbf{a}_j|}{\|\mathbf{a}_k\|_2 \|\mathbf{a}_j\|_2}, \quad (2.7)$$

i.e., by the maximum absolute value of the cosine of the angle between any two columns of  $\mathbf{A}$ .

The mutual coherence supplies us with a lower bound for the spark given by [38]:

$$\text{spark}(\mathbf{A}) \geq 1 + \frac{1}{\mu(\mathbf{A})}.$$

Unfortunately, as it will be shown further, the mutual coherence of hyperspectral libraries is very close to 1 leading to useless bounds for the spark. In the following, we illustrate two relaxed strategies for computing  $(P_0)$ : *pursuit algorithms* and *nonnegative signals*.

## Pursuit algorithms

The problem  $(P_0)$  is NP-hard (meaning that the problem is combinatorial and very complex to solve) [70] and therefore there is little hope in solving it in a straightforward way. Greedy algorithms, such as the orthogonal basis pursuit (OMP) [72], and basis pursuit (BP) [32] are

two alternative approaches to compute the sparsest solution. The basis pursuit replaces the  $\ell_0$  norm in  $(P_0)$  with the  $\ell_1$  norm:

$$(P_1): \min_{\mathbf{x}} \|\mathbf{x}\|_1 \text{ subject to } \mathbf{A}\mathbf{x} = \mathbf{y}. \quad (2.8)$$

Contrary to problem  $(P_0)$ , problem  $(P_1)$  is convex and can be written as a linear programming (LP) problem and solved using LP solvers. What is, perhaps, totally unexpected is that, in given circumstances related with matrix  $\mathbf{A}$ , problem  $(P_1)$  has the same solution as problem  $(P_0)$ . This result is stated in terms of the restricted isometric constants introduced in [20]. Herein, we use the variant proposed in [47]. Let  $\alpha_k, \beta_k \geq 0$  to be the tightest constants in the inequalities:

$$\alpha_k \|\mathbf{x}\|_2 \leq \|\mathbf{A}\mathbf{x}\|_2 \leq \beta_k \|\mathbf{x}\|_2, \quad \|\mathbf{x}\|_0 \leq k, \quad (2.9)$$

and further define:

$$\gamma_{2s} \equiv \frac{\beta_{2s}^2}{\alpha_{2s}^2} \geq 1. \quad (2.10)$$

Then, under the assumption that  $\gamma_{2s} < 4\sqrt{2} - 3 \simeq 2.6569$ , every  $s$ -sparse vector is recovered by solving problem  $(P_1)$  (see Theorem 2.1 and Corollary 2.1 of [47]). Meanwhile, it has been shown that, in some cases, the OMP algorithm also provides the  $(P_0)$  solution in a fashion comparable with the BP alternative, with the advantage of being faster and easier to implement [92], [17].

### Nonnegative signals

We now consider the problem:

$$(P_0^+): \min_{\mathbf{x}} \|\mathbf{x}\|_0 \text{ subject to } \mathbf{A}\mathbf{x} = \mathbf{y} \quad \mathbf{x} \geq \mathbf{0}. \quad (2.11)$$

and follow a line of reasoning close to that of [18]. Hyperspectral libraries generally contain only nonnegative components (i.e. reflectances). Thus, by assuming that the zero vector is not in

the columns of  $\mathbf{A}$ , it is always possible to find a vector  $\mathbf{h}$  such that:

$$\mathbf{h}^T \mathbf{A} = \mathbf{w}^T > 0. \quad (2.12)$$

Since all components of  $\mathbf{w}$  are nonnegative, the matrix  $\mathbf{W}^{-1}$ , where  $\mathbf{W} \equiv \text{diag}(\mathbf{w})$ , is well-defined and has positive diagonal entries. Defining  $\mathbf{z} \equiv \mathbf{W}\mathbf{x}$ ,  $c \equiv \mathbf{h}^T \mathbf{y}$ ,  $\mathbf{D} \equiv \mathbf{A}\mathbf{W}^{-1}$ , and noting that:

$$\mathbf{h}^T \mathbf{A}\mathbf{W}^{-1} \mathbf{z} = \mathbf{1}^T \mathbf{z}, \quad (2.13)$$

the problem  $(P_0^+)$  is equivalent to:

$$(P_0^+): \min_{\mathbf{x}} \|\mathbf{z}\|_0 \quad \text{subject to} \quad \mathbf{D}\mathbf{z} = \mathbf{y} \quad \mathbf{z} \geq \mathbf{0}, \quad \mathbf{1}^T \mathbf{z} = c. \quad (2.14)$$

We conclude that, when the original signals are nonnegative and the system matrices comply with property (2.12), then problem (2.11) enforces the equality constraint  $\mathbf{1}^T \mathbf{z} = c$ . This constraint has very strong connections with the ASC constraint which is so popular in hyperspectral applications. ASC is, however, prone to strong criticisms because, in a real image, there is strong signature variability [4] that, at the very least, introduces positive scaling factors varying from pixel to pixel in the signatures present in the mixtures. As a result, the signatures are defined up to a scale factor and, thus, ASC should be replaced with a generalized ASC of the form  $\sum_i \xi_i x_i = 1$ , in which the weights  $\xi_i$  denote the pixel-dependent scale factors. What we conclude from the equivalence between problems (2.11) and (2.14) is that the nonnegativity of the sources imposes automatically a generalized ASC. For this reason we do not impose explicitly the ASC constraint.

Similarly to problem  $(P_0)$ , problem  $(P_0^+)$  is NP-hard and impossible to solve exactly for a

general matrix  $\mathbf{A}$ . As shown previously, we can consider instead the  $\ell_1$  relaxation:

$$(P_1^+): \min_{\mathbf{z}} \|\mathbf{z}\|_1 \quad \text{subject to} \quad \mathbf{D}\mathbf{z} = \mathbf{y} \quad \mathbf{z} \geq \mathbf{0}. \quad (2.15)$$

Here, we have dropped the equality constraint  $\mathbf{1}^T \mathbf{z} = c$  because it is satisfied by any solution of  $\mathbf{D}\mathbf{z} = \mathbf{y}$ . As with problem  $(P_0)$ , the condition  $\gamma_{2s} < 4\sqrt{2} - 3 \simeq 2.6569$  referred to in this subsection is now applied to the restricted isometric constants of matrix  $\mathbf{D}$  to ensure that any  $s$ -sparse vector solution of  $(P_0^+)$  is recovered by solving the problem  $(P_1^+)$ .

Another way of characterizing the uniqueness of the solution of problem  $(P_0^+)$  is *via* the *one-sided coherence* introduced in [18]. However, similarly to the mutual coherence, the one-sided coherence of hyperspectral libraries is very close to one leading to useless bounds. The coherence may be increased by left multiplying the system  $\mathbf{D}\mathbf{z} = \mathbf{y}$  with a suitable invertible matrix  $\mathbf{P}$  [18]. This preconditioning tends to improve the performance of greedy algorithms such as OMP. It leads, however, to an optimization problem equivalent to  $(P_1^+)$ . Thus, a BP solver yields the same solution.

### 2.2.2 Approximate solutions

We now assume now that the perturbation  $\mathbf{n}$  in the observation model is not zero, and still we want to find an approximate solution for our SR problem. The computation of approximate solutions raises issues parallel to those found for exact solutions as addressed above. Therefore, we go very briefly through the same topics. Again, we start by assuming that the noise is zero and ANC and ASC constraints are not enforced. Our noise-tolerant SR optimization problem is then:

$$(P_0^\delta): \min_{\mathbf{x}} \|\mathbf{x}\|_0 \quad \text{subject to} \quad \|\mathbf{A}\mathbf{x} - \mathbf{y}\|_2 \leq \delta. \quad (2.16)$$

The concept of uniqueness of the sparsest solution is now replaced with the concept of stability [39], [91], [47]. For example, in [39] it is shown that, given a sparse vector  $\mathbf{x}_0$  satisfying the



sparsity constraint  $\mathbf{x}_0 < (1 + 1/\mu(\mathbf{A}))/2$  such that  $\|\mathbf{A}\mathbf{x}_0 - \mathbf{y}\| \leq \delta$ , then every solution  $\mathbf{x}_0^\delta$  of problem  $(P_0^\delta)$  satisfies:

$$\|\mathbf{x}_0^\delta - \mathbf{x}_0\|^2 \leq \frac{4\delta^2}{1 - \mu(\mathbf{A})(2\mathbf{x}_0 - 1)}. \quad (2.17)$$

Notice that, when  $\delta = 0$ , i.e., when the solutions are exact, this result parallels those ensuring the uniqueness of the sparsest solution. Again, we illustrate two relaxed strategies for computing  $(P_0)$ :

### Pursuit algorithms

Problem  $(P_0^\delta)$ , as  $(P_0)$ , is NP-hard. We consider here two approaches to tackle this problem. The first is the greedy OMP algorithm with stopping rule  $\|\mathbf{A}\mathbf{x} - \mathbf{y}\|_2 \leq \delta$ . The second consists of relaxing the  $\ell_0$  norm to the  $\ell_1$  norm, thus obtaining a so-called *basis pursuit denoising* (BPDN) optimization problem [32]:

$$(P_1^\delta) : \min_{\mathbf{x}} \|\mathbf{x}\|_1 \text{ subject to } \|\mathbf{A}\mathbf{x} - \mathbf{y}\|_2 \leq \delta. \quad (2.18)$$

Contrarily to problem  $(P_0^\delta)$ , problem  $(P_1^\delta)$  is convex and, thus, it is very likely to be solved efficiently with convex optimization methods. As in  $(P_0^\delta)$ , the stability of the solution of problem  $(P_1^\delta)$  has also been provided [19], [47]. For example, from Theorem 3.1 of [47], we have that, if  $\gamma_{2s} < 4\sqrt{2} - 3 \simeq 2.6569$ , the  $\ell_2$  error between any  $s$ -sparse solution  $\mathbf{x}$  of  $\mathbf{A}\mathbf{x} = \mathbf{y}$  and any solution  $\mathbf{x}_1^\delta$  of  $(P_1^\delta)$  satisfies:

$$\|\mathbf{x}_1^\delta - \mathbf{x}\|_2 \leq C\delta, \quad (2.19)$$

where  $\delta$  is a constant depending on the restricted isometric constants  $\alpha_{2s}$  and  $\beta_{2s}$  defined in (2.9).

## Nonnegative signals

We now consider the problem:

$$(P_0^{\delta+}) : \min_{\mathbf{x}} \|\mathbf{x}\|_0 \quad \text{subject to} \quad \|\mathbf{Ax} - \mathbf{y}\|_2 \leq \delta, \quad \mathbf{x} \geq 0. \quad (2.20)$$

Following the reasoning already put forward in subsection 2.2.1, we have that problem  $(P_0^{\delta+})$  is equivalent to:

$$\min_{\mathbf{z}} \|\mathbf{z}\|_0 \quad \text{subject to} \quad \|\mathbf{Dz} - \mathbf{y}\|_2 \leq \delta, \quad \mathbf{z} \geq 0, \quad (2.21)$$

where, as shown previously in this subsection for nonnegative signals,  $\mathbf{D} \equiv \mathbf{AW}^{-1}$ ,  $\mathbf{W} \equiv \text{diag}(\mathbf{h}^T \mathbf{A})$  and  $\mathbf{h}$  is chosen such that  $\mathbf{h}^T \mathbf{A} > 0$ . From the observation equation  $\mathbf{y} = \mathbf{Dz} + \mathbf{n}$  and from  $\|\mathbf{n}\| \leq \delta$ , we may now write  $\mathbf{1}^T \mathbf{z} = c + \mathbf{h}^T \mathbf{n}$ , where  $c \equiv \mathbf{h}^T \mathbf{y}$ . Therefore, the positivity constraint in problem  $(P_0^{\delta+})$  jointly with the property  $\mathbf{h}^T \mathbf{A} > 0$  impose implicitly a soft constraint  $\|\mathbf{1}^T \mathbf{z} - c\|_2 \leq \delta_h$ , where  $\delta_h$  is such that  $\|\mathbf{h}^T \mathbf{n}\|_2 \leq \delta_h$ .

Similarly to  $(P_0^\delta)$ , problem  $(P_0^{\delta+})$  is NP-hard and impossible to solve exactly for a general matrix  $\mathbf{A}$  or  $\mathbf{D}$ . We can consider instead the  $\ell_1$  relaxation:

$$(P_1^{\delta+}) : \min_{\mathbf{z}} \|\mathbf{z}\|_1 \quad \text{subject to} \quad \|\mathbf{Dz} - \mathbf{y}\|_2 \leq \delta, \quad \mathbf{z} \geq 0. \quad (2.22)$$

As with problem  $(P_1^\delta)$ , the condition  $\gamma_{2s} < 4\sqrt{2} - 3 \simeq 2.6569$  is now applied to the restricted isometric constants of matrix  $\mathbf{D}$ , thus ensuring the stability of the solutions of  $(P_1^{\delta+})$ .

## 2.3 Algorithms

In the previous section we have listed a series of optimization problems aimed at computing sparse exact and approximate solutions for our hyperspectral SR problem. In this section, we explain in detail the algorithms we are going to use for experimental validation in the next two sections. Specifically, we considered five unmixing algorithms, of which three do not enforce

---

**Algorithm 2.1** Pseudocode of the Classic Orthogonal Matching Pursuit (OMP) Algorithm.

---

**Initialization:**

Iteration:  $i = 0$

Initial solution:  $\mathbf{x}^0 = \mathbf{0}$

Initial residual:  $\mathbf{r}^0 = \mathbf{y}$

Initial matrix of selected indices:  $\Lambda^0 = \Phi$  (*empty*)

**Main iteration:**

Update iteration:  $i \leftarrow i + 1$

Compute the index of the best correlated member of  $\mathbf{A}$  to the actual residual:

$index \leftarrow \arg \min_{1 \leq k \leq m} \|\mathbf{A}_k \mathbf{x}^{i-1} - \mathbf{r}^{i-1}\|_2^2$  where  $\mathbf{A}_k$  represents the  $k^{th}$  column of

$\mathbf{A}$

Update support:  $\Lambda^i \leftarrow \Lambda^{i-1} \cup \{index\}$

Update solution:  $\mathbf{x}^i \leftarrow \arg \min_{\mathbf{x}} \|\mathbf{A}_{\Lambda^i} \mathbf{x} - \mathbf{y}\|_2^2$  subject to: Support  $\{\mathbf{x}^i\} = \Lambda^i$

(where  $\mathbf{A}_{\Lambda^i}$  is the matrix containing the columns of  $\mathbf{A}$  having the indexes from

$\Lambda^i$ )

Update residual:  $\mathbf{r}^i \leftarrow \mathbf{y} - \mathbf{A} \mathbf{x}^i$

Stop if termination rule:  $\|\mathbf{r}^i\|_2^2 \leq T$  is satisfied (the norm of the residual is below a preset threshold  $T$ )

Otherwise, repeat from **Main iteration**.

---

explicitly the sparseness of the solution, while the other two belong to the sparse unmixing class of algorithms.

### 2.3.1 Orthogonal Matching Pursuit Algorithms

Many variants of the OMP have been published (see [18] and the references therein). Herein, we use the standard implementation shown, for one pixel, in Algorithm 2.1. The algorithm keeps track of the residual  $\mathbf{y} - \mathbf{A} \mathbf{x}^i$ , where  $\mathbf{x}^i$  is the estimate of  $\mathbf{x}$  at the  $i$ -th algorithm iteration. At the first iteration, the initial residual is equal to the observed spectrum of the pixel, the vector of fractional abundances is null and the matrix of the indices of selected endmembers is empty. Then, at each iteration, the algorithm finds the member of  $\mathbf{A}$  which is best correlated to the actual residual, adds this member to the matrix of endmembers, updates the residual and computes the estimate of  $\mathbf{x}$  using the selected endmembers. The algorithm stops when a stop criterion is satisfied (in our case, when the actual residual is smaller than a preset threshold  $T$ ). A member from  $\mathbf{A}$  cannot be selected more than once, as the residual is orthogonalized with respect to the members already selected.

OMP may be used in any of the problems listed in Section 2.2. We consider, however, the

OMP variation proposed in [18] tailored to problems  $(P_0^+)$  and  $(P_0^{\delta+})$ , and which we denote by  $\text{OMP}^+$ . In this variation, the *Update solution* step in Algorithm 2.1 is modified to:

$$\mathbf{z}^i = \arg \min_{\mathbf{z}} \|\mathbf{D}\mathbf{z} - \mathbf{y}\| \quad \text{subject to} \quad \text{Support}\{\mathbf{z}^i\} = \mathcal{S}^i \quad \mathbf{z} > 0. \quad (2.23)$$

The OMP and  $\text{OMP}^+$  stopping rule is adapted either to solve exact or approximate problems. Considering that  $\varepsilon$  represents a measure of the error in the accuracy of the unmixing result, in the former case  $\varepsilon$  is very small ( $\varepsilon \rightarrow 0$ ), leading to the use of a small  $T$  as stopping threshold, whereas in the latter case  $\varepsilon > 0$ , which translates to setting a higher value for the stopping threshold  $T$  in Algorithm 2.1.

### 2.3.2 Basis Pursuit and Basis Pursuit Denoising Algorithms

In this work, we also use the recently introduced constrained sparse unmixing algorithm via variable splitting and augmented Lagrangian (CSUnSAL) [10] to solve the linear problems  $(P_1)$  and  $(P_1^+)$  and the quadratic problems  $(P_1^\delta)$  and  $(P_1^{\delta+})$ . CSUnSAL is tailored to hyperspectral applications with hundreds of thousands or millions of spectral vectors to unmix. This algorithm exploits the alternating direction method of multipliers (ADMM) [44] in a way similar to recent works [46] and [2]. Here, we use the acronyms CSUnSAL, CSUnSAL<sup>+</sup>, CSUnSAL<sup>δ</sup>, and CSUnSAL<sup>δ+</sup> to denote the variant of CSUnSAL tailored to  $(P_1)$ ,  $(P_1^+)$ ,  $(P_1^\delta)$ , and  $(P_1^{\delta+})$  problems, respectively.

### 2.3.3 Unconstrained Basis Pursuit and Basis Pursuit Denoising Algorithms

All the constrained optimization problems  $(P_1)$ ,  $(P_1^+)$ ,  $(P_1^\delta)$ , and  $(P_1^{\delta+})$  can be converted into unconstrained versions by minimizing the respective Lagrangian. For example, the problem  $(P_1^\delta)$  is equivalent to:

$$\min_{\mathbf{x}} \frac{1}{2} \|\mathbf{A}\mathbf{x} - \mathbf{y}\|_2^2 + \lambda \|\mathbf{x}\|_1. \quad (2.24)$$

The parameter  $\lambda > 0$  is the Lagrange multiplier and  $\lambda \rightarrow 0$  when  $\delta \rightarrow 0$ . This model, sometimes referred to as the least squares (LS)  $\ell_1$  model, is widely used in the signal processing community. It was used before to address the unmixing problem in [53], in which the endmembers were first extracted from the original image using the N-FINDR endmember extraction algorithm [95] and, then, the respective fractional abundances of the endmembers were inferred. However, the N-FINDR algorithm assumes the presence of pure pixels in the original image. According to our best knowledge, this approach was never used before to address the hyperspectral unmixing problem using spectral libraries.

In this work, we use the sparse unmixing algorithm via variable splitting and augmented Lagrangian (SUnSAL), introduced in [10], to solve problem (2.24). SUnSAL, as CSUnSAL, exploits the ADMM method [44] in a way similar to [2] and [46]. SUnSAL solves the unconstrained versions of  $(P_1)$ ,  $(P_1^+)$ ,  $(P_1^\delta)$ , and  $(P_1^{\delta+})$ . Hereinafter, we use the acronyms SUnSAL, SUnSAL<sup>+</sup>, SUnSAL <sup>$\delta$</sup> , and SUnSAL <sup>$\delta+$</sup>  to denote the respective variant.

It is important to emphasize that, by setting  $\lambda = 0$  in (2.24), one can arrive to a LS solution of the system, which is obtained by solving the unconstrained optimization problem:

$$(P^{\text{LS}}) : \min_{\mathbf{x}} \|\mathbf{y} - \mathbf{A}\mathbf{x}\|_2. \quad (2.25)$$

The solution of optimization problem (2.25) has poor behavior in terms of accuracy when the matrix of coefficients is ill-conditioned (as it is always the case in the sparse unmixing problem, in which we deal with fat matrices) or when the observations are affected by noise. However, one can take advantage of the physical constraints usually imposed in the unmixing problem (ANC and ASC) by plugging them into the objective function of  $(P^{\text{LS}})$ . Using this approach, we can simply arrive to the so-called non-negative constrained LS (NCLS) and fully constrained LS (FCLS) solutions in [55] by first activating the ANC and, then, by activating both the ANC and ASC constraints, respectively. In this chapter, we use SUnSAL to solve the constrained versions of the LS problem because, as mentioned before, they are particular cases of (2.24) when  $\lambda = 0$ .

---

**Algorithm 2.2** Pseudocode of the Iterative Spectral Mixture Analysis Algorithm.

---

**Part 1:**

**Initialization:**

Iteration:  $i = 1$

Initial spectral library:  $\mathbf{A}^1 \leftarrow \mathbf{A}$

**Main iteration:**

Compute solution:  $\mathbf{x}^i \leftarrow \arg \min_x \|\mathbf{A}^i \mathbf{x} - \mathbf{y}\|_2^2$

Compute  $\text{RMSE}^i \leftarrow \frac{1}{\sqrt{L}} \|\hat{\mathbf{y}} - \mathbf{y}\|_2$ , where  $\hat{\mathbf{y}} = \mathbf{A}^i \mathbf{x}^i$

Compute the member of  $\mathbf{A}^i$  having the lowest abundance:  $\text{index} \leftarrow \min_k (\mathbf{x}_1^k)$

Remove the member having the lowest fractional abundance from the spectral library:

$\mathbf{A}^i \leftarrow \mathbf{A}^i \setminus \mathbf{A}_{\text{index}}^i$

If  $\mathbf{A}$  still contains more than one member, update iteration:  $i \leftarrow i + 1$  and repeat **Main iteration**

**Part 2:**

Compute the variation of the RMSE for all iterations  $i_{\min} \leq i \leq m$ :  $\Delta \text{RMSE}_i = 1 - \text{RMSE}_{i-1} / \text{RMSE}_i$

(where  $i_{\min}$  is the minimum number of iterations before stopping the search)

Determine the position of the first substantial increase in the  $\Delta \text{RMSE}$  (*the critical iteration*):  $i_{\Delta \text{RMSE}_{\max}}$

The final solution is the solution computed in **Part 1** at the critical iteration

---

### 2.3.4 Iterative Spectral Mixture Analysis (ISMA)

In this work we also use the iterative spectral mixture analysis (ISMA) algorithm [80] to solve the considered problems. The pseudocode of ISMA is shown in Algorithm 2.2. ISMA is an iterative technique derived from the standard spectral mixture analysis formulation presented in Eq. (2.2). It finds an optimal endmember set by examining the change in the root mean square error (RMSE) after reconstructing the original scene using the fractional abundance estimations, as shown in Algorithm 2.2. The algorithm consists of two parts. In the first one, ISMA initially computes an unconstrained solution of the unmixing problem in Eq. (2.2), using all the spectral signatures available in a spectral library  $\mathbf{A}$ . Then, it removes the signature with the lowest estimated fractional abundance in  $\mathbf{x}^i$  and repeats the process with the remaining signatures, until only one signature remains. In the second part of the algorithm, a so-called critical iteration is identified as the iteration corresponding to the first abrupt change in the RMSE, computed as follows:

$$\Delta \text{RMSE} \equiv 1 - \left( \frac{\text{RMSE}_{j-1}}{\text{RMSE}_j} \right), \quad (2.26)$$

where  $\text{RMSE}_j$  is the RMSE corresponding to the  $j$ th iteration. The critical iteration corresponds to the optimal set of endmembers. The idea of recovering the true endmember set by analyzing the change in the RMSE is based on the fact that, before finding the optimal set of endmembers, the RMSE varies in certain (small) limits and it has a bigger variation when one endmember from the optimal set is removed, as the remaining endmembers are not sufficient to model with good accuracy the actual observation. It is important to emphasize that ISMA computes, at each iteration, an unconstrained solution instead of a constrained one. This is because it is predictable that, when the set of endmembers approaches the optimal one, the estimated fractional abundance vector  $\hat{\mathbf{x}}$  will actually approach  $\mathbf{x}$ , the true one.

## 2.4 Experiments with simulated data

In this section, we run a series of simulated data experiments which are mainly intended to address two fundamental questions:

1. What is the minimum sparsity of signals which are recoverable using hyperspectral libraries?
2. Among the optimization problems and respective algorithms, what are the more suitable ones to address hyperspectral SR problem?

The section is organized as follows. First, we describe the spectral libraries used in our simulated data experiments and the performance discriminators. Then, we compute approximate solutions without imposing the ASC (due to the reasoning showed in subsection 2.2.1) for simulated mixtures, using the techniques described in section 2.3. We do not address the unmixing problem when the observations are not affected by noise since, in this case, and for the levels of sparsity considered, all the methods were able to recover the correct solution. Further, we present a comparison of the algorithms used to solve the unmixing problem from two viewpoints: their computational complexity, and their behavior with different noise levels. Next, a short example is dedicated to the case when the ASC holds, for one particular library and with observations

affected by correlated noise. The last experiment of this section exemplifies the application of sparse unmixing techniques to spectral libraries composed by image-derived endmembers, an approach that can be adopted if no spectral library is available *a priori*. The section concludes with a summary of the most important aspects observed in our simulated data experiments.

### 2.4.1 Spectral Libraries Used in Simulated Data Experiments

We have considered the following spectral libraries in our experiments:

- $\mathbf{A}_1 \in \mathbb{R}^{224 \times 498}$ : A selection of 498 materials (different mineral types) from the USGS library denoted splib06<sup>3</sup> and released in September 2007. The reflectance values are measured for 224 spectral bands distributed uniformly in the interval  $0.4\text{--}2.5\mu\text{m}$ .
- $\mathbf{A}_2 \in \mathbb{R}^{224 \times 342}$ : Subset of  $\mathbf{A}_1$ , where the angle between any two different columns is larger than  $3^\circ$ . We have made this pruning because there are many signatures in  $\mathbf{A}_1$  which correspond to very small variations, including scalings, of the same material.
- $\mathbf{A}_3 \in \mathbb{R}^{224 \times 500}$ : A selection of 500 materials generated using a spectral library generator tool, which allows an user to create a spectral library starting from the ASTER library<sup>4</sup>, a compilation of over 2400 spectra of natural and man-made materials. Specifically, each of the members has the reflectance values measured for 224 spectral bands distributed uniformly in the interval  $3\text{--}12\mu\text{m}$ . In this library, there were selected spectra corresponding to materials of the following types: man-made (30), minerals (265), rocks (130), soil (40), water (2), vegetation (2), frost/snow/ice (1) and stony meteorites (30). Notice that, in a real scenario, a library like this is not likely to be used, as it is expected that a given mixture does not contain materials of so many different types. Although real hyperspectral images are acquired usually in a narrower range of wavelengths, this library represents an interesting case study since it is highly heterogeneous from the viewpoint of the type of materials that actually compose it, compared to  $\mathbf{A}_1$  and  $\mathbf{A}_2$  (which contain only mineral

---

<sup>3</sup>Available online: <http://speclab.cr.usgs.gov/spectral.lib06>

<sup>4</sup>Available online: <http://speclib.jpl.nasa.gov>



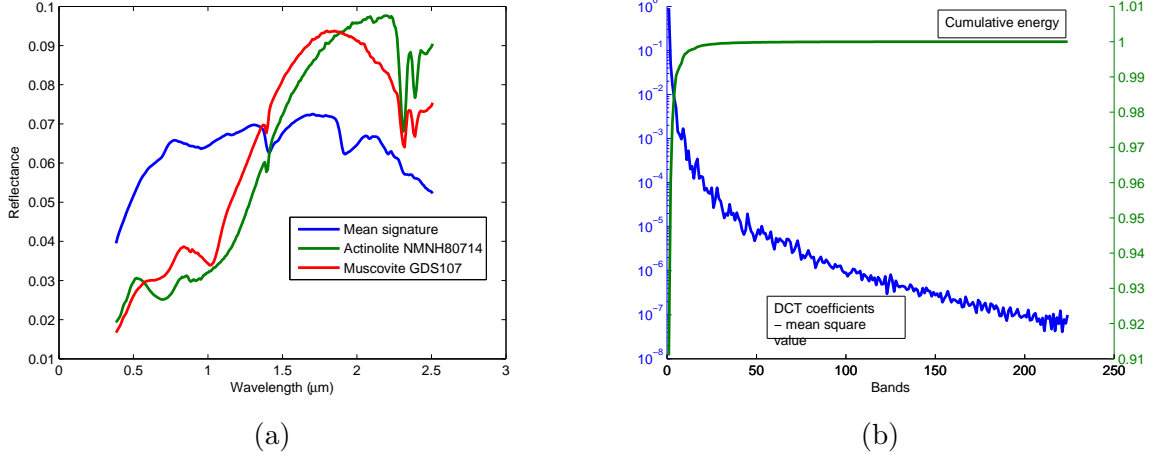


Figure 2.3: (a) Mean signature and two other signatures randomly chosen from library  $\mathbf{A}_1$ . (b) DCT coefficients and cumulative energy.

spectra). At the same time, using this library leads to more challenging unmixing problem due to the internal characteristics of the library, as it will be seen further.

- $\mathbf{A}_4 \in \mathbb{R}^{224 \times 449}$ : Subset of  $\mathbf{A}_3$ , generated following the same reasonings as for  $\mathbf{A}_2$ .

For comparative purposes, we also consider the following two libraries made of i.i.d components:

- $\mathbf{A}_5 \in \mathbb{R}^{224 \times 440}$ : made of i.i.d. Gaussian components of zero mean and variance one
- $\mathbf{A}_6 \in \mathbb{R}^{224 \times 440}$ : made of i.i.d. components uniformly distributed in the interval  $[0, 1]$ .

Fig. 2.3(a) plots the mean signature and two other signatures randomly chosen from library  $\mathbf{A}_1$ . All the curves shown are non-negative and relatively smooth. These characteristics can also be seen in Fig. 2.3(b), which plots the mean square value of the DCT coefficients computed over all signatures of the library  $\mathbf{A}_1$  jointly with their cumulative energy. From this plot, we conclude that 99.9% of the energy is contained in the first 21 coefficients. If we assume that (from a practical point of view) the remaining coefficients are zero, then the spark of  $\mathbf{A}_1$  should be no larger than 21. This results from the following:

1. Computing the DCT of the columns of  $\mathbf{A}$  is equivalent to left multiplying  $\mathbf{A}$  by an unitary  $L \times L$  matrix, which, therefore, does not change the  $\text{spark}(\mathbf{A})$ .

Table 2.1: Mutual Coherence Values and Estimation of the Spark for Different Spectral Libraries.

Spectral library	$\mathbf{A}_1$	$\mathbf{A}_2$	$\mathbf{A}_3$	$\mathbf{A}_4$	$\mathbf{A}_5$	$\mathbf{A}_6$
Description	USGS	USGS pruned	ASTER	ASTER pruned	i.i.d. Gaussian	i.i.d. Uniform
Number of spectra ( $t$ )	498	342	500	449	440	440
Number of spectral bands ( $L$ )	224	224	224	224	220	220
Minimum wavelength ( $w_{min}$ ) in $\mu\text{m}$	0.4	0.4	3	3	-	-
Maximum wavelength ( $w_{max}$ ) in $\mu\text{m}$	2.5	2.5	12	12	-	-
spark( $\mathbf{A}$ ) (upper bound)	21	23	30	54	221	221
Mutual coherence $\mu(S)$	0.99998	0.9986	1	0.9986	0.3141	0.8388

- Any matrix with zero elements for any line greater than a given natural  $l$ , has rank no larger than  $l$ .

Table 2.1 characterizes the libraries  $\mathbf{A}_1$  to  $\mathbf{A}_6$ . We draw attention on the very high values of the coherence for the spectral libraries (both original and pruned versions). The upper limits of the spark values for libraries  $\mathbf{A}_1$  to  $\mathbf{A}_4$  anticipate difficulties in the SR. These difficulties are somehow mitigated by the very low level of sparsity of the signal in which we are interested. On the other hand, it is important to emphasize that libraries composed by i.i.d. components (similar to  $\mathbf{A}_5$  and  $\mathbf{A}_6$ ) have been used extensively in the literature in order to investigate the ability of different algorithms to deal with under-determined systems of equations. In a sparse unmixing context, the use of these libraries is mainly intended to preliminarily validate the algorithms used. This is because these libraries represent ideal situations that are never encountered in real scenarios, as it can be concluded from Table 2.1. In the following subsections we present a series of simulation results based on the aforementioned libraries and aimed at assessing the potential of SR techniques in the context of hyperspectral unmixing applications.

#### 2.4.2 Performance Discriminators

Before presenting our experimental results, it is first important to describe the parameter settings and performance discrimination metrics adopted in our experiments. Regarding parameter settings, the algorithms described in section 2.3 have been applied to unmix simulated mixtures containing a number of endmembers (i.e. values of the sparsity level) which ranges from 2 to 20. For each considered cardinality, spectral library and noise level, we generated 100 mixtures containing random members from the library. The fractional abundances were

randomly generated following a Dirichlet distribution [69]. ISMA, OMP and OMP+ algorithms were constrained to return solutions having at most 30 endmembers (we assume that it is not plausible that a mixed pixel contains more materials). Also, the RMSE variation for ISMA ( $\Delta\text{RMSE}$ ) was simply related to the difference between two consecutive values of the RMSE:  $\Delta\text{RMSE}_i \equiv \text{RMSE}_i - \text{RMSE}_{i-1}$ . We remind that ISMA is a per-pixel optimization method. This means that the stopping criterion should be individually set for each pixel separately, which is impossible in real scenes with thousands or tens of thousands of pixels. In our experiments, the stopping criterion was set for a large number of samples at once. The semi-optimal parameters that we have set empirically in our experiments are reported in an Appendix (see Table 2.4 for additional details). It is important to emphasize that, in Table 2.4 and in all the following figures, the algorithms: OMP, ISMA, SUnSAL and CSUnSAL are used to solve the unmixing problems  $(P_1)$  and  $(P_1^\delta)$ , whereas SUnSAL+ and CSUnSAL+ algorithms are used to solve the problems  $(P_1^+)$  and  $(P_1^{\delta+})$ . Finally, algorithms SUnSAL+D and CSUnSAL+D solve the modified problems shown in (2.15). SUnSAL solves also the NCLS problem. It is also important to note that algorithms OMP+, SUnSAL+D and CSUnSAL+D were not applied for the library  $(\mathbf{A}_5)$ , as the corresponding technique is dedicated to nonnegative signals.

Regarding the adopted performance discriminators, the quality of the reconstruction of a spectral mixture was measured using the signal to reconstruction error:  $\text{SRE} \equiv E[\|\mathbf{x}\|_2^2]/E[\|\mathbf{x} - \hat{\mathbf{x}}\|_2^2]$ , measured in dB:  $\text{SRE}(\text{dB}) \equiv 10 \log_{10}(\text{SRE})$ . We use this error measure, instead of the classical root-mean-squared error (RMSE), as it gives more information regarding the power of the error in relation with the power of the signal. We also computed a so-called “probability of success”,  $p_s$ , which is an estimate of the probability that the relative error power be smaller than a certain threshold. This metric is a widespread one in sparse regression literature, and is formally defined as follows:  $p_s \equiv P(\|\hat{x} - x\|^2/\|x\|^2 \leq \text{threshold})$ . For example, if we set  $\text{threshold} = 10$  and get  $p_s = 1$  this means that the total relative error power of the fractional abundances is, with probability one, less than  $\frac{1}{10}$ . This gives an indication about the stability of the estimation that is not inferable directly from the SRE (which is an average). In our case, the estimation

result is considered successful when  $\|\hat{x} - x\|^2 / \|x\|^2 \leq 3.16$  (5dB). In all the following figures related to the SRE(dB), we plot a dashed blue line representing the 5dB level in all situations in which at least one of the algorithms reaches this value. The main rationale for using this threshold is that, after inspecting the results of different unmixing scenarios, we concluded that a reconstruction attaining SRE(dB) = 5dB is still useful. To illustrate this situation, we simulated a toy hyperspectral image with dimensions  $15 \times 15$  pixels using the spectral library  $\mathbf{A}_1$ . We assumed the presence of 5 randomly selected endmembers in all simulated pixels, with all observations affected by white noise with signal-to-noise ratio ( $\text{SNR} \equiv \|\mathbf{Ax}\|^2 / \|\mathbf{n}\|_2^2$ ) given by  $\text{SNR} = 40\text{dB}$ . For better visual perception of the unmixing results, the fractional abundance of one of the endmembers follows a deterministic pattern (say, a staircase shape with fifteen values comprised between 0 and 1) with the other abundances generated randomly (such that the ASC holds in each pixel). Fig. 2.4 shows the true and the inferred abundance maps obtained for the first endmember when  $\text{SRE(dB)} = 5.3\text{dB}$  after applying the SUnSAL algorithm. Fig. 2.4 also shows the true and reconstructed reflectance values at spectral band number 100 ( $1.28 \mu\text{m}$ ) of our toy hyperspectral image. Finally, the last row of Fig. 2.4 shows the difference images (which represent the per-pixel differences between the images in the top and middle rows of the same figure) in order to represent the magnitude of the errors that occurred in the estimation of fractional abundances and in the image reconstruction at the considered spectral band. Note the low values of the errors achieved in both cases. The simple toy example in Fig. 2.4 indicates that a reconstruction with  $\text{SRE(dB)} \geq 5\text{dB}$  can be considered of good accuracy. Fig. 2.5 also shows the true and the reconstructed spectra of a randomly selected pixel in our toy hyperspectral image. In Fig. 2.5, the reconstructed spectrum was obtained for  $\text{SRE(dB)} = 4.8\text{dB}$ . Moreover, while in this example the noise was set to a low value, in the following tests the observations are affected by higher noise ( $\text{SNR} = 30\text{dB}$ ) meaning that the chosen threshold is even more powerful in terms of performance discrimination.

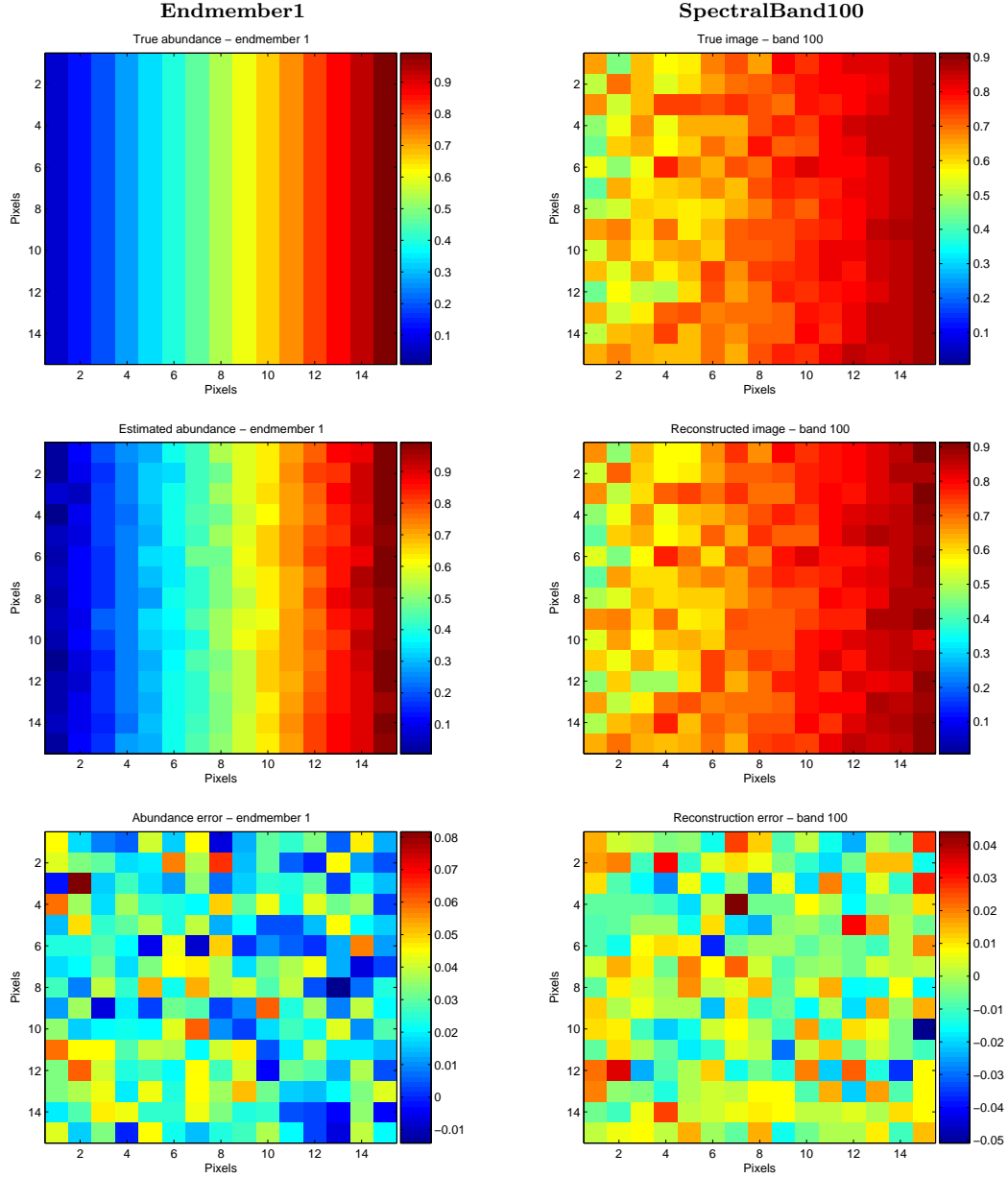


Figure 2.4: Toy example illustrating the reconstruction quality obtained for  $\text{SRE(dB)} \approx 5\text{dB}$ . The figures at the top respectively represent the abundance fractions of an endmember and the reflectance values of spectral band 100 ( $1.28 \mu\text{m}$ ) in the toy hyperspectral image, the figures in the middle represent the respective estimations using SUNSAL algorithm, while the figures at the bottom show the corresponding differences between the true and the estimated values in both cases.

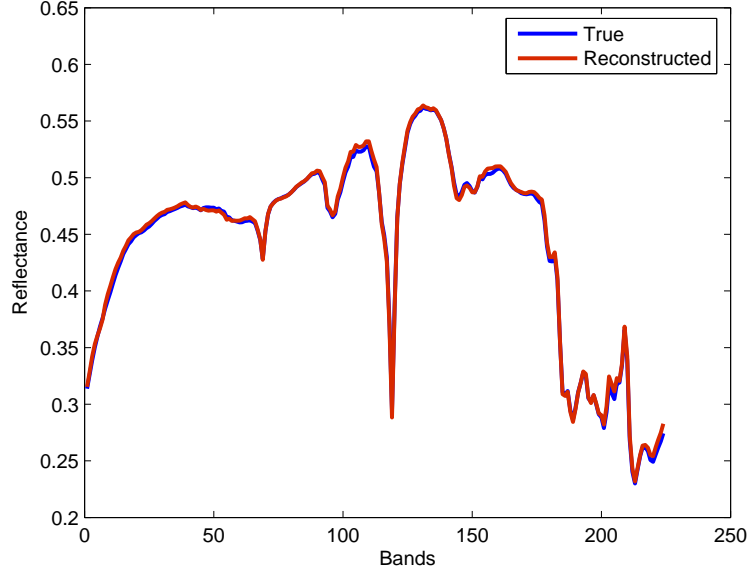


Figure 2.5: True (blue) and reconstructed (red) spectra of a randomly selected pixel in a toy hyperspectral image simulated with  $\text{SRE}(\text{dB}) = 5.2\text{dB}$ .

### 2.4.3 Calculation of Approximate Solutions Without Imposing the ASC Constraint

In this subsection, we consider that the observations are affected by noise, i.e.  $\mathbf{n} \neq 0$ . The SNR was set to 30dB. This noise level was chosen after analyzing the SNR estimated using the VCA [69] algorithm<sup>5</sup> in several real hyperspectral images, and for different values of the number of endmembers assumed to be present in the respective scenes.

It is important to emphasize that the additive perturbation in the model described in Eq. (2.2) may be motivated by several causes, including system noise, Poisson noise related with the photon counting process, and modeling errors related with deviations in the spectral signatures resulting from atmospheric interferers, or nonlinearities in the observation mechanism. The first two causes usually introduce band uncorrelated noise, whereas the latter one yields band correlated noise. In hyperspectral imaging applications, we argue that correlated noise is a major concern since it is very difficult to calibrate the observations resulting from an airborne/spaceborne sensor with regards to those in a spectral library of signatures acquired in a laboratory and free of atmospheric interferers, let alone spectral variability issues. Taking into

<sup>5</sup>Demo available on-line at <http://www.lx.it.pt/bioucas/code.htm>

account that, in real applications, the noise is highly correlated as it represents mainly modeling noise and the spectra are of low-pass type with respect to the wavelength, in our simulations we considered white noise on the one hand and, on the other, colored noise resulting from low-pass filtering i.i.d. Gaussian noise, using a normalized cut-off frequency of  $5\pi/L$ . For a given mixture, the unmixing process was again considered successful when  $\text{SRE}(\text{dB}) \geq 5\text{dB}$ . In the following, we describe our experiments assuming white and correlated noise, respectively.

### Experiments Assuming White Noise

Fig. 2.6 shows the  $\text{SRE}(\text{dB})$  obtained for our simulated observations affected by white noise. Similarly, Fig. 2.7 shows the probability of success  $p_s$  achieved by each method for the simulated observations affected by white noise. It should be noted that we removed the curves corresponding to algorithms with poor behavior from the plots in Figs. 2.6 and 2.7. From these figures, we can conclude that pruning the libraries can improve the performances of the algorithms when the observations are affected by white noise. Fig. 2.7 shows that the highest probability of success is achieved by SUNSAL (specifically, by its positive constrained version) and NCLS. The library  $\mathbf{A}_3$  seems to be the most difficult one to treat for all methods (being the most coherent matrix), but its pruned version is much more accessible. CSUnSAL particularly exhibits a significant performance improvement when pruning the libraries. For the libraries composed by real signatures:  $\mathbf{A}_1 \dots \mathbf{A}_4$ , the probability of success is low for all the methods when the cardinality is higher than 10. Nevertheless, in a sparse unmixing framework we are interested in solutions with a smaller number of endmembers, say, up to 5 endmembers per pixel. For the libraries composed by i.i.d. entries, all the methods exhibit good behavior. For the other libraries, ISMA and OMP exhibit poor results.

### Experiments Assuming Correlated noise

Fig. 2.8 shows the  $\text{SRE}(\text{dB})$  obtained for our simulated observations affected by correlated noise. Similarly, Fig. 2.9 shows the probability of success  $p_s$  obtained for our simulated observations affected by correlated noise. From the viewpoint of our considered problem, perhaps this is the

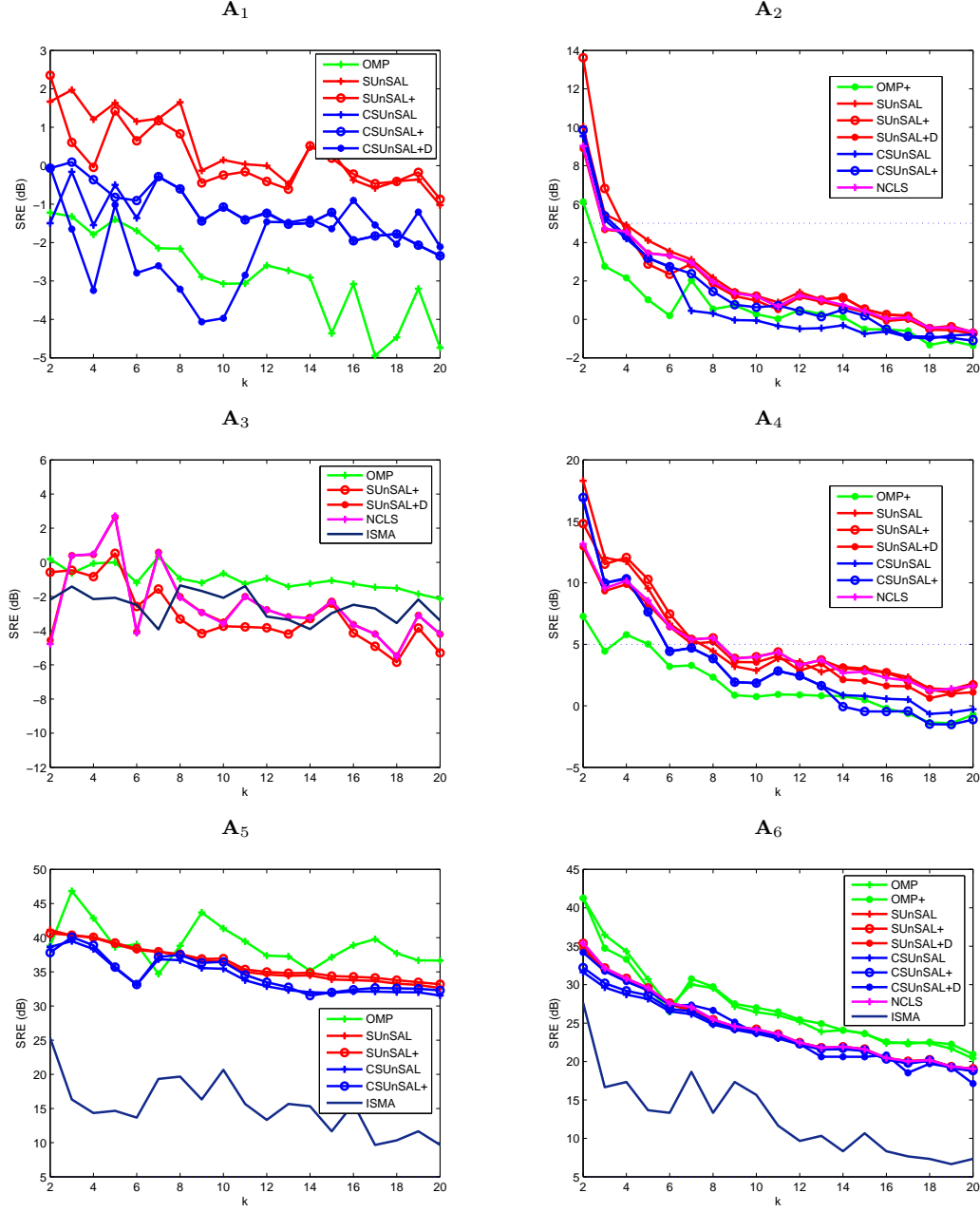


Figure 2.6: Plot of the SRE(dB) values (as a function of the number of endmembers) obtained by the different sparse unmixing methods when applied to the simulated data with white noise (SNR=30dB), using different spectral libraries.



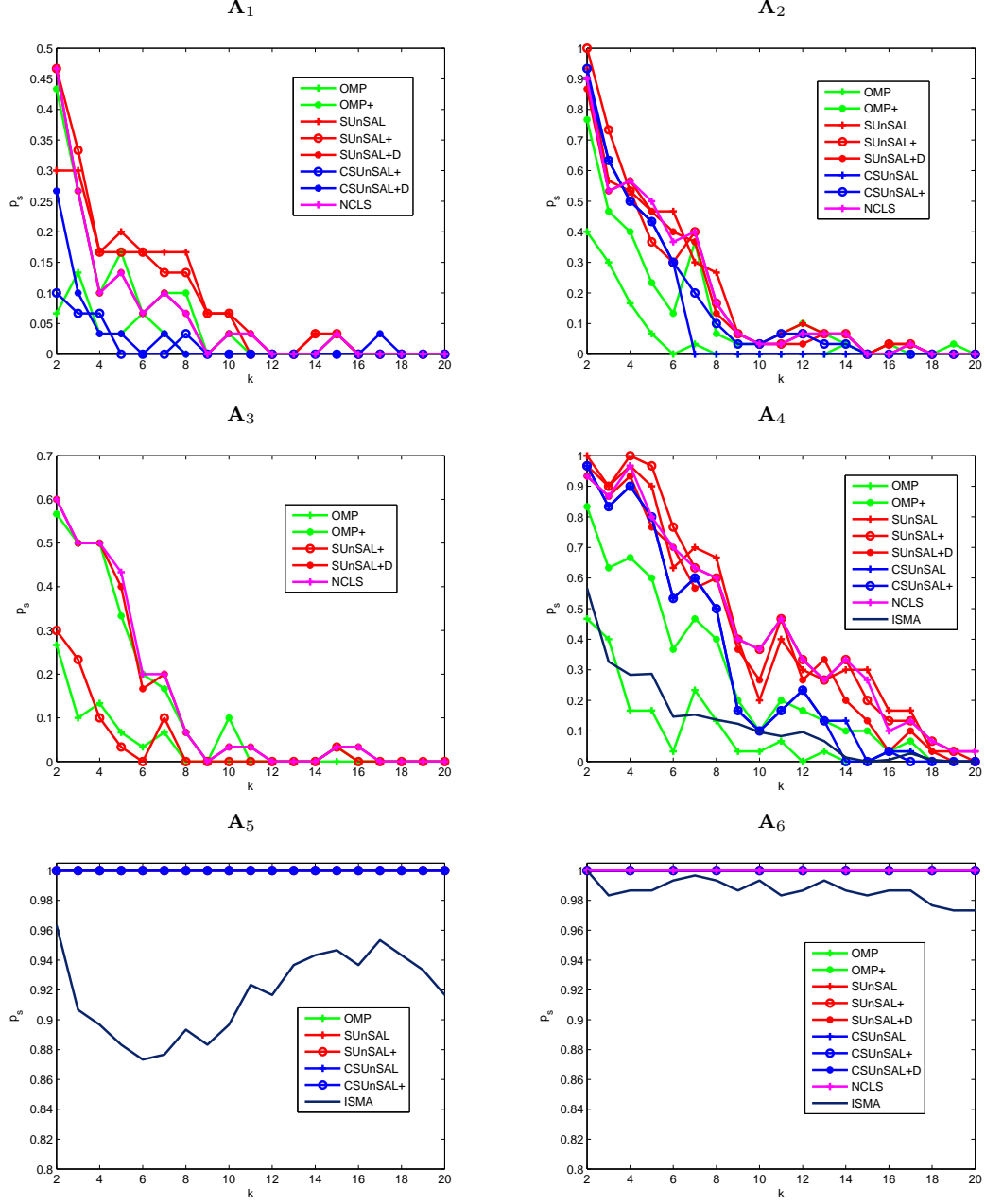


Figure 2.7: Plot of the  $p_s$  values (as a function of the number of endmembers) obtained by the different sparse unmixing methods when applied to the simulated data with white noise (SNR=30dB), using different spectral libraries.

most interesting case study since noise in the hyperspectral images is usually correlated. From Figs. 2.8 and 2.9, it can be observed that most considered sparse unmixing methods exhibit better performance when applied to observations affected by colored noise. As in previous (and subsequent) experiments, we removed the curves corresponding to algorithms with poor behavior. For the libraries composed by real signatures, the highest probability of success is achieved by CSUnSAL and/or its variants, followed closely by the unconstrained version of SUnSAL (see the plots for the most difficult cases, corresponding to  $\mathbf{A}_1$  and  $\mathbf{A}_3$ ). This result confirms our introspection that imposing sparsity can lead to improved results in the context of hyperspectral unmixing problems using spectral libraries.

#### 2.4.4 Comparison of Unmixing Algorithms with Regards to Computational Complexity

An important issue in the evaluation of sparse unmixing algorithms is their computational complexity, in particular, when large spectral libraries are used to solve the unmixing problem. In this regard, we emphasize that both OMP (and its variations) and ISMA are computationally complex, with cubic running time  $O(L^3)$ . All remaining algorithms (NCLS, FCLS, SUnSAL and its variations, CSUnSAL and its variations) have the same theoretical complexity, with quadratic running time  $O(L^2)$ . A more detailed comparison reporting the actual algorithm running times in the task of unmixing a real hyperspectral scene are given (for the same computing environment) in Section 2.5.

#### 2.4.5 Comparison of Unmixing Algorithms in the Presence of Different Noise Levels

In this subsection we compare the performances of the considered sparse unmixing algorithms with different noise levels. Specifically, we consider SNR levels of 20, 30, 40 and 50dB, both for white and correlated noise. In this experiment, the observations were generated by assuming a fixed cardinality of the solution:  $k = 5$ . Fig. 2.10 shows the SRE(dB) as a function of the noise

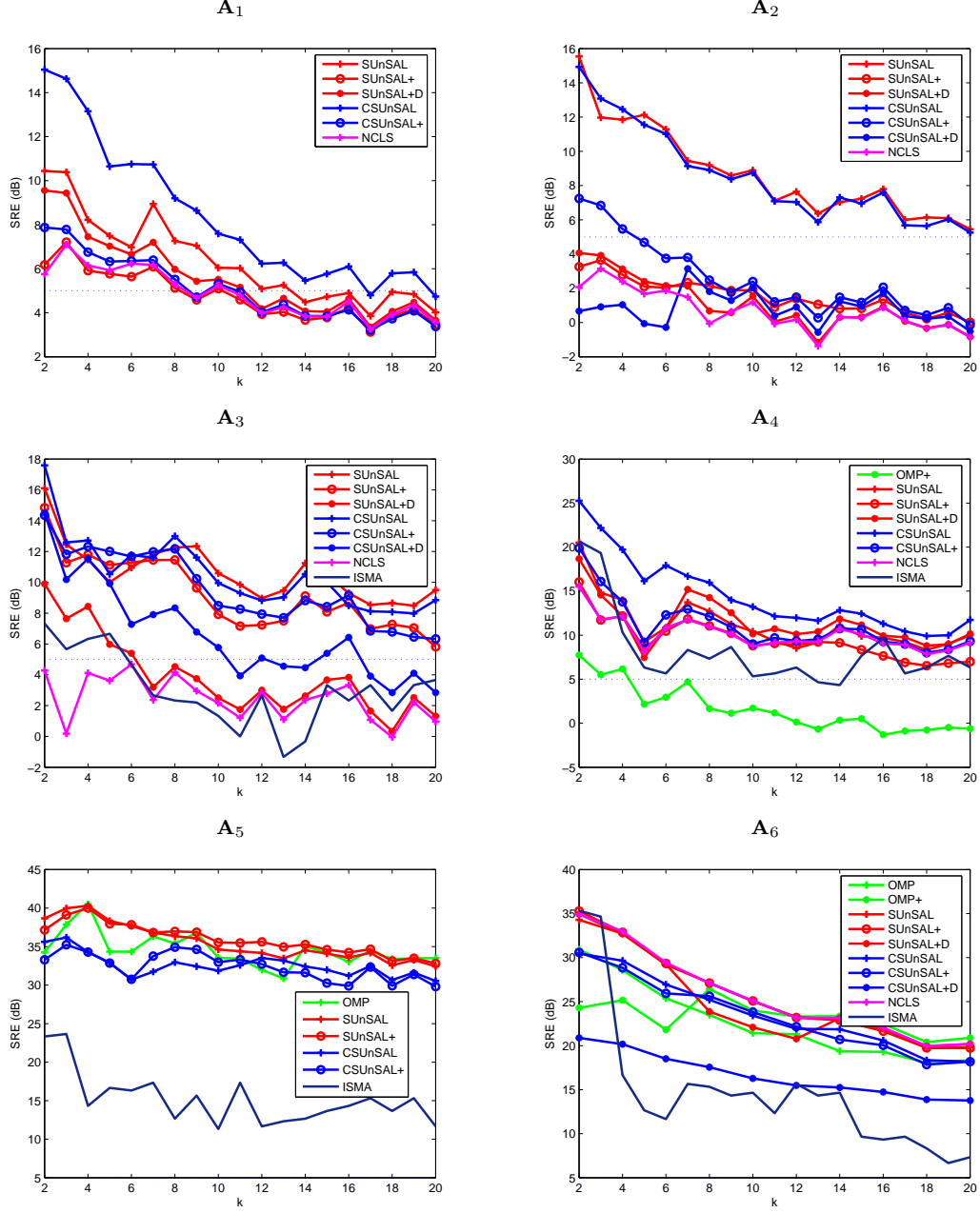


Figure 2.8: Plot of the SRE(dB) values (as a function of the number of endmembers) obtained by the different sparse unmixing methods when applied to the simulated data with correlated noise (SNR=30dB), using different spectral libraries.

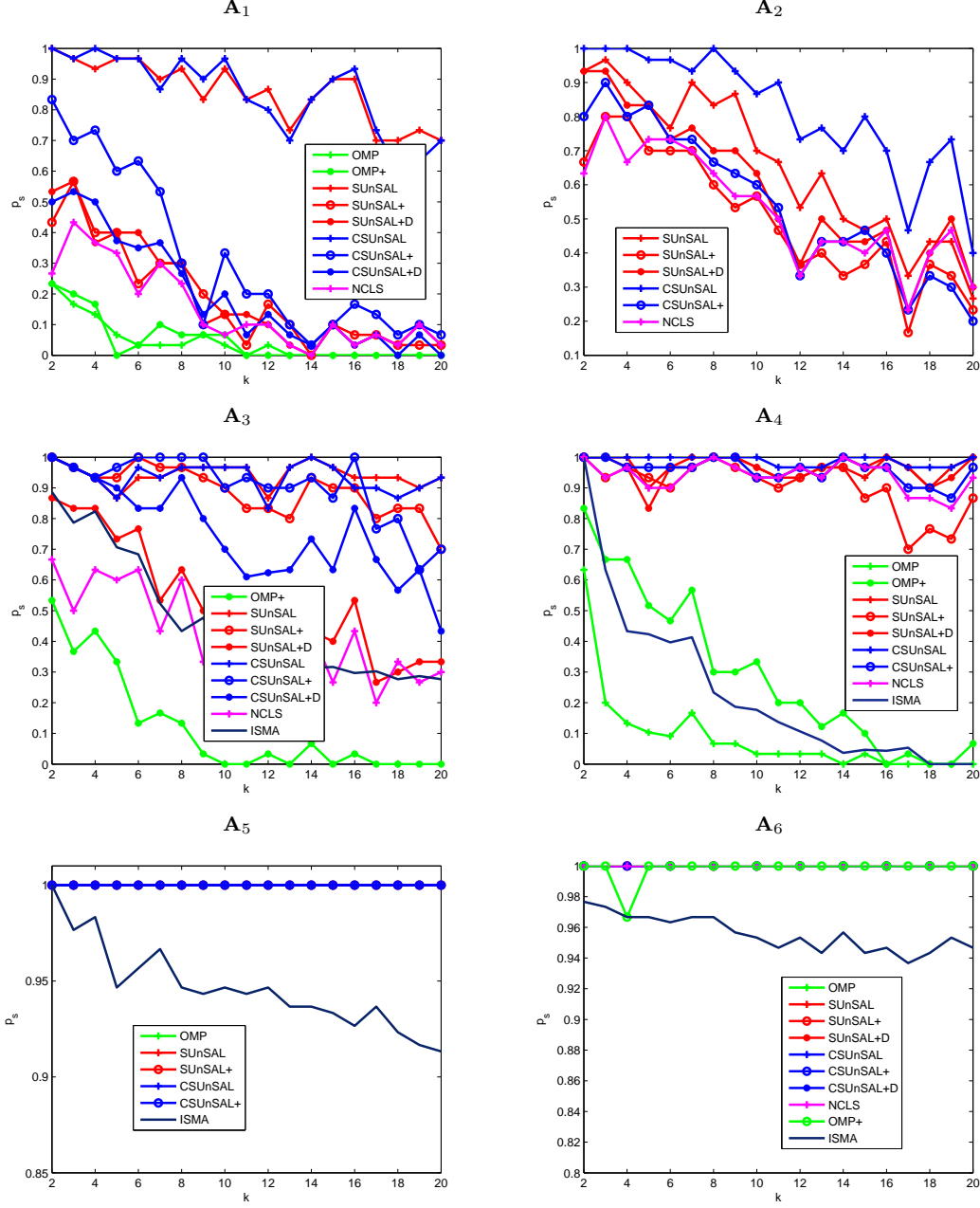


Figure 2.9: Plot of the  $p_s$  values (as a function of the number of endmembers) obtained by the different sparse unmixing methods when applied to the simulated data with correlated noise (SNR=30dB), using different spectral libraries.

level affecting the measurements in the case of white noise, while Fig. 2.11 shows the the same plots in the case of measurements affected by correlated noise, for different spectral libraries. Again we removed the curves corresponding to algorithms with poor behavior. The algorithm parameters in this experiment were set using the procedure described in the Appendix (see Table 2.5). From Figs. 2.10 and 2.11, we can conclude that the performance of the algorithms decreases when the noise increases, as expected. In general, the algorithm behavior observed in previous simulated scenarios is confirmed here, with the general trend that most considered approaches perform better in the presence of correlated noise rather than in the presence of white noise. For the white noise scenario, both SUnSAL and SUnSAL+ generally provide the highest values of SRE(dB), particularly for high SNR values. For the correlated noise scenario, CSUnSAL and its variation CSUnSAL+ generally provide the highest scores of SRE(dB), with the exception of spectral library  $\mathbf{A}_6$  for which NCLS provides the highest error scores as it was already the case in previous experiments. To conclude this subsection, it is worth mentioning that we not only evaluated the performance of the proposed method with different libraries and fixed cardinality of the solution (as illustrated in Figs. 2.10 and 2.11), but also with a fixed library and variable cardinality of the solution. For instance, extensive experiments conducted using only the library  $\mathbf{A}_1$  for different cardinalities of the solution (not included here for space considerations) led to the same conclusions obtained using all the libraries.

#### 2.4.6 Calculation of Approximate Solutions Imposing the ASC Constraint

This subsection discusses the results obtained in a noisy environment by the techniques presented in section 2.3 which include the ASC constraint, denoted by  $\text{SUnSAL}^{\text{ASC}}$  (which solves here also the FCLS problem) and  $\text{CSUnSAL}^{\text{ASC}}$ . The simulated data were generated as explained in subsection 2.4.3 but this time imposing the ASC constraint, and adding both white and correlated noise to the simulated observations. The spectral library used in this example is  $\mathbf{A}_1$ . When the ASC holds,  $\text{SUnSAL}^{\text{ASC}}$  is equal to FCLS since, no matter how the parameter  $\lambda$  is chosen, the sparsity enforcing term does not play any role (it is a constant). As a consequence,

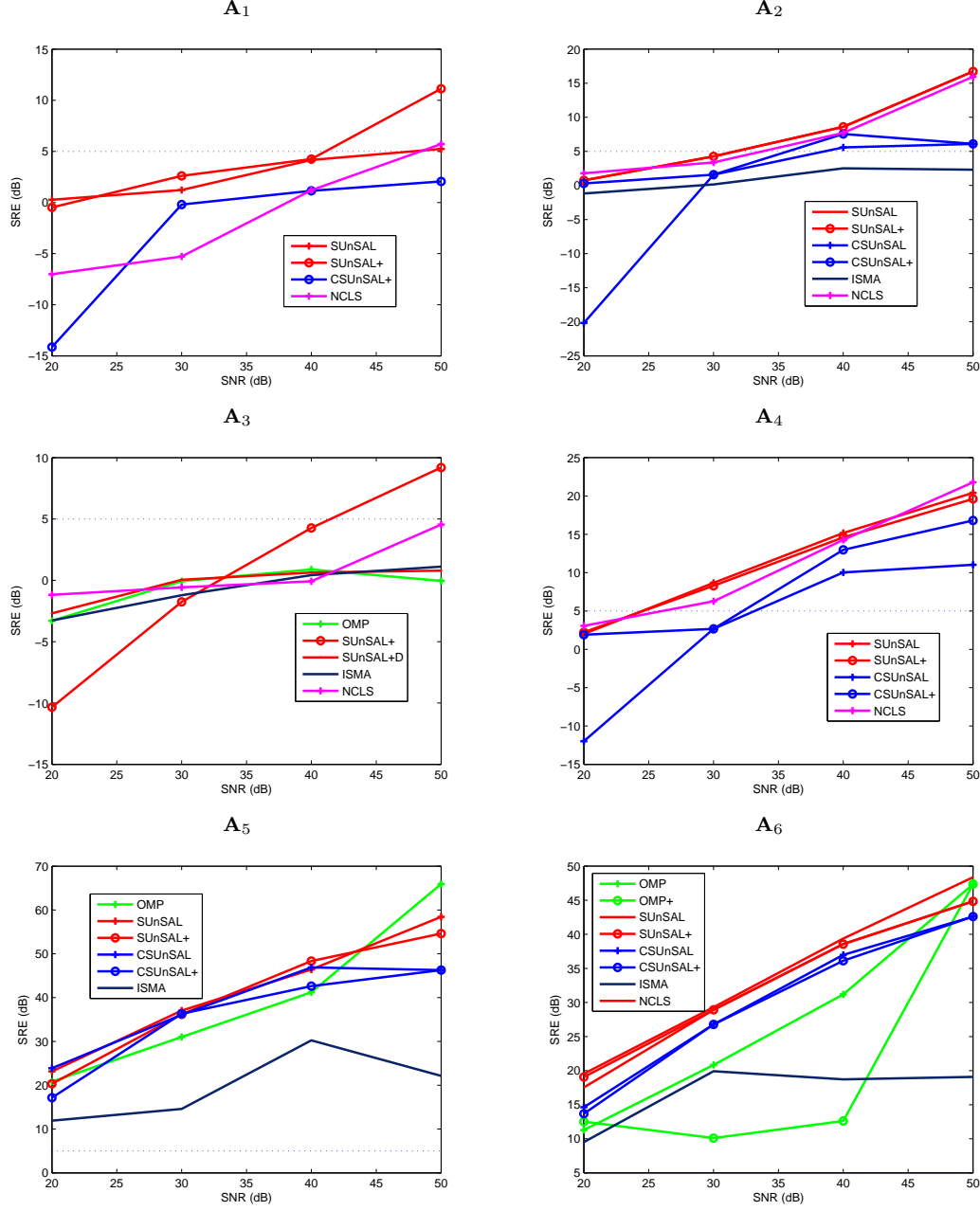


Figure 2.10: Plot of the SRE(dB) values (as a function of the considered SNR) obtained by the different sparse unmixing methods when applied to the simulated data with white noise, using different spectral libraries.

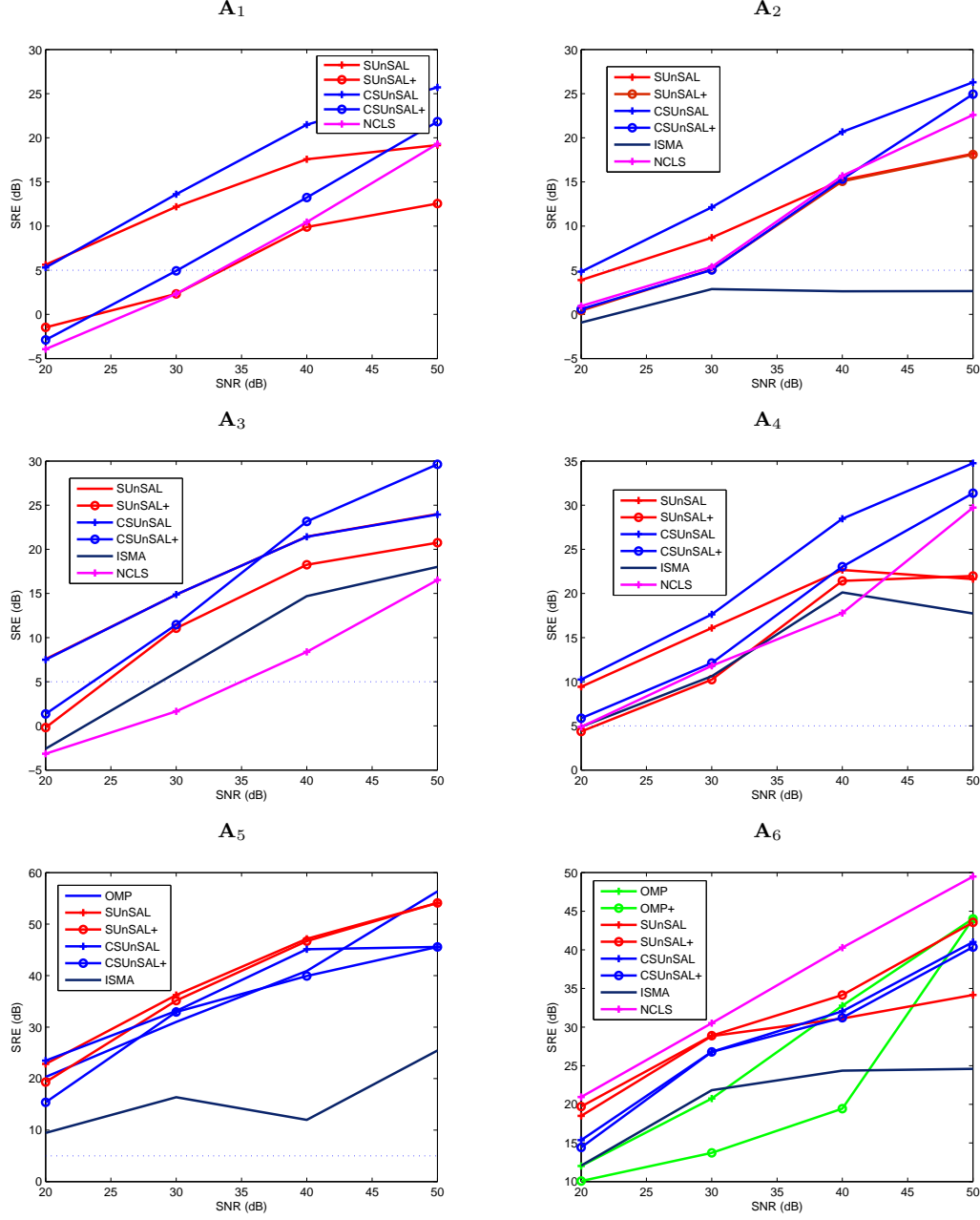


Figure 2.11: Plot of the SRE(dB) values (as a function of the considered SNR) obtained by the different sparse unmixing methods when applied to the simulated data with correlated noise, using different spectral libraries.

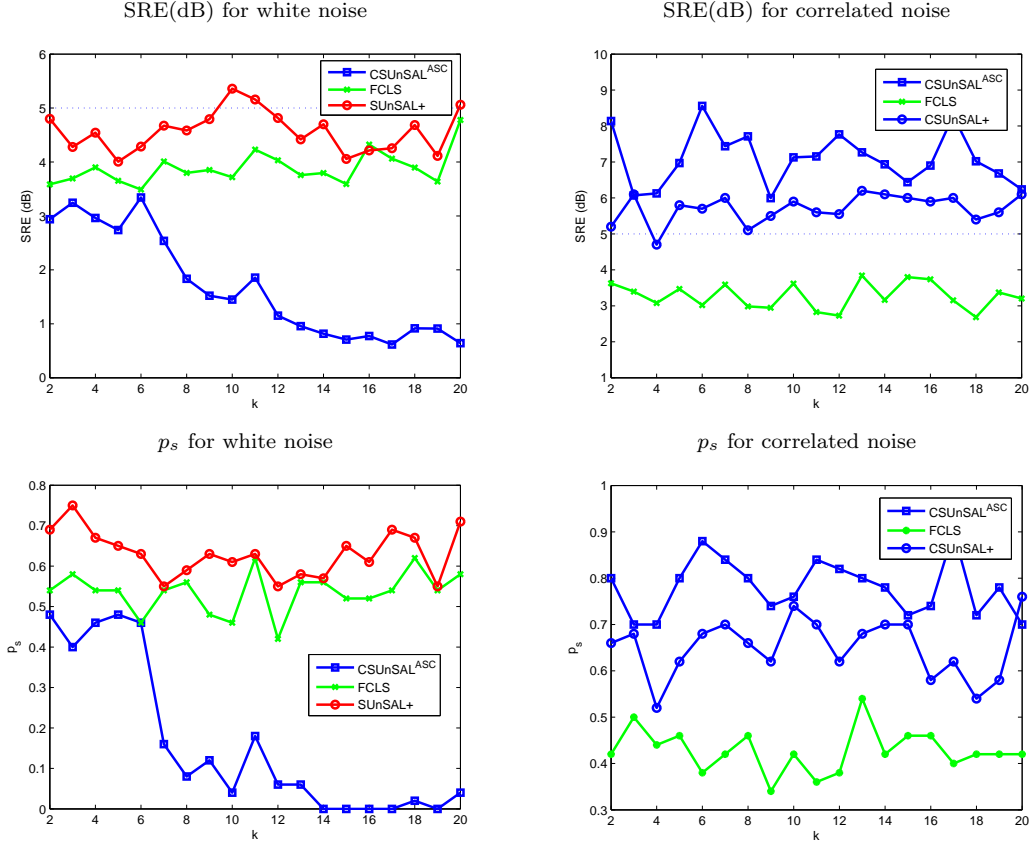


Figure 2.12: Plot of the SRE(dB) and  $p_s$  values (as a function of the number of endmembers) obtained by the different sparse unmixing methods including the ASC constraint when applied to the simulated data with white and correlated noise, using spectral library  $\mathbf{A}_1$

we do not plot here the results obtained by  $\text{SUnSAL}^{\text{ASC}}$ , but, instead, the results obtained by  $\text{SUnSAL}+$  and  $\text{CSUnSAL}+$  for white noise and correlated noise, respectively. Fig. 2.12 shows the values of SRE(dB) and  $p_s$  for the two considered cases (white and correlated noise). These results exemplify the behavior of the constrained unmixing algorithms in the hypothetical situation in which the ASC constraint holds, an assumption that is not always true in real unmixing scenarios due to signature variability issues as explained in subsection 2.2.1. Fig. 2.12 shows that the performances of  $\text{SUnSAL}+$  and FCLS are quite similar (with a small advantage for  $\text{SUnSAL}+$ ) and generally superior to those achieved by  $\text{CSUnSAL}^{\text{ASC}}$  for white noise, while both  $\text{CSUnSAL}+$  and  $\text{CSUnSAL}^{\text{ASC}}$  exhibit a significant performance improvement with regards to FCLS when applied to unmix observations affected by correlated noise, especially for high cardinalities of the solution.



#### 2.4.7 Application of sparse unmixing techniques to image-derived endmembers

The main goal of this experiment is to analyze the performance of sparse unmixing techniques when a spectral library is not available *a priori*. In this case, the proposed methods can still be applied by resorting to an artificially generated spectral library constructed using image-derived endmembers. In our experiment, we first derived a subset of 12 members from library  $\mathbf{A}_1$  (the subset was generated after retaining only the spectral signatures which form a spectral angle larger than  $20^\circ$  with all other signatures in the library). Then, we randomly selected five of the spectral signatures in the resulting subset and used them to generate a simulated hyperspectral image with  $75 \times 75$  pixels and 224 bands per pixel. The data were generated using a linear mixture model, using the five randomly selected signatures as the endmembers and imposing the ASC in each simulated pixel. In the resulting image, illustrated in Fig. 2.13(a), there are pure regions as well as mixed regions constructed using mixtures ranging between two and five endmembers, distributed spatially in the form of distinct square regions. Figs. 2.13(b)–(e) respectively show the true fractional abundances for each of the five endmembers. The background pixels are made up of a mixture of the same five endmembers, but this time their respective fractional abundances values were fixed to 0.5130, 0.1476, 0.1158, 0.1242 and 0.0994, respectively. The simulated data was then contaminated with noise (SNR=20dB).

Once the simulated data set was generated, we used the HySime algorithm [12] to find the signal subspace and projected the data on this subspace. Then, two endmember extraction algorithms: VCA and N-FINDR were used to automatically extract the endmembers from the simulated data. The obtained endmember sets were merged in order to construct the spectral library used in the sparse unmixing process. In this library, only materials with spectral angle of at least  $3^\circ$  with regards to other materials in the library were retained in order to avoid strong similarities between the spectral signatures when conducting the sparse unmixing process. The abundance estimation was then conducted with SUnSAL+, using different values of the parameter  $\lambda$ . The same algorithm was used to find the NCLS solution by setting  $\lambda = 0$ . Finally, the

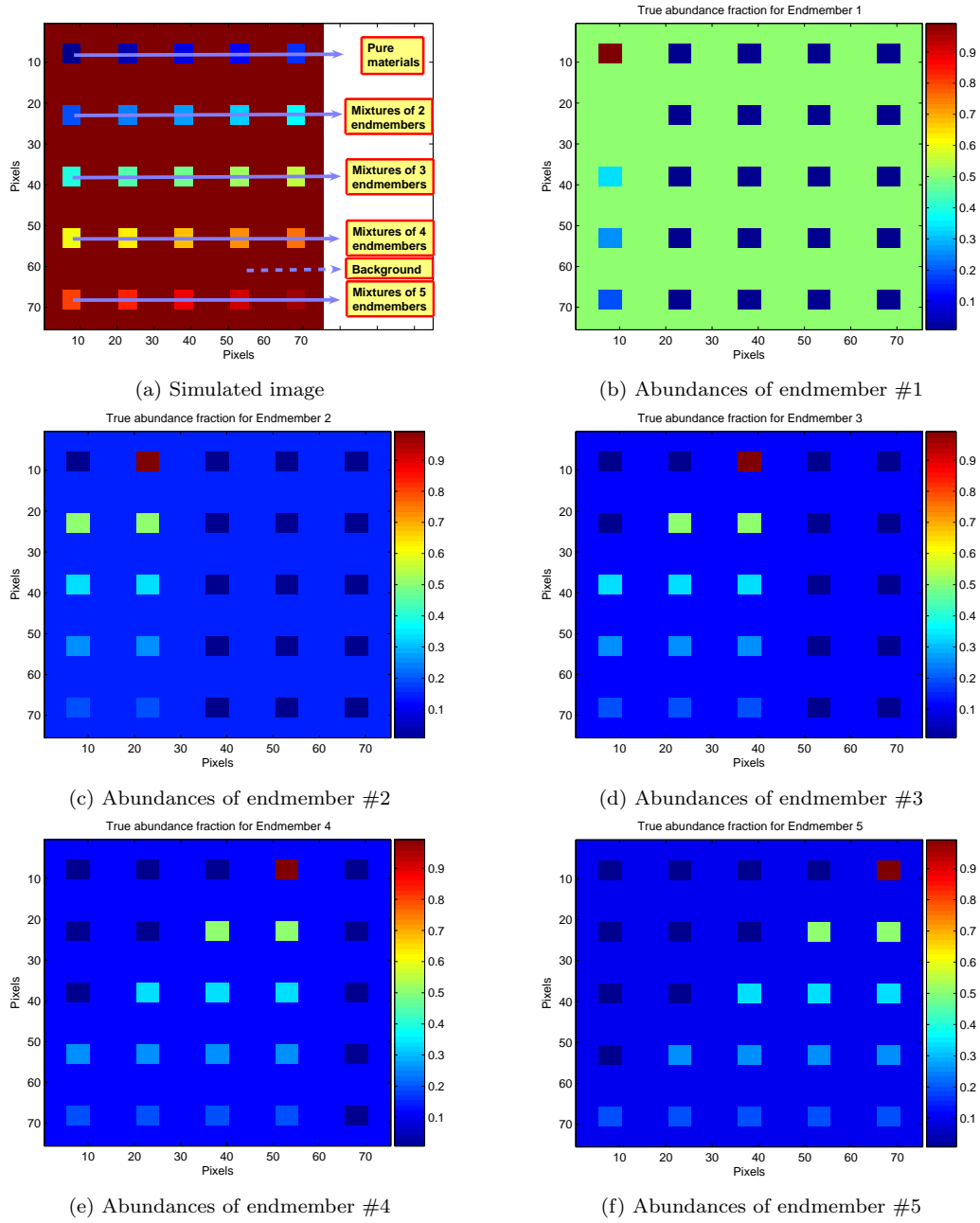


Figure 2.13: Simulated data set constructed to evaluate the possibility of applying sparse unmixing methods using image-derived endmembers.

estimated and true abundances were aligned and the SRE(dB) was computed. Table 2.2 shows the mean SRE(dB) achieved, both for different values of  $\lambda$  and for each different endmember. For illustrative purposes, Fig. 2.14 also graphically displays the abundance estimation results obtained for one specific endmember (the 5<sup>th</sup> one used in the simulations). From Table 2.2, it can be seen that sparse techniques can still be successfully applied using image-derived endmembers in case there is no spectral library available *a priori*. Even in the presence of significant noise, SUnSAL+ always performed better than NCLS, no matter the value of  $\lambda$  tested or the endmember considered. The results displayed in Fig. 2.14 are also in line with these observations. It is also worth noting that, in this experiment, we did not determine *a priori* the optimal parameter for  $\lambda$ .

Table 2.2: SRE(dB) values achieved after applying SUnSAL+ to image-derived endmembers from the simulated image in Fig. 2.13.

	Results for different values of $\lambda$				
	$\lambda = 10^{-1}$	$\lambda = 5 \times 10^{-2}$	$\lambda = 10^{-3}$	$\lambda = 5 \times 10^{-4}$	NCLS: $\lambda = 0$
Mean SRE (dB)	9.60	10.82	12.09	12.62	9.10
	Results for different endmembers				
	endmember #1	endmember #2	endmember #3	endmember #4	endmember #5
Mean SRE (dB)	22.82	1.33	10.91	13.75	5.42

## 2.4.8 Summary and Main Observations

In summary, our main observation from the experiments conducted in this section is that spectral libraries are indeed suitable for solving the sparse unmixing problem in our simulated analysis scenarios. Although the techniques which do not explicitly enforce the sparsity of the solution exhibit similar performances with regards to sparse techniques when the observations are affected by white noise, our experimental results demonstrated that, by enforcing the sparsity of the solution, unmixing results can significantly improve when the observations are affected by correlated noise, which is the most typical one in real hyperspectral imaging scenarios. It is also worth noting that, according to our experiments, the sparse techniques exhibit better performance when the number of endmembers is low (say, up to 5), which is a reasonable assumption in practice, but also for higher cardinalities when the noise is correlated. Finally, we also demonstrated that sparse unmixing methods can be applied using image-derived endmembers when

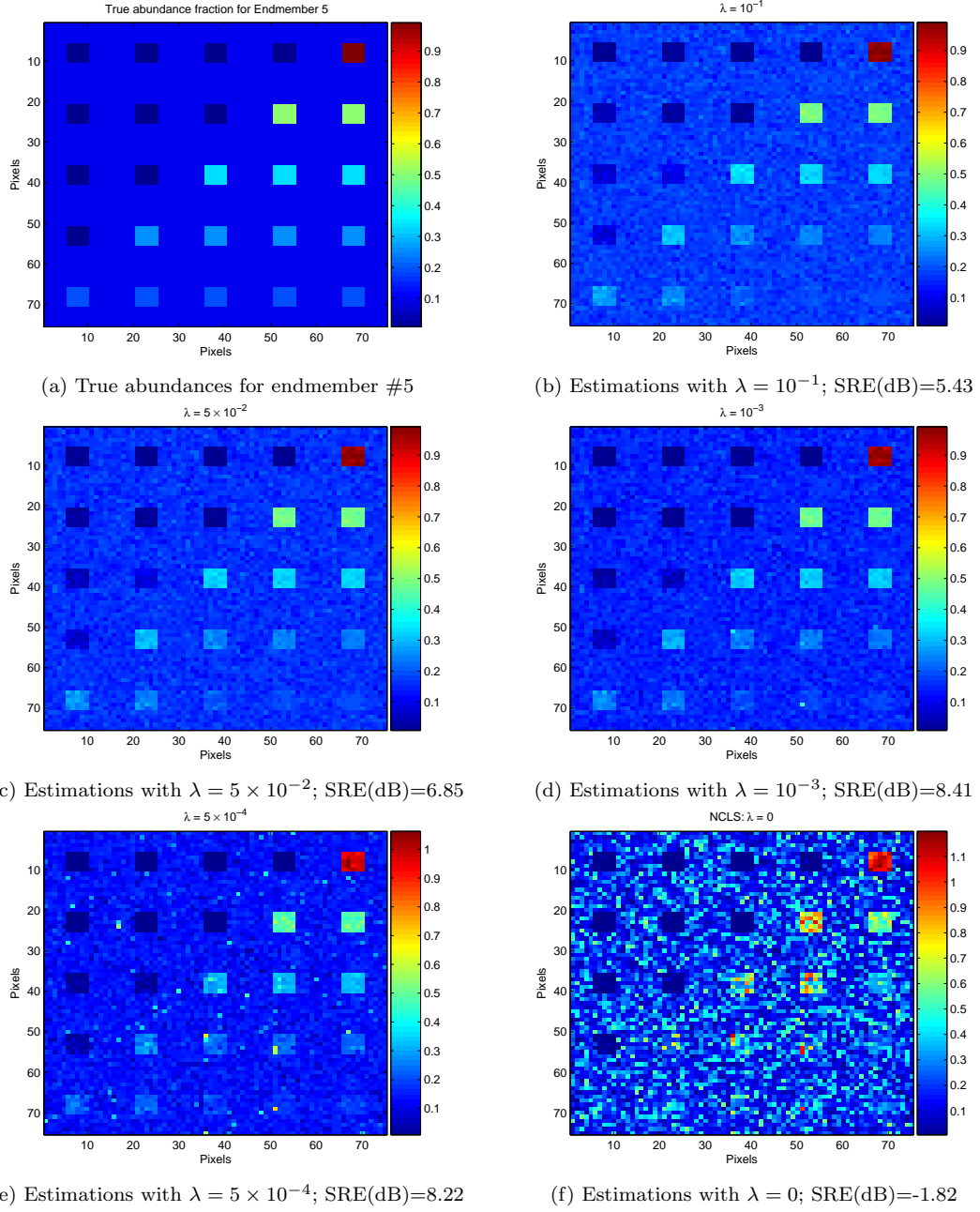


Figure 2.14: True and estimated abundance fractions for one of the simulated endmembers (all results were obtained using SUnSAL+ for different values of the parameter  $\lambda$ ).

there is no spectral library available *a priori*. Although our experiments with simulated mixtures are quite encouraging, the complexity of real mixtures is usually quite high and it is difficult to account for all possible issues affecting such mixtures when conducting simulations. For this reason, further experiments using real hyperspectral data sets are highly desirable. These will be conducted in the following section.

## 2.5 Experiments with Real Data

The scene used in our real data experiments is the well-known AVIRIS Cuprite data set, available online in reflectance units<sup>6</sup>. This scene has been widely used to validate the performance of endmember extraction algorithms. The portion used in experiments corresponds to a  $350 \times 350$ -pixel subset of the sector labeled as f970619t01p02\_r02\_sc03.a.rfi in the online data. The scene comprises 224 spectral bands between 0.4 and 2.5  $\mu\text{m}$ , with nominal spectral resolution of 10 nm. Prior to the analysis, bands 1–2, 105–115, 150–170, and 223–224 were removed due to water absorption and low SNR in those bands, leaving a total of 188 spectral bands. The Cuprite site is well understood mineralogically, and has several exposed minerals of interest, all included in the USGS library considered in experiments, denoted splib06<sup>7</sup> and released in September 2007. In our experiments, we use spectra obtained from this library as input to the unmixing methods described in section 2.3. For illustrative purposes, Fig. 2.15 shows a mineral map produced in 1995 by USGS, in which the Tricorder 3.3 software product [34] was used to map different minerals present in the Cuprite mining district<sup>8</sup>. It should be noted that the Tricorder map is only available for hyperspectral data collected in 1995, while the publicly available AVIRIS Cuprite data was collected in 1997. Therefore, a direct comparison between the 1995 USGS map and the 1997 AVIRIS data is not possible. However, the USGS map serves as a good indicator for qualitative assessment of the fractional abundance maps produced by the unmixing algorithms described in section 2.3.

---

<sup>6</sup><http://aviris.jpl.nasa.gov/html/aviris.freedata.html>

<sup>7</sup><http://speclab.cr.usgs.gov/spectral.lib06>

<sup>8</sup>[http://speclab.cr.usgs.gov/cuprite95.tgif.2.2um\\_map.gif](http://speclab.cr.usgs.gov/cuprite95.tgif.2.2um_map.gif)

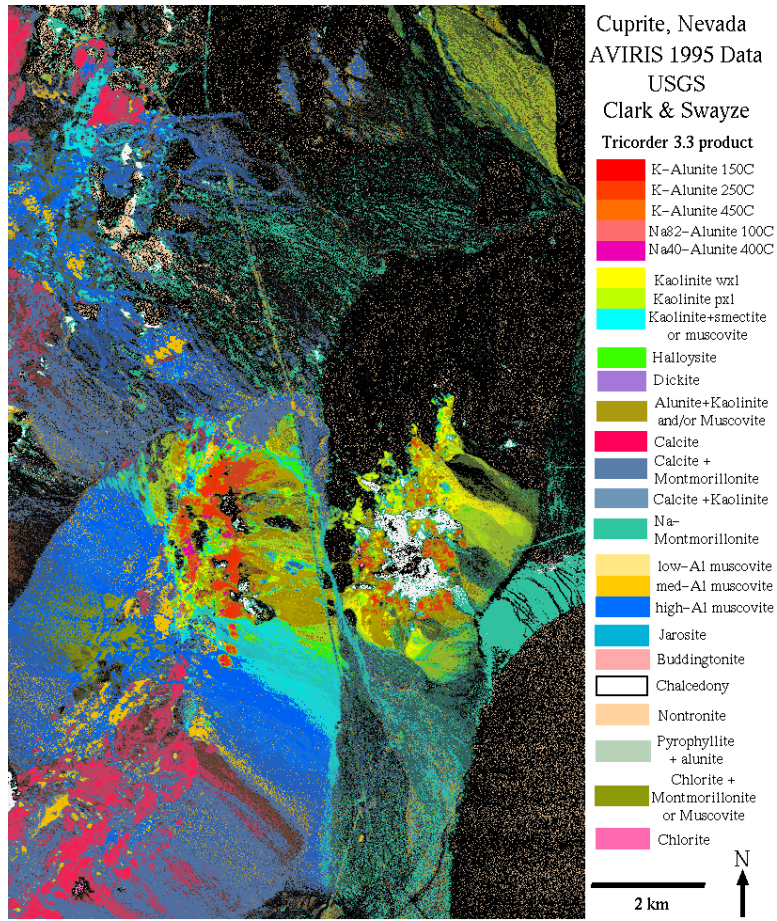


Figure 2.15: USGS map showing the location of different minerals in the Cuprite mining district in Nevada. The map is available online at: [http://speclab.cr.usgs.gov/cuprite95.tgif.2.2um\\_map.gif](http://speclab.cr.usgs.gov/cuprite95.tgif.2.2um_map.gif).

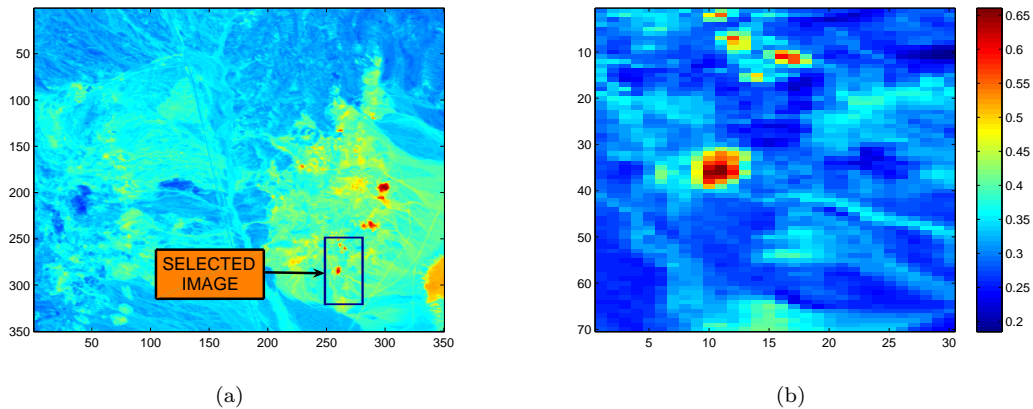


Figure 2.16: AVIRIS Cuprite hyperspectral scene used in our experiments. (a) Spatial localization of a toy  $70 \times 30$ -pixel subscene in the considered  $350 \times 350$ -pixel data set. (b) Spectral band at 558 nm wavelength of the toy subscene.

In order to compute approximate solutions and to compare the performances of the algorithms described in Section 2.3, a toy subscene of  $70 \times 30$  pixels of the Cuprite data set was first used prior to conducting experiments with the  $350 \times 350$ -pixel scene. The position of the toy subscene in the  $350 \times 350$  scene is shown in Fig. 2.16(a), while the spectral band at 558 nm wavelength of the toy subscene is shown in Fig. 2.16(b). The results obtained for the  $350 \times 350$ -pixel scene are presented at the end of this section.

In all our experiments with real data, we use library  $\mathbf{A}_1$  to compute approximate solutions. However, before processing the hyperspectral data, we should first focus our attention on calibration issues. As we have already referred to before, even though we are working with atmospherically corrected data in reflectance units, there are always calibration mismatches between the real pixel spectra and the spectra available in the library due to the rather different acquisition conditions of the two data types. In order to minimize these mismatches, we apply a band-dependent correction strategy to the original data set, which amounts at replacing the data set  $\mathbf{Y}$  with  $\mathbf{CY}$ , where  $\mathbf{C}$  is a diagonal matrix that minimizes the modeling error, i.e.:

$$\hat{\mathbf{C}} = \arg \min_{\mathbf{C}, \mathbf{X} \geq \mathbf{0}, \mathbf{1}_m^T \mathbf{X} = \mathbf{1}_n^T} \|\mathbf{A}_1 \mathbf{X} - \mathbf{CY}\|_2, \quad (2.27)$$

where  $\mathbf{X} \geq \mathbf{0}$  is the fractional abundance matrix. Problem (2.27) is non-convex and, thus, very hard to solve exactly. We have computed a sub-optimal solution to this problem by alternating the minimizing with respect to  $\mathbf{C}$  and to  $\mathbf{X}$ . We start the iterative procedure with  $\mathbf{C} = \mathbf{I}$ . The minimization with respect to  $\mathbf{C}$  and to  $\mathbf{X}$  are, respectively, least squares and constrained least squares problems. To speed up the process and ensure quality in the estimate of  $\mathbf{C}$ , we removed non-sparse fractional abundances from  $\mathbf{X}$  and the respective spectral vectors from  $\mathbf{Y}$  after the first iteration. We ran a total of 20 iterations. The plot of the correction factors with regards to the spectral bands is displayed in Fig. 2.17(a). These factors are always close to one, apart from a few bands in the blue wavelengths. For illustrative purposes, Fig. 2.17(b) shows a random pixel observation from the original AVIRIS Cuprite data set and its corrected version using the aforementioned strategy.

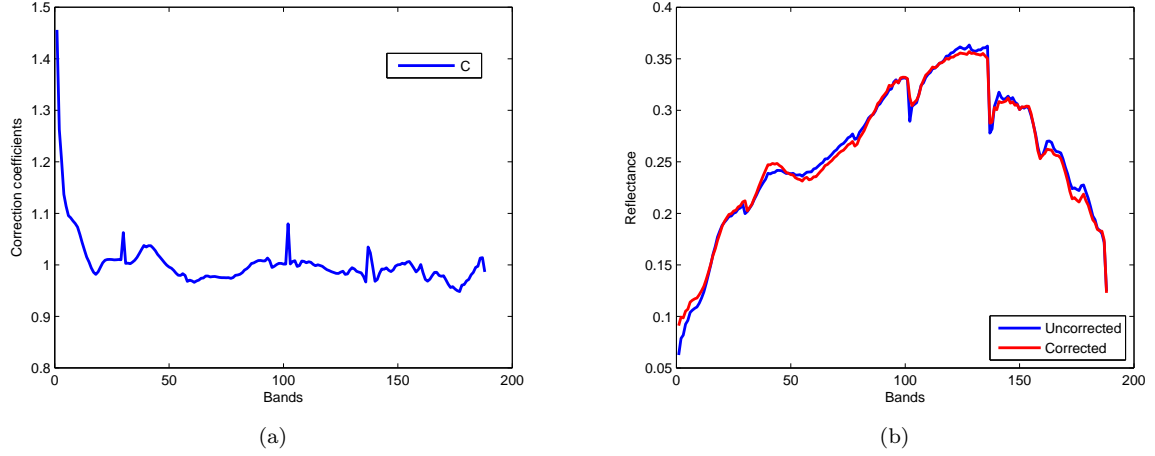


Figure 2.17: (a) Plot of diagonal values of the correction matrix  $\mathbf{C}$ . (b) Original (blue) and corrected (red) spectrum of a randomly selected pixel in the AVIRIS Cuprite data set.

After correcting the data, the unmixing problem was first solved for the toy subscene, using the sparse unmixing algorithms described in section 2.3. The parameters used were:  $\lambda = 10^{-5}$  for SUnSAL and all its variations, and  $\delta = 10^{-4}$  for CSUnSAL and all its variations. Fig. 2.18 represents the fractional abundance estimations obtained for each endmember material in the  $\mathbf{A}_1$  spectral library (as a function of the pixel index in the considered toy subscene) by the considered sparse unmixing methods. We emphasize that there are a total of  $70 \times 30 = 2100$  pixels in the toy subscene. As shown by Fig. 2.18, the unconstrained version of CSUnSAL leads to highly inaccurate (i.e. physically unrealistic) results since the solutions contain negative values. CSUnSAL+, on the other hand, introduces more reasonable abundance estimates which, in turn, do not comply with the ASC constraint since the sum of all abundance fractions per pixel generally exceed the value 1.0, i.e. these are super-unitary. CSUnSAL+D seems far more realistic than the unconstrained version. Both SUnSAL+D and CSUnSAL+D produce, in some cases, super-unitary fractional abundances. SUnSAL and SUnSAL+ exhibit similar performances, with the general observation that SUnSAL return vectors of fractional abundances which are more dense than SUnSAL+. Another general observation is that the constrained methods show clearly the sparsity of the solution, as the non-zero fractions appear in distinct lines (sometimes grouped in clusters). This is due to the fact that, in the library, there are consecutive members describing similar materials. This general observation is strengthened if we compute the average



number of endmembers having fractional abundances higher than 0.05 in one pixel: 44.05 for SUnSAL, 6.07 for SUnSAL+, 6.2 for SUnSAL+D, 68.55 for CSUnSAL, 8.36 for CSUnSAL+ and 11.09 for CSUnSAL+D. For illustrative purposes, Fig. 2.19 exemplifies the most significant minerals found by SUnSAL+ in the toy subscene.

It is important to note that the constrained results of sparse unmixing algorithms have very similar norms of the reconstruction error, with all of them situated for one randomly selected pixel around 0.05. We have used this observation in order to set the stopping threshold in the OMP and OMP+ algorithms to this value (i.e. by forcing them to achieve exactly the same error). In the case of ISMA we empirically set the algorithm threshold to  $t_3 = 2$ , based on the observed RMSE variation of a small number of randomly selected pixels (10). It is also worth noting that choosing a threshold for ISMA is extremely difficult in this application, since the RMSE has a very smooth variation and the critical iteration is very difficult to identify. For illustrative purposes, the unmixing results after using these three algorithms (OMP, OMP+ and ISMA) are reported in Fig. 2.21. From Fig. 2.21, it can be seen that OMP performs poorly (its solution contains many negative fractional abundances). OMP+ performs better and tolerates large super-unitary values, although the sparsity of the solution is quite apparent. The same observation is valid for ISMA. For the sake of completeness, Fig. 2.20 shows the fractional abundances estimated by NCLS in the toy subscene. The results were obtained using the SUnSAL algorithm, by setting  $\lambda = 0$  and activating the ANC constraint. Before reporting the abundance estimation results obtained for the  $350 \times 350$ -pixel data set, Table 2.3 reports the processing times (in seconds) measured after applying the considered unmixing algorithms to the toy  $70 \times 30$ -pixel subscene. The algorithms were implemented using MatlabR2009 on a desktop PC equipped with an Intel Core 2 Duo CPU (at 2.33 GHz) and 2GB of RAM memory. As shown by Table 2.3, ISMA is quite slow compared to the other algorithms, while OMP and OMP+ are the fastest ones. NCLS and SUnSAL in all its variants exhibit comparable running times, while CSUnSAL proves to be slower than them. In turn, SUnSAL is very fast in the unconstrained version. Although some of the reported sparse unmixing algorithms needed

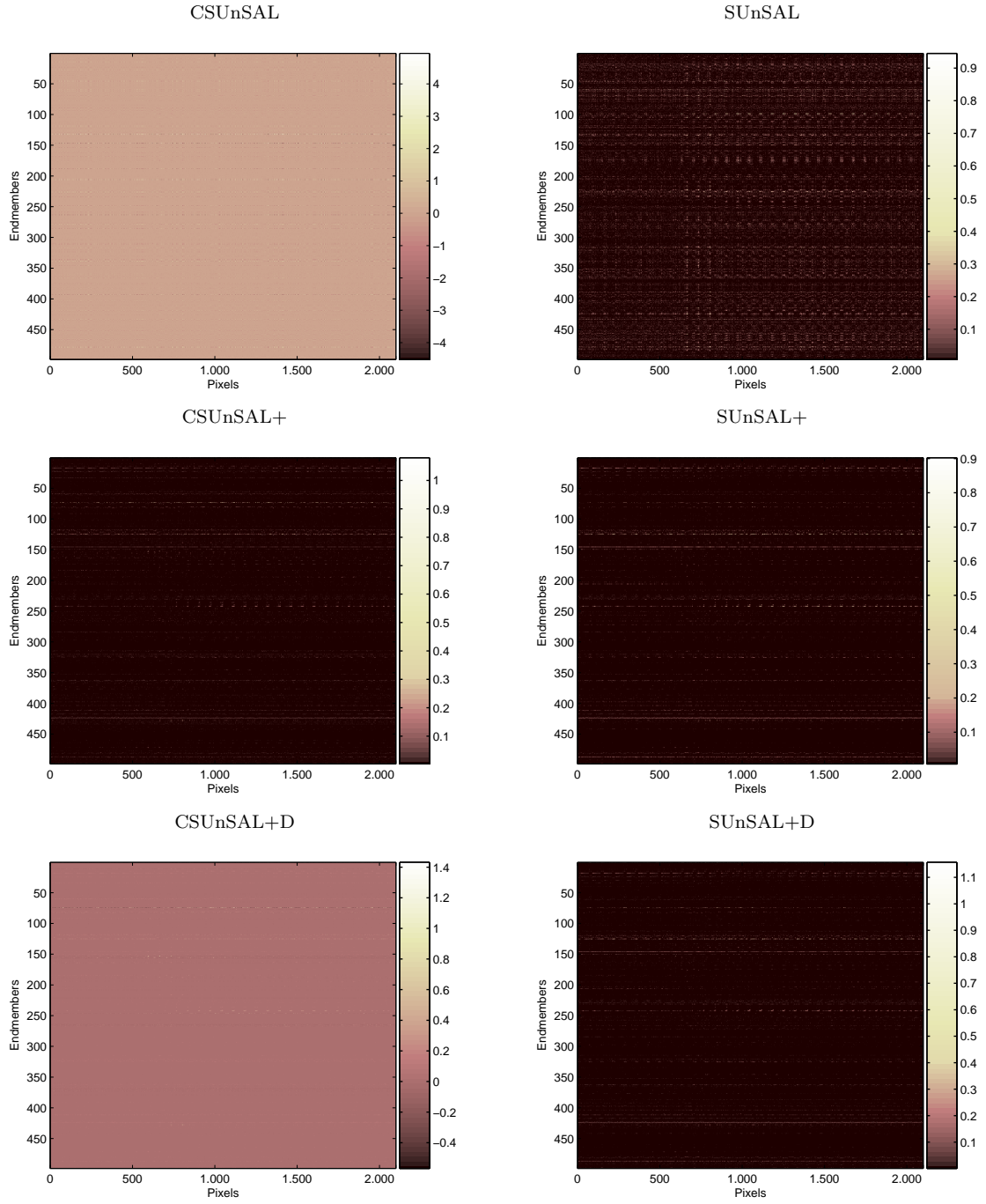


Figure 2.18: Fractional abundance estimations obtained for each endmember material in the  $\mathbf{A}_1$  spectral library (as a function of the pixel index in the considered toy subspace) by the considered sparse unmixing methods.

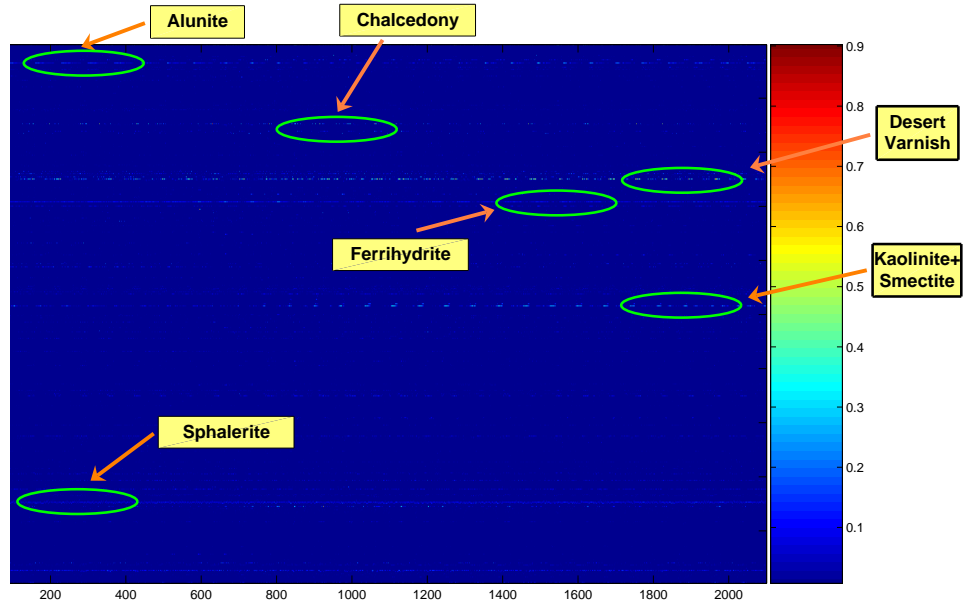


Figure 2.19: Fractional abundance estimations obtained for each endmember material in the  $\mathbf{A}_1$  spectral library (as a function of the pixel index in the considered toy subspace) by the SUnSAL+ method. The most significant minerals found by this algorithm are outlined.

significant times to complete their calculations in this example, their implementation in the form of parallel algorithms is very feasible and this strategy (not adopted in this work) can lead to significant reductions in processing time in future developments.

Table 2.3: Processing times (in seconds) measured after applying the considered unmixing algorithms to the toy  $70 \times 30$ -pixel subspace on a desktop PC equipped with an Intel Core 2 Duo CPU (at 2.33 GHz) and 2GB of RAM memory.

	OMP	OMP+	NCLS	ISMA	SUnSAL	SUnSAL+	SUnSAL+D	CSUnSAL	CSUnSAL+	CSUnSAL+D
Time [s]	71	76	413	50400	195	420	520	1011	1355	1402

Based on the previous results, which indicate that the ANC-constrained versions of SUnSAL and CSUnSAL exhibit similar performances in this problem and that sparse techniques generally exhibit better performance than those techniques that do not explicitly enforce sparseness, we now apply the SUnSAL+ algorithm to estimate fractional abundances in the  $350 \times 350$ -pixel AVIRIS Cuprite scene using the spectral library  $\mathbf{A}_1$  and a pruned version of  $\mathbf{A}_1$ . The pruned version was obtained by simply removing some of the spectral signatures which form a spectral angle smaller than  $2.5^\circ$ , thus obtaining a library with 390 spectrally distinct signatures denoted by  $\mathbf{A}$ . Fig. 2.22 shows a visual (qualitative) comparison between the fractional abundance

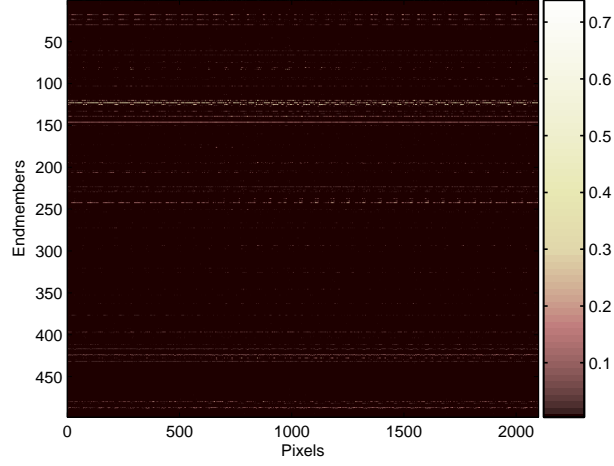
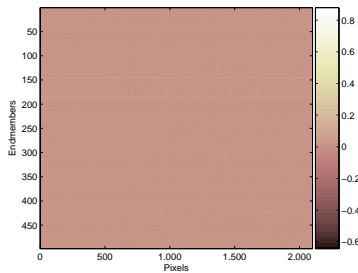
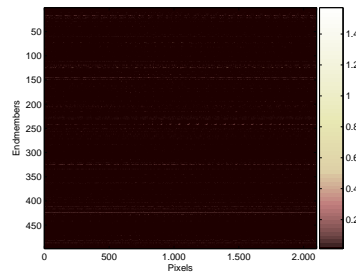


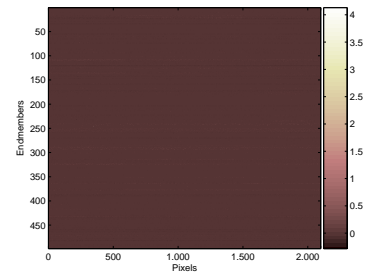
Figure 2.20: Fractional abundance estimations obtained for each endmember material in the  $\mathbf{A}_1$  spectral library (as a function of the pixel index in the considered toy subspace) by the NCLS method.



(a) OMP



(b) OMP+



(c) ISMA

Figure 2.21: Fractional abundance estimations obtained for each endmember material in the  $\mathbf{A}_1$  spectral library (as a function of the pixel index in the considered toy subspace) by the OMP, OMP+ and ISMA methods.

maps, estimated for 7 highly materials in the AVIRIS Cuprite scene, by applying the SUnSAL+ algorithm. For comparative purposes, the spatial distribution maps of these materials extracted from the Tricorder classification map shown in Fig. 2.15 are also displayed. From Fig. 2.22, it can be observed that the SUnSAL+ sparse unmixing technique is able to find a good approximation for the distribution of the materials in the scene, both for the original and also for the pruned version of the spectral library. It should be noted that there are still some differences between our estimated abundance maps and the Tricorder maps, mainly due to the fact that the Tricorder maps are in fact classification maps (i.e., all pixels are considered pure and classified as belonging or not to a class given by the representative mineral in that pixel) and not abundance maps (in which the value assigned to a mixed pixel varies depending on the degree of presence of the mineral in the pixel). Even so, it can be seen visually that the SUnSAL+ sparse unmixing technique generally returns the highest abundances exactly for those pixels classified as belonging to the respective class of materials.

## 2.6 Conclusions and Future Research

In this chapter, we have reformulated the spectral unmixing problem under the light of sparse regression, and further evaluated the performance of several (available and new) sparse regression algorithms in spectral unmixing applications. One significant advantage of using sparse regression for spectral unmixing purposes is to take advantage of the increasing availability of spectral libraries of materials measured on the ground, for instance, using advanced field spectroradiometers. Through the sparse unmixing techniques described in this chapter, mixed pixels can be expressed in the form of linear combinations of a number of pure spectral signatures known in advance and available in a library. With this strategy, the abundance estimation process no longer depends on the availability of pure spectral signatures in the input data nor on the capacity of a certain endmember extraction algorithm to identify such pure signatures. Quite opposite, the procedure is reduced to finding the optimal subset of signatures in the library that can best model each mixed pixel in the scene.

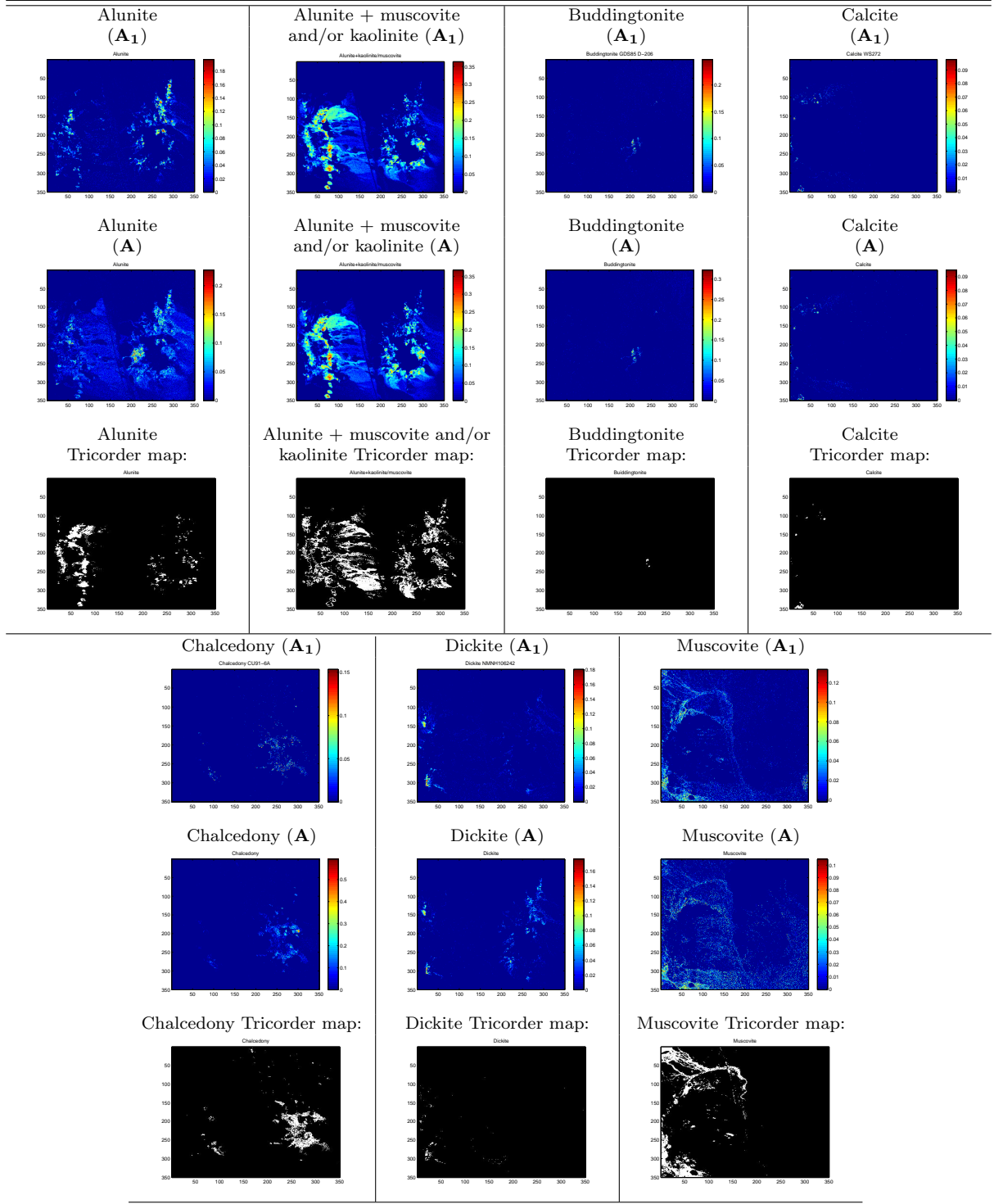


Figure 2.22: Qualitative comparison between the fractional abundance maps estimated by the SUNSAL+ sparse unmixing technique and the classification maps produced by USGS Tricorder algorithm for the  $350 \times 350$ -pixel AVIRIS Cuprite scene.

Although our experimental results (conducted with both simulated and real data sets) are very encouraging, there are several aspects to be considered in practice and worth being further investigated in future research efforts. One is the fact that the library spectra are rarely acquired under the same conditions as the airborne data. To address this issue, in this work we have adopted a simple correction algorithm to compensate for possible interferers. Another issue is the fact that the ability to obtain useful sparse solutions of an under-determined system of equations depends, mostly, on the degree of coherence between the columns of the system matrix and also on the degree of sparseness of the original signals. As a result, the most favorable scenarios correspond to highly sparse signals and system matrices with low coherence. Unfortunately, in hyperspectral imaging applications the spectral signatures of the materials tend to be highly correlated. This unfavorable aspect is, somehow, balanced by the highly sparse nature of the fractional abundances. A final issue to be explored in future developments is the high computational complexity of sparse unmixing algorithms, addressed in this work by the consideration of fast algorithms based on the augmented Lagrangian method of multipliers but also subject to further improvements related with the inherently parallel nature of such algorithms. In fact, an important advantage of sparse unmixing methods is that their complexity depends more on the cardinality of the solution and on the number of spectra in the library and less on the size of the hyperspectral image to be processed. Since sparse unmixing is conducted in pixel-by-pixel fashion, the procedure could be accelerated by dividing the image into sub-images (or sub-sets of pixels) of any size, and processing the sub-partitions in parallel without the need to establish an optimal size of sub-images or sub-partitions. This feature anticipates high scalability of potential parallel solutions to this approach.

## **Appendix –**

In this Appendix, we report the parameters used in our simulated data experiments. Specifically, Table 2.4 reports the parameters used when looking for approximate solutions in experiments with  $\text{SNR} = 30\text{dB}$ , for each considered cardinality, unmixing method and spectral library. In order to ensure a fair comparison, we defined near-optimal parameters for groups or

levels of sparsity, with each group being described by a representative level for all considered methods. The parameters were denoted as follows:  $t_1$ ,  $t_2$  and  $t_3$  are the thresholds imposed in the stopping criteria for OMP, OMP+ and ISMA;  $\lambda_1$ ,  $\lambda_2$ ,  $\lambda_3$  are the regularization parameters for SUnSAL, SUnSAL+ and SUnSAL+D; and  $\delta_1$ ,  $\delta_2$ ,  $\delta_3$  are the tolerance errors for CSUnSAL, CSUnSAL+ and CSUnSAL+D, respectively. It should be noted that NCLS does not require any input parameter.

In order to find near-optimal parameters in this particular case (SNR = 30dB), the representative levels for the groups of sparsity were chosen as follows: for  $k = 2 \dots 6$  the representative level is  $k_1 = 4$ ; for  $k = 7 \dots 13$  the representative level is  $k_2 = 10$ ; and for  $k = 14 \dots 20$  the representative level is  $k_3 = 17$ . Table 2.4 [columns (a) and (b)] show the near-optimal parameters established for the simulated data sets affected by white and correlated noise, respectively. These parameters are near-optimal for the representative cardinalities, but they are applied for all sparsity levels in the respective group and they were inferred by testing the algorithms using toy examples, i.e. by considering a large range of possible discrete values on the basis of a small number of samples (10).

On the other hand, Table 2.5 reports the parameters used in our simulated data experiments when the true cardinality was  $k = 5$  and the SNR varied between 20 and 50dB. These parameters were found in a similar fashion to the ones reported in Table 2.4, considering two representative levels of the SNR:  $k_1 = 25$ dB for SNR = 20...30dB, and  $k_2 = 45$ dB for  $k = 40 \dots 50$ dB. To conclude this section, we would like to emphasize our significant efforts in testing the most suitable parameters in order to report only near-optimal results for each considered method.



Table 2.4: Parameter settings used in our simulated data experiments when the SNR was constant (SNR = 30dB).

		(a) White noise			(b) Colored noise		
		$k_1 = 4$	$k_2 = 10$	$k_3 = 17$	$k_1 = 4$	$k_2 = 10$	$k_3 = 17$
OMP ( $t_1$ )	$\mathbf{A}_1$	0.31	0.29	0.23	0.045	0.02	0.005
	$\mathbf{A}_2$	0.035	0.03	0.03	0.005	0.005	0.005
	$\mathbf{A}_3$	0.245	0.255	0.33	0.065	0.02	0.225
	$\mathbf{A}_4$	0.105	0.02	0.02	0.315	0.005	0.01
	$\mathbf{A}_5$	0.365	0.21	0.16	0.4	0.28	0.155
	$\mathbf{A}_6$	0.29	0.25	0.24	0.275	0.225	0.07
OMP+ ( $t_2$ )	$\mathbf{A}_1$	0.05	0.145	0.026	0.06	0.03	0.015
	$\mathbf{A}_2$	0.21	0.02	0.02	0.005	0.005	0.005
	$\mathbf{A}_3$	0.02	0.085	0.245	0.275	0.155	0.165
	$\mathbf{A}_4$	0.025	0.01	0.02	0.3	0.2	0.15
	$\mathbf{A}_5$	-	-	-	-	-	-
	$\mathbf{A}_6$	0.285	0.25	0.23	0.24	0.14	0.065
ISMA ( $t_3$ )	$\mathbf{A}_1$	0.04	0.004	$7 \cdot 10^{-4}$	$5 \cdot 10^{-4}$	$5 \cdot 10^{-4}$	$10^{-6}$
	$\mathbf{A}_2$	$10^{-4}$	$4 \cdot 10^{-4}$	$10^{-4}$	$6 \cdot 10^{-4}$	0.001	$5 \cdot 10^{-6}$
	$\mathbf{A}_3$	0.003	$10^{-4}$	$5 \cdot 10^{-4}$	0.004	0.05	$6 \cdot 10^{-4}$
	$\mathbf{A}_4$	$7 \cdot 10^{-4}$	$7 \cdot 10^{-4}$	$3 \cdot 10^{-4}$	0.03	$2 \cdot 10^{-4}$	$10^{-5}$
	$\mathbf{A}_5$	0.03	0.001	$10^{-4}$	0.03	0.001	$10^{-4}$
	$\mathbf{A}_6$	0.02	0.004	0.005	0.05	$5 \cdot 10^{-4}$	0.004
SUNSAL ( $\lambda_1$ )	$\mathbf{A}_1$	0.006	0.004	0.003	$10^{-5}$	$10^{-5}$	$10^{-5}$
	$\mathbf{A}_2$	$3 \cdot 10^{-4}$	$3 \cdot 10^{-4}$	$6 \cdot 10^{-4}$	$10^{-5}$	$10^{-5}$	$10^{-5}$
	$\mathbf{A}_3$	0.4	0.5	0.5	0.008	0.003	0.001
	$\mathbf{A}_4$	0.002	0.003	0.004	$5 \cdot 10^{-5}$	$5 \cdot 10^{-5}$	$10^{-5}$
	$\mathbf{A}_5$	0.5	0.3	0.2	0.4	0.4	0.1
	$\mathbf{A}_6$	0.5	0.3	0.5	0.4	0.2	0.1
SUNSAL+ ( $\lambda_2$ )	$\mathbf{A}_1$	0.04	0.04	0.01	$10^{-5}$	$5 \cdot 10^{-5}$	$5 \cdot 10^{-5}$
	$\mathbf{A}_2$	0.005	$10^{-6}$	$10^{-5}$	$10^{-5}$	$10^{-6}$	$5 \cdot 10^{-7}$
	$\mathbf{A}_3$	0.5	0.3	0.4	$5 \cdot 10^{-4}$	$6 \cdot 10^{-4}$	$5 \cdot 10^{-4}$
	$\mathbf{A}_4$	$6 \cdot 10^{-5}$	$5 \cdot 10^{-6}$	$8 \cdot 10^{-5}$	$10^{-4}$	$10^{-5}$	$10^{-5}$
	$\mathbf{A}_5$	0.5	0.31	0.2	0.4	0.3	0.2
	$\mathbf{A}_6$	0.08	0.06	0.07	0.04	0.03	0.3
SUNSAL+D ( $\lambda_3$ )	$\mathbf{A}_1$	0.05	0.01	0.005	$7 \cdot 10^{-4}$	$3 \cdot 10^{-4}$	$7 \cdot 10^{-4}$
	$\mathbf{A}_2$	0.002	$5 \cdot 10^{-4}$	$10^{-5}$	$3 \cdot 10^{-6}$	$10^{-6}$	$5 \cdot 10^{-7}$
	$\mathbf{A}_3$	0.4	0.3	0.3	0.001	0.004	0.001
	$\mathbf{A}_4$	0.005	0.001	0.001	$10^{-6}$	$5 \cdot 10^{-6}$	$10^{-7}$
	$\mathbf{A}_5$	-	-	-	-	-	-
	$\mathbf{A}_6$	0.1	0.1	0.3	0.09	0.09	0.09
CSUNSAL ( $\delta_1$ )	$\mathbf{A}_1$	0.3	0.2	0.2	0.001	0.001	$5 \cdot 10^{-4}$
	$\mathbf{A}_2$	0.09	0.04	0.03	$10^{-5}$	$2 \cdot 10^{-4}$	$10^{-4}$
	$\mathbf{A}_3$	$10^{-7}$	$10^{-7}$	$10^{-12}$	0.03	0.02	0.009
	$\mathbf{A}_4$	0.03	0.03	0.03	$10^{-4}$	$10^{-5}$	$10^{-5}$
	$\mathbf{A}_5$	0.3	0.2	0.1	0.3	0.1	0.08
	$\mathbf{A}_6$	0.2	0.2	0.2	0.2	0.2	0.2
CSUNSAL+ ( $\delta_2$ )	$\mathbf{A}_1$	0.4	0.3	0.3	$10^{-5}$	$5 \cdot 10^{-5}$	$10^{-5}$
	$\mathbf{A}_2$	0.03	0.03	0.03	$10^{-4}$	$10^{-4}$	$5 \cdot 10^{-4}$
	$\mathbf{A}_3$	0.05	0.01	0.01	$10^{-12}$	$10^{-10}$	$10^{-12}$
	$\mathbf{A}_4$	0.03	0.03	0.02	$10^{-5}$	$5 \cdot 10^{-5}$	$5 \cdot 10^{-5}$
	$\mathbf{A}_5$	0.3	0.2	0.1	0.3	0.2	0.09
	$\mathbf{A}_6$	0.2	0.2	0.2	0.3	0.2	0.1
CSUNSAL+D ( $\delta_3$ )	$\mathbf{A}_1$	0.03	0.01	0.01	$10^{-4}$	$10^{-4}$	$10^{-4}$
	$\mathbf{A}_2$	$10^{-4}$	$10^{-5}$	$10^{-5}$	$10^{-4}$	$10^{-5}$	$10^{-5}$
	$\mathbf{A}_3$	0.002	0.002	0.001	$10^{-4}$	$10^{-4}$	$10^{-4}$
	$\mathbf{A}_4$	$10^{-5}$	$10^{-5}$	$10^{-7}$	$10^{-7}$	$10^{-7}$	$10^{-7}$
	$\mathbf{A}_5$	-	-	-	-	-	-
	$\mathbf{A}_6$	0.1	0.05	0.01	0.1	0.02	0.01

Table 2.5: Parameter settings used in our simulated data experiments when the SNR varied between 20 and 50dB.

		(a) White noise		(b) Colored noise	
		$k_1 = 25dB$	$k_2 = 45dB$	$k_1 = 25dB$	$k_2 = 45dB$
OMP ( $t_1$ )	$\mathbf{A}_1$	0.05	0.055	0.05	0.06
	$\mathbf{A}_2$	0.055	0.09	0.05	0.05
	$\mathbf{A}_3$	0.05	0.05	0.05	0.05
	$\mathbf{A}_4$	0.05	0.05	0.05	0.05
	$\mathbf{A}_5$	0.05	0.05	0.065	0.05
	$\mathbf{A}_6$	0.05	0.05	0.05	0.055
OMP+ ( $t_2$ )	$\mathbf{A}_1$	0.05	0.05	0.07	0.065
	$\mathbf{A}_2$	0.05	0.05	0.05	0.05
	$\mathbf{A}_3$	0.05	0.05	0.05	0.05
	$\mathbf{A}_4$	0.05	0.05	0.05	0.05
	$\mathbf{A}_5$	-	-	-	-
	$\mathbf{A}_6$	0.05	0.05	0.05	0.055
ISMA ( $t_3$ )	$\mathbf{A}_1$	$10^{-4}$	$8 \cdot 10^{-5}$	$8 \cdot 10^{-5}$	$5 \cdot 10^{-5}$
	$\mathbf{A}_2$	$5 \cdot 10^{-5}$	$5 \cdot 10^{-5}$	$10^{-4}$	$5 \cdot 10^{-5}$
	$\mathbf{A}_3$	$5 \cdot 10^{-5}$	$10^{-4}$	0.2	0.05
	$\mathbf{A}_4$	$5 \cdot 10^{-5}$	$5 \cdot 10^{-5}$	$8 \cdot 10^{-5}$	$8 \cdot 10^{-5}$
	$\mathbf{A}_5$	0.003	$3 \cdot 10^{-4}$	0.005	0.001
	$\mathbf{A}_6$	0.001	$5 \cdot 10^{-5}$	$5 \cdot 10^{-5}$	$10^{-4}$
SUnSAL ( $\lambda_1$ )	$\mathbf{A}_1$	0.05	0.001	$10^{-5}$	$10^{-5}$
	$\mathbf{A}_2$	0.005	$10^{-4}$	$10^{-5}$	$5 \cdot 10^{-5}$
	$\mathbf{A}_3$	0.2	0.2	0.001	$5 \cdot 10^{-5}$
	$\mathbf{A}_4$	$8 \cdot 10^{-4}$	$10^{-4}$	$10^{-5}$	$10^{-5}$
	$\mathbf{A}_5$	0.2	0.05	0.2	0.1
	$\mathbf{A}_6$	0.2	0.05	0.2	0.01
SUnSAL+ ( $\lambda_2$ )	$\mathbf{A}_1$	0.01	$10^{-4}$	0.01	$10^{-4}$
	$\mathbf{A}_2$	0.005	$10^{-4}$	$10^{-8}$	$5 \cdot 10^{-5}$
	$\mathbf{A}_3$	0.2	0.2	0.01	0.003
	$\mathbf{A}_4$	$10^{-4}$	$5 \cdot 10^{-5}$	$10^{-4}$	$10^{-5}$
	$\mathbf{A}_5$	0.2	0.1	0.2	0.1
	$\mathbf{A}_6$	0.2	0.05	0.05	0.01
SUnSAL+D ( $\lambda_2$ )	$\mathbf{A}_1$	0.2	0.001	0.05	0.05
	$\mathbf{A}_2$	$10^{-4}$	0.2	0.001	0.2
	$\mathbf{A}_3$	0.2	0.2	0.005	$5 \cdot 10^{-5}$
	$\mathbf{A}_4$	0.1	0.2	0.2	0.2
	$\mathbf{A}_5$	-	-	-	-
	$\mathbf{A}_6$	0.2	0.1	0.2	0.1
CSUnSAL ( $\delta_1$ )	$\mathbf{A}_1$	0.3	0.05	$8 \cdot 10^{-4}$	$10^{-4}$
	$\mathbf{A}_2$	0.05	0.005	$10^{-8}$	$10^{-8}$
	$\mathbf{A}_3$	0.3	0.3	0.01	0.001
	$\mathbf{A}_4$	0.05	0.005	$5 \cdot 10^{-5}$	$10^{-8}$
	$\mathbf{A}_5$	0.3	0.05	0.3	0.05
	$\mathbf{A}_6$	0.3	0.05	0.3	0.05
CSUnSAL+ ( $\delta_2$ )	$\mathbf{A}_1$	0.3	0.05	$8 \cdot 10^{-4}$	$10^{-8}$
	$\mathbf{A}_2$	0.05	0.005	0.003	$10^{-4}$
	$\mathbf{A}_3$	0.3	0.3	$10^{-8}$	$5 \cdot 10^{-5}$
	$\mathbf{A}_4$	0.05	0.003	$10^{-8}$	$10^{-5}$
	$\mathbf{A}_5$	0.3	0.05	0.3	0.05
	$\mathbf{A}_6$	0.3	0.05	0.3	0.05
CSUnSAL+D ( $\delta_3$ )	$\mathbf{A}_1$	0.3	0.05	0.1	0.05
	$\mathbf{A}_2$	0.3	0.3	0.3	0.3
	$\mathbf{A}_3$	0.3	0.3	$10^{-8}$	$10^{-4}$
	$\mathbf{A}_4$	0.3	0.3	0.3	0.3
	$\mathbf{A}_5$	-	-	-	-
	$\mathbf{A}_6$	0.3	0.3	0.3	0.3

## Chapter 3

# Total Variation Spatial Regularization for Sparse Hyperspectral Unmixing

**Abstract** – Spectral unmixing aims at estimating the fractional abundances of pure spectral signatures (also called *endmembers*) in each mixed pixel collected by a remote sensing hyperspectral imaging instrument. Mixed pixels are often encountered in hyperspectral scenes due to insufficient spatial resolution or mixing phenomena happening at different scales. In the previous chapter, the linear spectral unmixing problem was approached in semi-supervised fashion as a sparse regression one, under the assumption that the observed image signatures can be expressed as linear combinations of pure spectra, known *a priori* and available in a library. This new approach sidesteps well-known obstacles often met in endmember extraction, such as the stopping criteria for the extraction process (represented by the number of endmembers needed to explain the observed scene) and the fact that the scene might not contain pure pixels. It happens, however, that in many applications the spectral libraries contain highly correlated signatures, which limits the success of sparse regression applied to mixtures with a very small number of materials. Also, sparse unmixing focuses on analyzing the hyperspectral data without incorporating spatial information. As a result, sparse unmixing does not treat the hyperspectral data as *images*, but as unordered listings of spectral measurements with no particular spatial arrangement, disregarding the existing spatial correlation between image features. In this chapter, we mitigate these limitations by adding the total variation (TV) regularization to the classical sparse regression formulation, thus exploiting the spatial-contextual information present in the hyper-

spectral images. For this purpose, we explore the incorporation of spatial information on sparse unmixing techniques and further develop a new algorithm called *sparse unmixing via variable splitting augmented Lagrangian and total variation* (SUnSAL-TV). Our experimental results, conducted with both simulated data sets –generated using spectral libraries publicly available from the U.S. Geological Survey (USGS)– and real hyperspectral data sets, collected by NASA Jet Propulsion Laboratory’s Airborne Visible Infra-Red Imaging Spectrometer (AVIRIS), indicate the potential of including spatial information (through the TV term) on sparse unmixing formulations for improved characterization of mixed pixels in hyperspectral imagery.

**Index Terms** – Hyperspectral imaging, spectral unmixing, sparse unmixing, sparse regression, total variation (TV) regularization.

### 3.1 Introduction

Although the sparse unmixing techniques described in the previous chapter have been shown to exhibit good potential for the characterization of mixed pixels using spectral libraries, they focus mostly on exploiting the spectral information available in the hyperspectral data. Such information deals with pixel vectors in an independent manner from the neighboring pixel values, whereas spatial information concerns the relationship between each pixel vector and its neighbors. This means that, despite the inherent spatial-spectral duality that resides in hyperspectral scenes, the classic sparse unmixing approach uses only spectral information and disregards spatial-contextual information. Previous works showed that including spatial information, both as a preprocessing step [101] and in the unmixing procedure itself [76, 81], has a positive impact on the accuracy of the estimated fractional abundances. On the other hand, the success of unmixing when performed via sparse regression techniques relies on the *mutual coherence* [18] of the spectral library<sup>1</sup> and the number of materials in the mixtures, i.e., the so-called *degree of sparsity* [58]. In favorable scenarios, we have low degree of sparsity and low coherence. In hyperspectral applications, the former is often true, but the latter is not as shown

---

<sup>1</sup>The mutual coherence of a library is closely related with the so-called restricted isometric property (RIP) [20].

in the previous chapter.

In order to sidestep the limitations imposed to sparse regression by the high correlation of spectral libraries, in this chapter we develop a new algorithm called *sparse unmixing via variable splitting augmented Lagrangian and total variation* (SUnSAL-TV). This method includes spatial information on the sparse unmixing formulation by means of the total variation (TV) regularizer [82], [53], [21]. This regularizer accounts for spatial homogeneity: it is very likely that two neighboring pixels have similar fractional abundances for the same endmember. The TV regularizer acts as *a priori* information, which improves the conditioning of the underlying inverse problem [3]. At the end, unmixing is obtained by solving a large non-smooth convex optimization problem. It should be noted that the work [102] introduces a hyperspectral unmixing approach formally similar to ours. There is, however, a major conceptual difference: whereas we are solving a sparse regression problem based on a library, in [102] the endmembers are jointly inferred with the fractional abundances. Recall that the main rationale for our approach is avoiding the endmember estimation step. A vector TV was also used in [53] to unmix and increase the resolution of hyperspectral images. Again, there is a major conceptual difference with respect to our approach: whereas we are solving a sparse regression problem based on a library, the endmembers in [53] are inferred using an external algorithm, in this case the N-FINDR [95].

The remainder of the chapter is structured as follows. Section 3.2 reviews shortly the linear versus the sparse unmixing formulations. Section 3.3 describes the newly developed SUnSAL-TV algorithm. Section 3.4 describes our experimental results with simulated hyperspectral data sets. Section 3.5 describes experiments with real hyperspectral data. Section 3.6 concludes with some remarks and hints at plausible future research lines.

## 3.2 Linear versus sparse unmixing

The linear mixture model assumes that the spectral response of a pixel is a linear combination of all the pure spectral signatures (endmembers) present in the pixel. We recall the fact that, if we assume that the hyperspectral sensor used for data acquisition has  $L$  spectral bands, the

LMM can be rewritten in compact form as:

$$\mathbf{y} = \mathbf{M}\boldsymbol{\alpha} + \mathbf{n}, \quad (3.1)$$

where  $\mathbf{y}$  is an  $L \times 1$  column vector (the measured spectrum of the pixel),  $\mathbf{M}$  is an  $L \times q$  matrix containing  $q$  endmembers,  $\boldsymbol{\alpha}$  is a  $q \times 1$  vector containing the fractional abundances of the endmembers in the pixel, and  $\mathbf{n}$  is an  $L \times 1$  vector collecting the errors affecting the measurements at each spectral band. As mentioned in the previous chapter, two constraints related to fractional abundance estimation (ANC and ASC) are widely used in the literature. These constraints are described in Eqs. (2.3) and (2.4).

Sparse unmixing reformulates (3.1) assuming the availability of a library of spectral signatures *a priori* as follows:

$$\mathbf{y} = \mathbf{A}\mathbf{x} + \mathbf{n}, \quad (3.2)$$

where  $\mathbf{x}$  is the fractional abundance vector compatible with library  $\mathbf{A} \in \mathbb{R}^{L \times m}$ . Due to the fact that only a few of the signatures contained in  $\mathbf{A}$  are likely contributing to the observed spectrum,  $\mathbf{x}$  contains many values of zero, which means that it is *sparse*. We recall now the two formulations of the sparse unmixing problem described in the previous chapter:

$$\min_{\mathbf{x}} \frac{1}{2} \|\mathbf{A}\mathbf{x} - \mathbf{y}\|_2^2 + \lambda \|\mathbf{x}\|_1 \quad \text{subject to} \quad \mathbf{x} \geq \mathbf{0}, \quad (3.3)$$

and:

$$(P_1^{\delta+}) : \min_{\mathbf{x}} \|\mathbf{x}\|_1 \quad \text{subject to} \quad \|\mathbf{A}\mathbf{x} - \mathbf{y}\|_2 \leq \delta, \quad \mathbf{x} \geq \mathbf{0}, \quad (3.4)$$

where  $\lambda$  is a regularization parameter and  $\delta$  is the tolerated reconstruction error. The optimization problems in (3.3) and (3.4) are convex and equivalent. This means that, for any given parameter  $\lambda$ , a corresponding parameter  $\delta$  can be found which leads to the same unmixing solution. In the following section we describe a new algorithm called SUnSAL-TV which efficiently

solves the sparse unmixing problem taking into account the relationship between each pixel vector and its neighbors, including the TV regularizer [82], [53], [21] on top of the aforementioned sparse unmixing formulation.

### 3.3 Total Variation for Sparse Unmixing – The SUnSAL-TV

#### Algorithm

Let  $\mathbf{Y} \in \mathbb{R}^{L \times n}$  be the observed data matrix (where each column contains the observed spectrum of a given pixel); let  $\mathbf{X} \in \mathbb{R}^{m \times n}$  be the fractional abundances matrix; let  $\|\mathbf{X}\|_F \equiv \sqrt{\text{trace}\{\mathbf{X}\mathbf{X}^T\}}$  be the Frobenius norm of  $\mathbf{X}$ ; let  $\|\mathbf{X}\|_{1,1} \equiv \sum_{i=1}^n \|\mathbf{x}_i\|_1$  ( $\mathbf{x}_i$  denotes the  $i^{\text{th}}$  column of  $\mathbf{X}$ ); and let  $\lambda \geq 0$  and  $\lambda_{TV} \geq 0$  be regularization parameters. With these definitions in place, we can now carry out the sparse unmixing by solving the following optimization problem:

$$\min_{\mathbf{X}} \frac{1}{2} \|\mathbf{A}\mathbf{X} - \mathbf{Y}\|_F^2 + \lambda \|\mathbf{X}\|_{1,1} + \lambda_{TV} \text{TV}(\mathbf{X}), \quad (3.5)$$

subject to  $\mathbf{X} \geq 0$ ,

where

$$\text{TV}(\mathbf{X}) \equiv \sum_{\{i,j\} \in \varepsilon} \|\mathbf{x}_i - \mathbf{x}_j\|_1 \quad (3.6)$$

is a vector extension of the non-isotropic TV [82], [21], which promotes piecewise constant (or smooth) transitions in the fractional abundance of the same endmember among neighboring pixels, and  $\varepsilon$  denotes the set of horizontal and vertical neighbors in the image. It should be noted that an isotropic TV can also be defined as follows:

$$\text{TV}_{iso}(\mathbf{X}) \equiv \sum_i \|(\mathbf{x}_i - \mathbf{x}_{h_i}), (\mathbf{x}_i - \mathbf{x}_{v_i})\|_1, \quad (3.7)$$

where  $\mathbf{x}_{h_i}$  and  $\mathbf{x}_{v_i}$  represent, respectively, the components of  $\mathbf{X}$  attached to the horizontal and vertical neighbors of the  $i^{\text{th}}$  pixel in the image. In both cases (isotropic and non-isotropic TV),

we consider cycling boundaries.

The minimization in (3.5) with  $\lambda_{TV}$  set to zero is a constrained basis pursuit denoising (CBPDN) problem [32] applied to each individual pixel. The application of CBPDN and several other constrained sparse regression algorithms to hyperspectral unmixing was extensively studied in the previous chapter.

It should be noted that the optimization problem in (3.5), although convex, is very hard to solve owing to non-smooth terms and its huge dimensionality. For instance, if we consider a  $256 \times 256$ -pixel image and a spectral library with 500 materials, then  $\mathbf{X} \in \mathbb{R}^{500 \times 256^2}$ , which is about 40 million variables! To solve the problem in (3.5), we have modified the SUnSAL algorithm [10] following closely the methodology introduced in [3]. The core idea is to introduce a set of new variables per regularizer and then use the ADMM method [44] to solve the resulting constrained optimization problem. By a careful choice of the new variables, the initial problem is converted into a sequence of much simpler problems. The resulting approach, called SUnSAL-TV, combines the idea of sparse unmixing with that of exploiting the spatial-contextual information present in the hyperspectral images by including the TV regularizer on top of the sparse unmixing formulation. Next, we formalize the SUnSAL-TV algorithm (more details are given in an appendix at the end of the chapter).

An equivalent way of writing the optimization problem (3.5) is:

$$\min_{\mathbf{X}} \frac{1}{2} \|\mathbf{AX} - \mathbf{Y}\|_F^2 + \lambda \|\mathbf{X}\|_{1,1} + \lambda_{TV} \|\mathbf{HX}\|_{1,1} + \iota_{R+}(\mathbf{X}), \quad (3.8)$$

where  $\mathbf{H} \equiv [\mathbf{H}_h^T \mathbf{H}_v^T]^T$  is a linear operator computing the horizontal and vertical differences between the components of  $\mathbf{X}$  corresponding to neighboring pixels and  $\iota_{R+}(\mathbf{X}) = \sum_{i=1}^n \iota_{R+}(\mathbf{x}_i)$  is the indicator function ( $\mathbf{x}_i$  represents the  $i^{th}$  column of  $\mathbf{X}$  and  $\iota_{R+}(\mathbf{x}_i)$  is zero if  $\mathbf{x}_i$  belongs to the nonnegative orthant and  $+\infty$  otherwise).

Given the objective function (3.8), we write the following (constrained) equivalent formula-



tion:

$$\min_{\mathbf{U}, \mathbf{V}_1, \mathbf{V}_2, \mathbf{V}_3, \mathbf{V}_4, \mathbf{V}_5} \frac{1}{2} \|\mathbf{V}_1 - \mathbf{Y}\|_F^2 + \lambda \|\mathbf{V}_2\|_{1,1} + \lambda_{TV} \|\mathbf{V}_4\|_{1,1} + \iota_{R+}(\mathbf{V}_5), \quad (3.9)$$

$$\text{subject to } \mathbf{V}_1 = \mathbf{A}\mathbf{U}$$

$$\mathbf{V}_2 = \mathbf{U}$$

$$\mathbf{V}_3 = \mathbf{U}$$

$$\mathbf{V}_4 = \mathbf{H}\mathbf{V}_3$$

$$\mathbf{V}_5 = \mathbf{U}.$$

In (3.9), notice the asymmetry of the constraint  $\mathbf{H}\mathbf{V}_3 = \mathbf{V}_4$ , compared with the remaining constraints. As seen below, this asymmetry underlies large computational gains by decoupling the optimization in the spatial domain from the optimization in the spectral domain. Optimization (3.9) can be written in a compact form as follows:

$$\min_{\mathbf{U}, \mathbf{V}} g(\mathbf{V}) \quad \text{subject to } \mathbf{G}\mathbf{U} + \mathbf{B}\mathbf{V} = \mathbf{0}, \quad (3.10)$$

where

$$\mathbf{V} \equiv (\mathbf{V}_1, \mathbf{V}_2, \mathbf{V}_3, \mathbf{V}_4, \mathbf{V}_5),$$

$$g(\mathbf{V}) \equiv \frac{1}{2} \|\mathbf{V}_1 - \mathbf{Y}\|_F^2 + \lambda \|\mathbf{V}_2\|_{1,1} + \lambda_{TV} \|\mathbf{V}_4\|_{1,1} + \iota_{R+}(\mathbf{V}_5),$$

and

$$\mathbf{G} = \begin{bmatrix} \mathbf{A} \\ \mathbf{I} \\ \mathbf{I} \\ \mathbf{0} \\ \mathbf{I} \end{bmatrix}, \quad \mathbf{B} = \begin{bmatrix} -\mathbf{I} & \mathbf{0} & \mathbf{0} & \mathbf{0} & \mathbf{0} \\ \mathbf{0} & -\mathbf{I} & \mathbf{0} & \mathbf{0} & \mathbf{0} \\ \mathbf{0} & \mathbf{0} & -\mathbf{I} & \mathbf{0} & \mathbf{0} \\ \mathbf{0} & \mathbf{0} & \mathbf{H} & -\mathbf{I} & \mathbf{0} \\ \mathbf{0} & \mathbf{0} & \mathbf{0} & \mathbf{0} & -\mathbf{I} \end{bmatrix}. \quad (3.11)$$

The ADMM algorithm for the formulation (3.10) is shown in Algorithm 3.1, where (see [3],

---

**Algorithm 3.1** Alternating direction method of multipliers (ADMM) pseudocode for solving problem (3.10).

---

1. **Initialization:** set  $k = 0$ , choose  $\mu > 0$ ,  $\mathbf{U}^{(0)}$ ,  $\mathbf{V}^{(0)}$ ,  $\mathbf{D}^{(0)}$
  2. **repeat:**
    3.  $\mathbf{U}^{(k+1)} \leftarrow \arg \min_{\mathbf{U}} \mathcal{L}(\mathbf{U}, \mathbf{V}^{(k)}, \mathbf{D}^{(k)})$
    4.  $\mathbf{V}^{(k+1)} \leftarrow \arg \min_{\mathbf{V}} \mathcal{L}(\mathbf{U}^{(k+1)}, \mathbf{V}, \mathbf{D}^{(k)})$
    5.  $\mathbf{D}^{(k+1)} \leftarrow \mathbf{D}^{(k)} - \mathbf{G}\mathbf{U}^{(k+1)} - \mathbf{B}\mathbf{V}^{(k+1)}$
  6. **until** some stopping criterion is satisfied.
- 

[45]):

$$\mathcal{L}(\mathbf{U}, \mathbf{V}, \mathbf{D}) \equiv g(\mathbf{U}, \mathbf{V}) + \frac{\mu}{2} \|\mathbf{G}\mathbf{U} + \mathbf{B}\mathbf{V} - \mathbf{D}\|_F^2, \quad (3.12)$$

is the augmented Lagrangian for problem (3.10),  $\mu > 0$  is a positive constant, and  $\mathbf{D}/\mu$  denotes the Lagrange multipliers associated to the constraint  $\mathbf{G}\mathbf{U} + \mathbf{B}\mathbf{V} = \mathbf{0}$ . In each iteration, Algorithm 3.1 sequentially optimizes  $\mathcal{L}$  with respect to  $\mathbf{U}$  (step 3) and  $\mathbf{V}$  (step 4), and then updates the Lagrange multipliers (step 5).

Matrix  $\mathbf{G}$  is full column rank and function  $g$  introduced in (3.10) is closed, proper, and convex. Then [44, Theorem 1] ensures that, for any  $\mu > 0$ , if (3.10) has a solution, say  $\mathbf{U}^*$ , then the sequence  $\{\mathbf{U}^{(k)}\}$ , converges to  $\mathbf{U}^*$ . If (3.10) does not have a solution, then at least one of the sequences  $\{\mathbf{U}^{(k)}\}$  or  $\{\mathbf{D}^{(k)}\}$  diverges. As stopping criterion, we use  $\|\mathbf{G}\mathbf{U}^{(k)} + \mathbf{B}\mathbf{V}^{(k)}\|_F \leq \varepsilon$ . The convergence speed of the ADMM algorithm depends on a suitable choice of parameter  $\mu$ . This is an active research topic and, to date, there is no explicit rule to select  $\mu$ . In this work it was hand-tuned for optimal performance.

We present in the appendix the details of the optimizations with respect to  $\mathbf{U}$  and  $\mathbf{V}$  of the ADMM Algorithm 3.1, which we term SUnSAL-TV. Here we make, however, a few pertinent observations. The optimization  $\mathbf{U}$  amounts at solving a linear system of equations of size  $m \times m$ . The matrix involved in this system of equations is fixed and then can be pre-computed involving low complexity as the rank of  $\mathbf{A}$  is  $\min\{L, m\}$ . The optimization with respect to  $\mathbf{V}$  is decoupled with respect to  $\mathbf{V}_1$ ,  $\mathbf{V}_2$ ,  $(\mathbf{V}_3, \mathbf{V}_4)$ , and  $\mathbf{V}_5$ . The reason for the coupling between  $\mathbf{V}_3$  and  $\mathbf{V}_4$  is the asymmetry already referred to in variable splitting introduced in (3.9). If we had followed

[3] exactly, we would have  $\mathbf{H}\mathbf{U} = \mathbf{V}_3$  instead of the couple  $\mathbf{U} = \mathbf{V}_3$  and  $\mathbf{H}\mathbf{V}_3 = \mathbf{V}_4$ . However, in this case, the optimization with respect to  $\mathbf{U}$  would be unbearable, as we would have matrix  $\mathbf{A}$  acting over the spectral dimension and matrix  $\mathbf{H}$  acting over the spatial domain in the same system.

As shown in the appendix, the optimizations with respect to  $\mathbf{V}_3$  alone and to  $\mathbf{V}_4$  alone are very light (the same is true for  $\mathbf{V}_1$ ,  $\mathbf{V}_2$ , and  $\mathbf{V}_5$ ). Therefore, a very simple way to achieve joint optimization with respect to  $(\mathbf{V}_3, \mathbf{V}_4)$  is to cycle over these two optimizations until convergence. In our SUnSAL-TV algorithm we cycle only once. We have two reasons for this decision: i) there is no need for an exact solution of optimizations with respect to  $\mathbf{U}$  (step 3) and  $\mathbf{V}$  (step 4) [44, Theorem 1], as long as the errors are summed; and ii) we have observed systematically faster convergence with just one step than with more steps. A proof of the convergence of SUnSAL-TV with just one step is, however, beyond the scope of this work.

Concerning computational complexity, we show in the appendix that each iteration of SUnSAL-TV has complexity  $\mathcal{O}(L^2n) + \mathcal{O}(Ln \log n)$ . Given that  $L$  is usually larger than  $n \log n$ , the first term dominates the total complexity of the algorithm.

Before concluding this section it is important to emphasize that, in this work, we test the SUnSAL-TV formulation using an exhaustive range of values for parameters  $\lambda$  and  $\lambda_{TV}$ , including zero. Hereinafter, we term the problem in (3.5) with  $\lambda = 0$  as *nonnegative constrained least squares TV* (NCLS-TV) and only *nonnegative constrained least squares* (NCLS) when  $\lambda = \lambda_{TV} = 0$ . In the following sections, we provide experimental results using both simulated and real hyperspectral data sets to illustrate the potential advantages of including TV regularization on top of sparse unmixing formulations, including both SUnSAL and NCLS.

### 3.4 Experiments with simulated data

In this section, we illustrate the unmixing performance achieved by including the TV regularizer on top of sparse regression formulations for spectral unmixing using two simulated hyperspectral datasets. The goal is to analyze the influence of the TV regularizer in the unmixing results,

both for solutions which are explicitly constrained to be sparse, and also for the ones computed without enforcing the sparseness explicitly. The section is organized as follows. Subsection 3.4.1 describes how the simulated data sets have been generated. We consider only scenes affected by noise, as the noiseless case is trivial. Subsection 3.4.2 concludes with a summary of the most relevant aspects observed in our simulated data experiments. This subsection contains also an additional comparison between the two types of TV regularizers discussed in this work (isotropic versus non-isotropic).

The performance discriminators adopted in this chapter are the ones described in Section 2.4.2 of Chapter 2: the signal to reconstruction error:  $\text{SRE} \equiv E[\|\mathbf{x}\|_2^2]/E[\|\mathbf{x} - \hat{\mathbf{x}}\|_2^2]$ , measured in dB:  $\text{SRE}(\text{dB}) \equiv 10 \log_{10}(\text{SRE})$ , and the probability of success:  $p_s \equiv P(\|\hat{x} - x\|^2/\|x\|^2 \leq \text{threshold})$ . Again, the estimation result is considered successful when  $\|\hat{x} - x\|^2/\|x\|^2 \leq 3.16$  (5dB). In all the tests using the TV regularizer on top of sparse unmixing approaches (SUnSAL-TV and NCLS-TV), we considered a first-order pixel neighborhood system.

### 3.4.1 Simulated data sets

We have considered two spectral libraries in our simulated image experiments:  $\mathbf{A}_1 \in \mathbb{R}^{224 \times 240}$  and  $\mathbf{A}_2 \in \mathbb{R}^{224 \times 240}$ . The libraries contain two different random selections of 240 materials (different mineral types) from the USGS library denoted splib06<sup>2</sup> and released in September 2007. The libraries comprise spectral signatures with reflectance values given in 224 spectral bands, distributed uniformly in the interval 0.4–2.5  $\mu\text{m}$ . The mutual coherences [18] are very close to 1. These libraries were used to generate two different simulated hyperspectral data cubes:

#### Simulated data cube 1 (DC1)

This simulated data cube was generated following closely the methodology described in Section 2.4.7, using five randomly selected spectral signatures from  $\mathbf{A}_1$ . This time, the background pixels have the following endmember abundances: 0.1149, 0.0741, 0.2003, 0.2055 and 0.4051,

---

<sup>2</sup>Available online: <http://speclab.cr.usgs.gov/spectral.lib06>

respectively. In the resulting simulated image, illustrated in Fig. 3.1(a), there are pure regions as well as mixed regions constructed using mixtures ranging between two and five endmembers, distributed spatially in the form of distinct square regions. Figs. 3.1(b)–(f) respectively show the true fractional abundances for each of the five endmembers. As in Section 2.4.7, after generating DC1 following the procedure described above, it was contaminated with i.i.d. Gaussian noise, for three levels of the signal-to-noise ratio ( $\text{SNR} \equiv \mathbb{E} \|\mathbf{Ax}\|^2 / \mathbb{E} \|\mathbf{n}\|_2^2$ ), i.e., 20dB, 30dB and 40dB.

### **Simulated data cube 2 (DC2)**

This simulated data cube was generated using nine randomly selected signatures from  $\mathbf{A}_2$ . The simulated image is made up of  $100 \times 100$  pixels. The fractional abundances of the endmembers follow a Dirichlet distribution uniformly over the probability simplex [69]. The resulting observations exhibit spatial homogeneity as described in Fig. 3.2, which shows the true abundances of the endmembers. After generating DC2 following the procedure described above, it was contaminated with i.i.d. Gaussian noise for three SNR levels: 20dB, 30dB and 40dB.

### **3.4.2 Results and discussion**

In this section we test the performance of the proposed TV regularizer combined with sparse unmixing formulations using the two simulated data cubes DC1 and DC2. We also include the original SUnSAL and NCLS formulations. The first part of this section is dedicated to an exhaustive analysis of the original formulation of the SUnSAL-TV algorithm, i.e. using a non-isotropic TV regularizer. The second part is dedicated to a comparison between the non-isotropic and the isotropic versions of the TV regularizer. The algorithms were tested using different values of the parameters  $\lambda$  and  $\lambda_{TV}$ :  $0, 5 \cdot 10^{-4}, 10^{-3}, 5 \cdot 10^{-3}, 0.01, 0.05, 0.1, 0.3, 0.5$  and 1. All possible combinations of these parameters were considered.

#### **Performance of the non-isotropic SUnSAL-TV in simulated environment**

Table 3.1 shows the SRE(dB) results achieved by the different tested methods with the two considered simulated data sets, using all considered SNR levels. On the other hand, Table 3.2

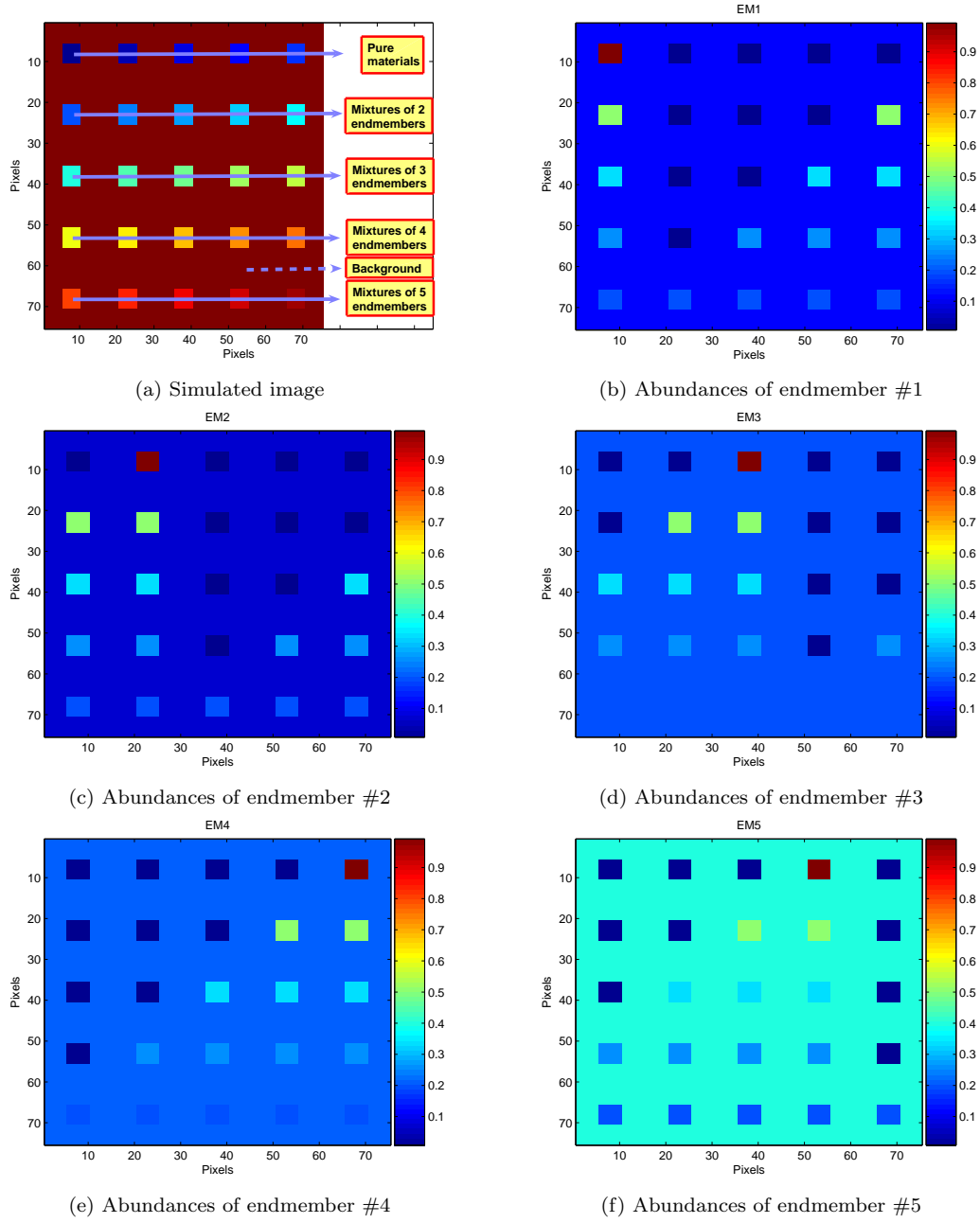


Figure 3.1: True fractional abundances of endmembers in the simulated data cube 1 (DC1).

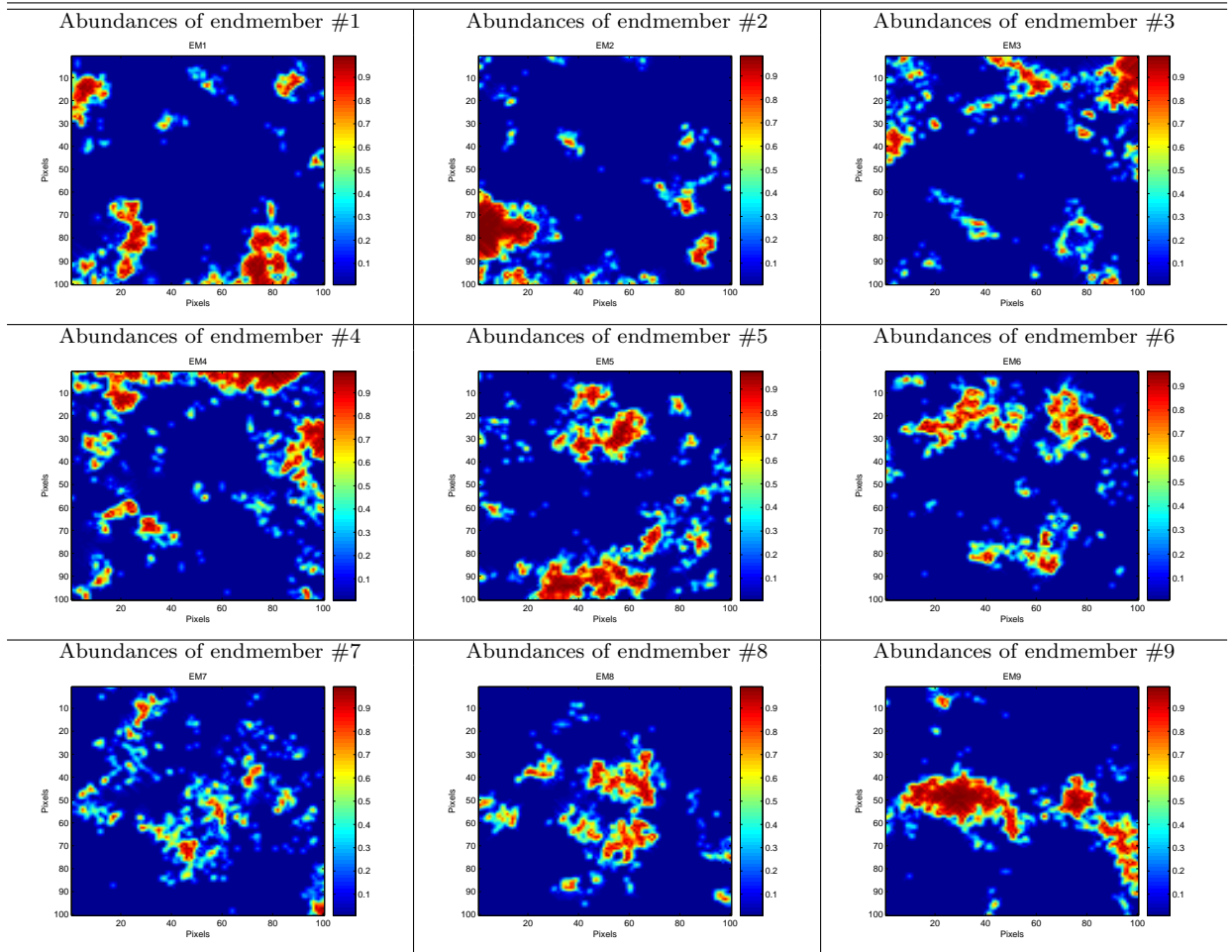


Figure 3.2: True fractional abundances of endmembers in the simulated data cube 2 (DC2).

shows the  $p_s$  results achieved by the different methods for the same data cubes. In both tables, we only report the best scores obtained across the considered parameter range (the optimal parameters for which the reported values were obtained are indicated in the parentheses).

Table 3.1: SRE(dB) values achieved after applying different unmixing methods to simulated data (the optimal parameters for which the reported values were achieved are indicated in the parentheses).

Data cube	SNR (dB)	NCLS ( $\lambda = 0, \lambda_{TV} = 0$ )	NCLS-TV ( $\lambda = 0, \lambda_{TV} \neq 0$ )	SUnSAL ( $\lambda \neq 0, \lambda_{TV} = 0$ )	SUnSAL-TV ( $\lambda \neq 0, \lambda_{TV} \neq 0$ )
DC1	20	2.1376	10.6206 ( $\lambda_{TV} = 0.05$ )	3.8954 ( $\lambda = 0.05$ )	10.6280 ( $\lambda = 5 \cdot 10^{-4}; \lambda_{TV} = 0.05$ )
	30	7.5037	11.7573 ( $\lambda_{TV} = 0.01$ )	8.9476 ( $\lambda = 0.01$ )	11.7677 ( $\lambda = 5 \cdot 10^{-4}; \lambda_{TV} = 0.01$ )
	40	10.048	12.6539 ( $\lambda_{TV} = 0.01$ )	10.944 ( $\lambda = 0.005$ )	12.6753 ( $\lambda = 5 \cdot 10^{-4}; \lambda_{TV} = 0.005$ )
DC2	20	1.0655	5.2458 ( $\lambda_{TV} = 0.01$ )	2.8945 ( $\lambda = 0.05$ )	5.912 ( $\lambda = 0.01; \lambda_{TV} = 0.01$ )
	30	5.9806	10.654 ( $\lambda_{TV} = 0.005$ )	7.8206 ( $\lambda = 0.01$ )	11.186 ( $\lambda = 0.005; \lambda_{TV} = 0.005$ )
	40	12.4347	13.0128 ( $\lambda_{TV} = 0.001$ )	12.561 ( $\lambda = 0.001$ )	14.6485 ( $\lambda = 0.001; \lambda_{TV} = 0.001$ )

Table 3.2:  $p_s$  values values achieved after applying different unmixing methods to simulated data (the optimal parameters for which the reported values were achieved are indicated in the parentheses).

Data cube	SNR (dB)	NCLS ( $\lambda = 0, \lambda_{TV} = 0$ )	NCLS-TV ( $\lambda = 0, \lambda_{TV} \neq 0$ )	SUnSAL ( $\lambda \neq 0, \lambda_{TV} = 0$ )	SUnSAL-TV ( $\lambda \neq 0, \lambda_{TV} \neq 0$ )
DC1	20	0.1076	0.9733 ( $\lambda_{TV} = 0.05$ )	0.4263 ( $\lambda = 0.05$ )	0.9733 ( $\lambda = 5 \cdot 10^{-4}; \lambda_{TV} = 0.05$ )
	30	0.8999	0.9955 ( $\lambda_{TV} = 0.01$ )	0.9468 ( $\lambda = 0.01$ )	0.9956 ( $\lambda = 5 \cdot 10^{-4}; \lambda_{TV} = 0.01$ )
	40	0.9696	0.9955 ( $\lambda_{TV} = 0.01$ )	0.9877 ( $\lambda = 0.005$ )	0.9956 ( $\lambda = 5 \cdot 10^{-4}; \lambda_{TV} = 0.005$ )
DC2	20	0.2041	0.5379 ( $\lambda_{TV} = 0.01$ )	0.384 ( $\lambda = 0.05$ )	0.6458 ( $\lambda = 0.01; \lambda_{TV} = 0.01$ )
	30	0.6046	0.9549 ( $\lambda_{TV} = 0.005$ )	0.7608 ( $\lambda = 0.01$ )	0.9558 ( $\lambda = 0.005; \lambda_{TV} = 0.005$ )
	40	0.9607	0.9998 ( $\lambda_{TV} = 0.001$ )	0.9805 ( $\lambda = 0.001$ )	0.9998 ( $\lambda = 0.001, \lambda_{TV} = 0.001$ )

From Tables 3.1 and 3.2, we can conclude that the inclusion of the TV regularizer offers the potential to improve unmixing performance in two different analysis scenarios, i.e. when the sparsity is imposed explicitly (SUnSAL), and also when it is not enforced (NCLS). For high SNR values, the improvements obtained with regards to the standard sparse unmixing formulations (SUnSAL and NCLS) are not significant. This is due to the fact that, with low noise conditions,



NCLS and the  $l_2 - l_1$  norm optimization solution are able to recover the fractional abundances with good accuracy. However, as the noise increases, the spatial term becomes more important and improves significantly the quality of unmixing results as it can be observed in the results obtained by SUnSAL-TV and NCLS-TV for SNR=20dB in Tables 3.1 and 3.2.

For illustrative purposes, Figs. 3.3 (DC1) and 3.4 (DC2) show the computed values of SRE(dB) as a function of both parameters  $\lambda$  and  $\lambda_{TV}$ . Here, we do not consider values larger than 0.3 for the two aforementioned parameters as we have experimentally observed that such values lead to poor performances in our experiments. Since the plots obtained for the  $p_s$  metric are very similar, we do not report them here for space considerations. From Figs. 3.3 and 3.4 it can be observed that, for the two considered scenes with different SNR levels, the best unmixing performances were achieved for relatively small values of the parameters. The improvements in unmixing performance resulting from the inclusion of the TV regularizer are more apparent when the SNR is low, while the performance of all methods becomes more similar as the SNR is increased. These observations are in line with those already reported in Tables 3.1 and 3.2.

Figs. 3.5 and 3.6 respectively show the abundance maps estimated for one randomly selected endmember in DC1 and DC2 (considering different noise levels). Since the abundance maps estimated for other endmembers exhibited similar behavior, we only report the results observed for endmember #5 in DC1 (see Fig. 3.1) and for endmember #9 in DC2 (see Fig. 3.2). The abundance maps displayed in Figs. 3.5 and 3.6 were obtained using optimal values for parameters  $\lambda$  and  $\lambda_{TV}$  (see Tables 3.1 and 3.2). From Figs. 3.5 and 3.6, it can be seen that the spatial term based on the TV regularizer improves both the NCLS and the SUnSAL solutions. In qualitative fashion, we can observe that the regions with high fractional abundance of the considered endmember are better delineated, while mixed regions with low concentration of the considered endmember are more homogeneous in nature. No matter the level of noise, the solutions get spatial consistency and the spatial distribution of the materials is determined with good accuracy in both cases. Sparse solutions are particularly needed when the SNR is low, as reported in Tables 3.1 and 3.2.

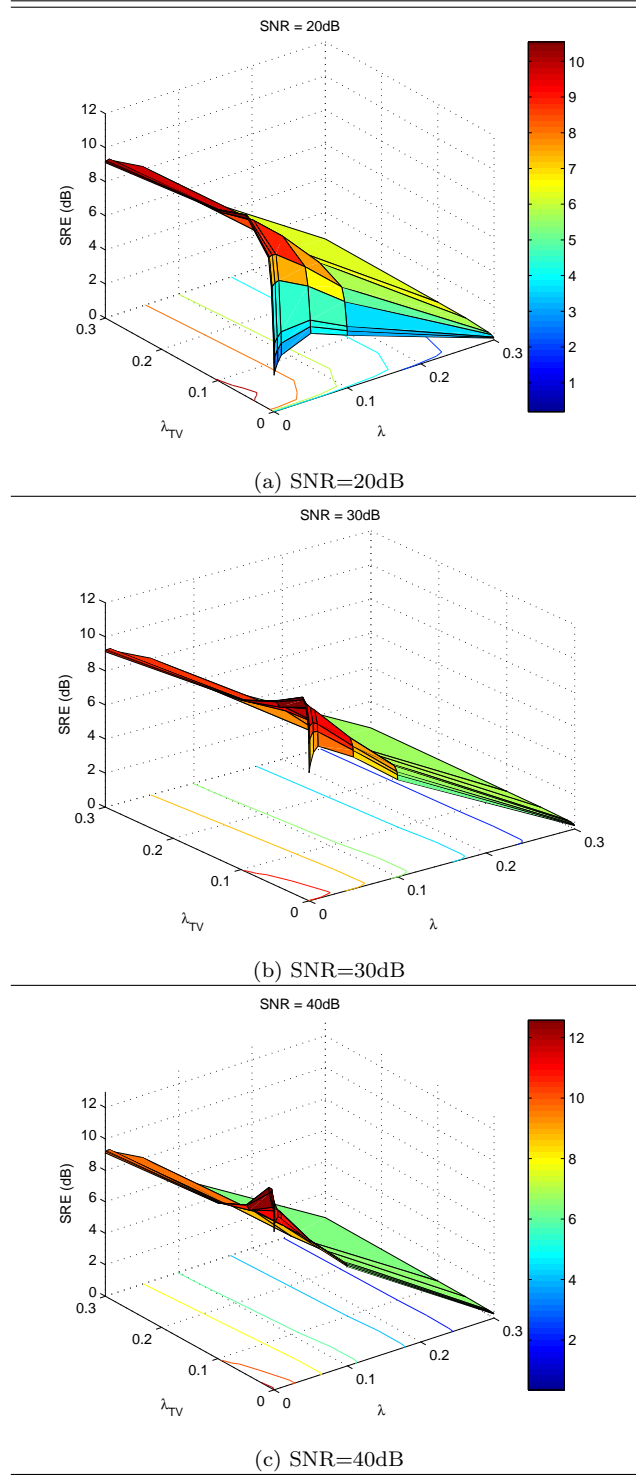


Figure 3.3: SRE(dB) as a function of parameters  $\lambda$  and  $\lambda_{TV}$  for DC1 with different SNR levels.

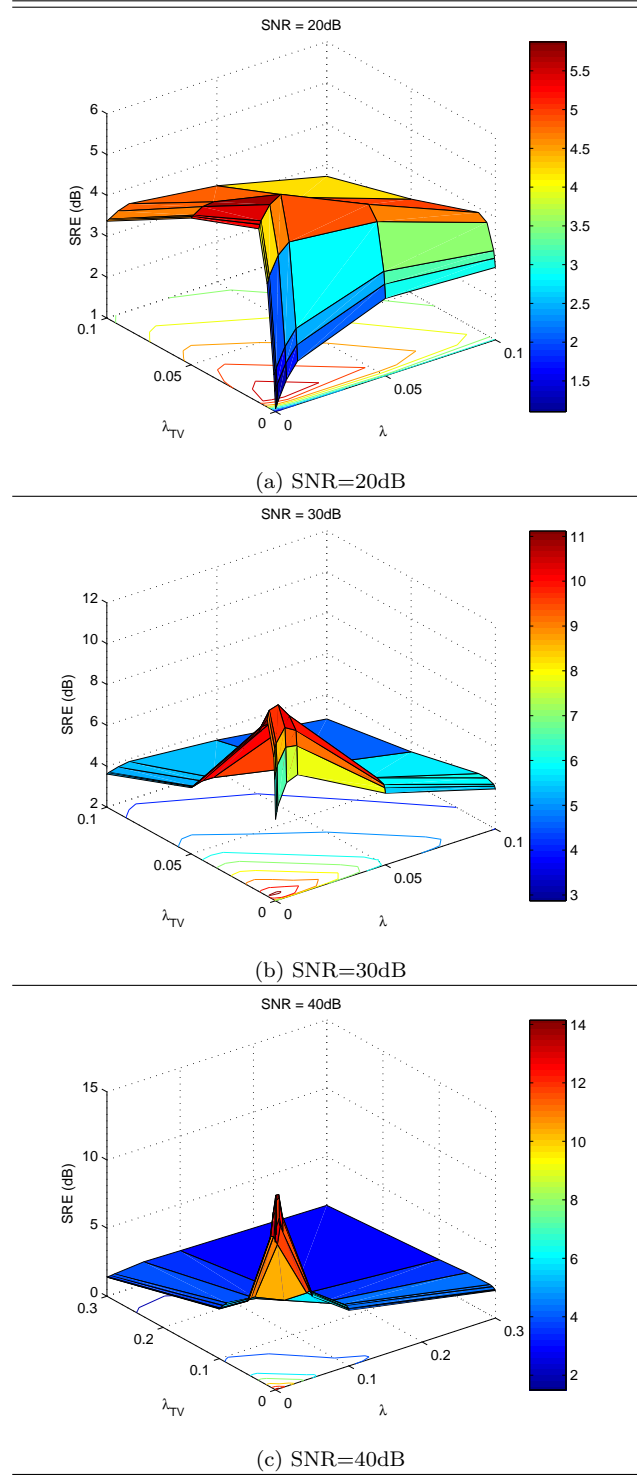


Figure 3.4: SRE(dB) as a function of parameters  $\lambda$  and  $\lambda_{TV}$  for DC2 with different SNR levels.

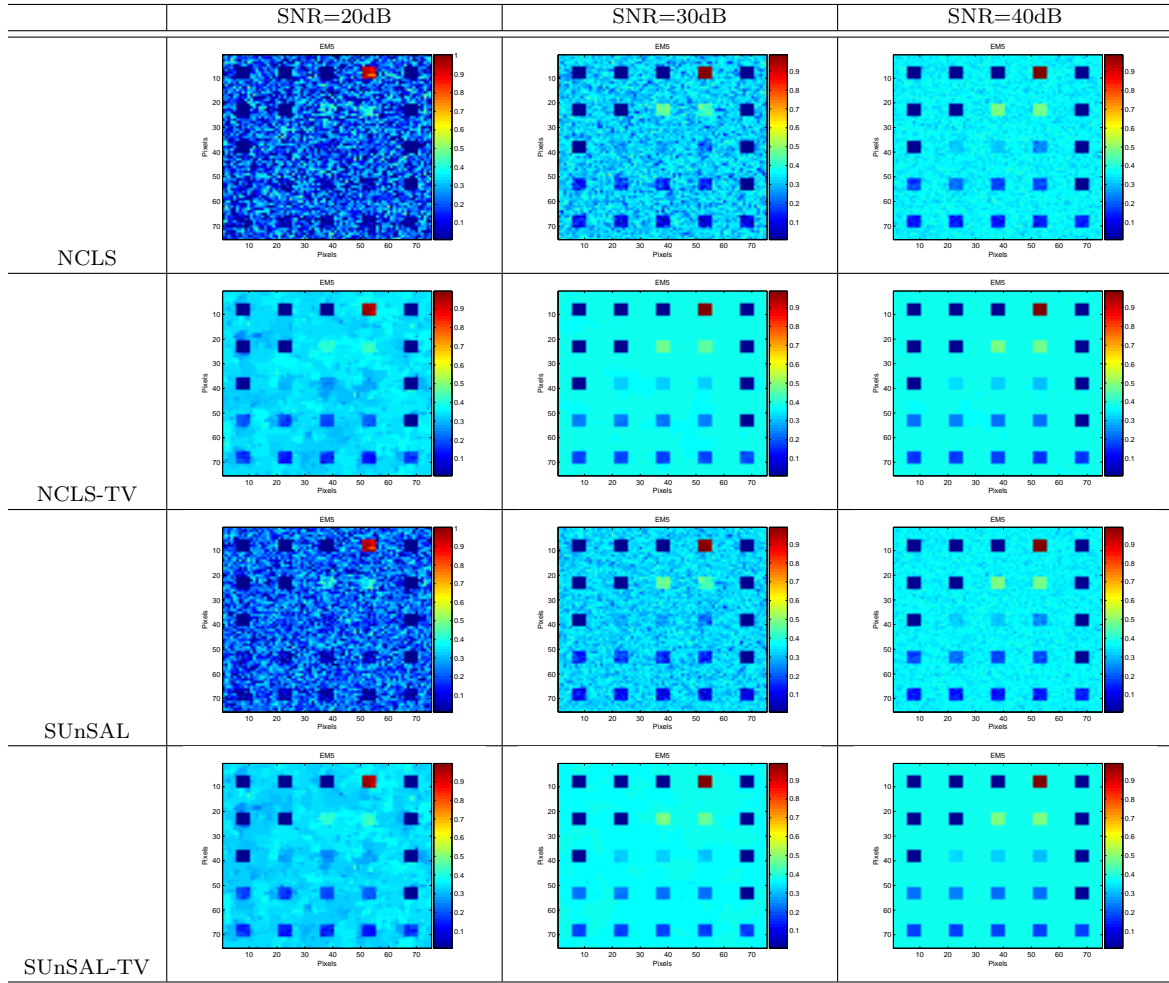


Figure 3.5: Abundance maps obtained by different unmixing methods for endmember #5 in DC1.

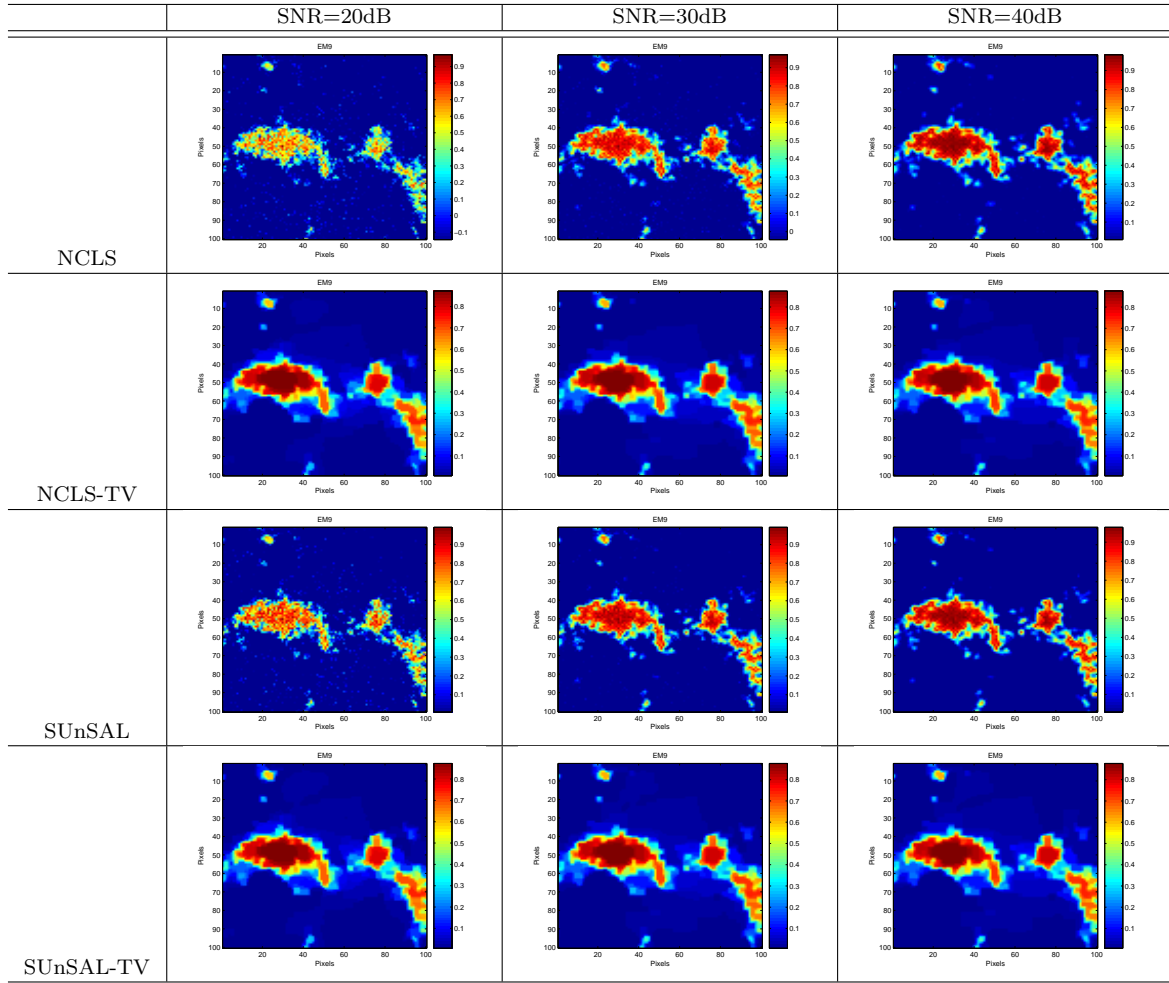


Figure 3.6: Abundance maps obtained by different unmixing methods for endmember #9 in DC2.

Fig. 3.7 shows the fractional abundance estimations obtained for each endmember material in the  $\mathbf{A}_1$  library (as a function of the pixel index in the scene DC1 simulated with SNR of 30dB) by the SUnSAL and SUnSAL-TV methods, along with the ground-truth abundances. To facilitate the visualization, background pixels are removed from the plots in the leftmost column of Fig. 3.7. In order to better visualize the impact of applying the TV regularizer, the rightmost column of Fig. 3.7 shows the same abundances for only 100 selected pixels (indicated by the green rectangle in the upper-leftmost plot in Fig. 3.7). The parameters used correspond to the ones reported in Table 3.1.

From Fig. 3.7, it can be seen graphically that the TV regularizer imposes spatial consistency in the unmixing results. The lines (denoting the abundance of a certain endmember in all pixels of the image) estimated by SUnSAL-TV are more similar to those in the ground-truth than the ones estimated by SUnSAL. After applying SUnSAL, there are many low abundance values estimated for endmembers which are not actually present in the image, but the TV regularizer vanishes those values and provides an overall estimate which is closer to ground-truth values. It is also remarkable that, at first sight, it would appear that both SUnSAL and SUnSAL-TV encounter problems in accurately locating one endmember (i.e., the one situated around line 150 of the upper-leftmost plot in Fig. 3.7). However, we must note that the spectral signature of this endmember corresponds to the *muscovite* mineral, and there are eleven spectra in the library corresponding to different variations of this mineral (all very similar in spectral terms –within 2.52 degrees– and located around line 150 of the upper-leftmost plot in Fig. 3.7). As a result, we conclude that the abundance estimates provided by SUnSAL-TV are highly accurate and indeed correlated with the ground-truth ones. With the aforementioned observations in mind, we believe that the combination of the TV regularizer with sparse unmixing methods offers promising results. Although the results obtained with simulated data sets are quite encouraging and revealing of the potential of including spatial information in sparse unmixing formulations, further experiments should be conducted with real hyperspectral scenes in order to fully substantiate our findings in real analysis scenarios.

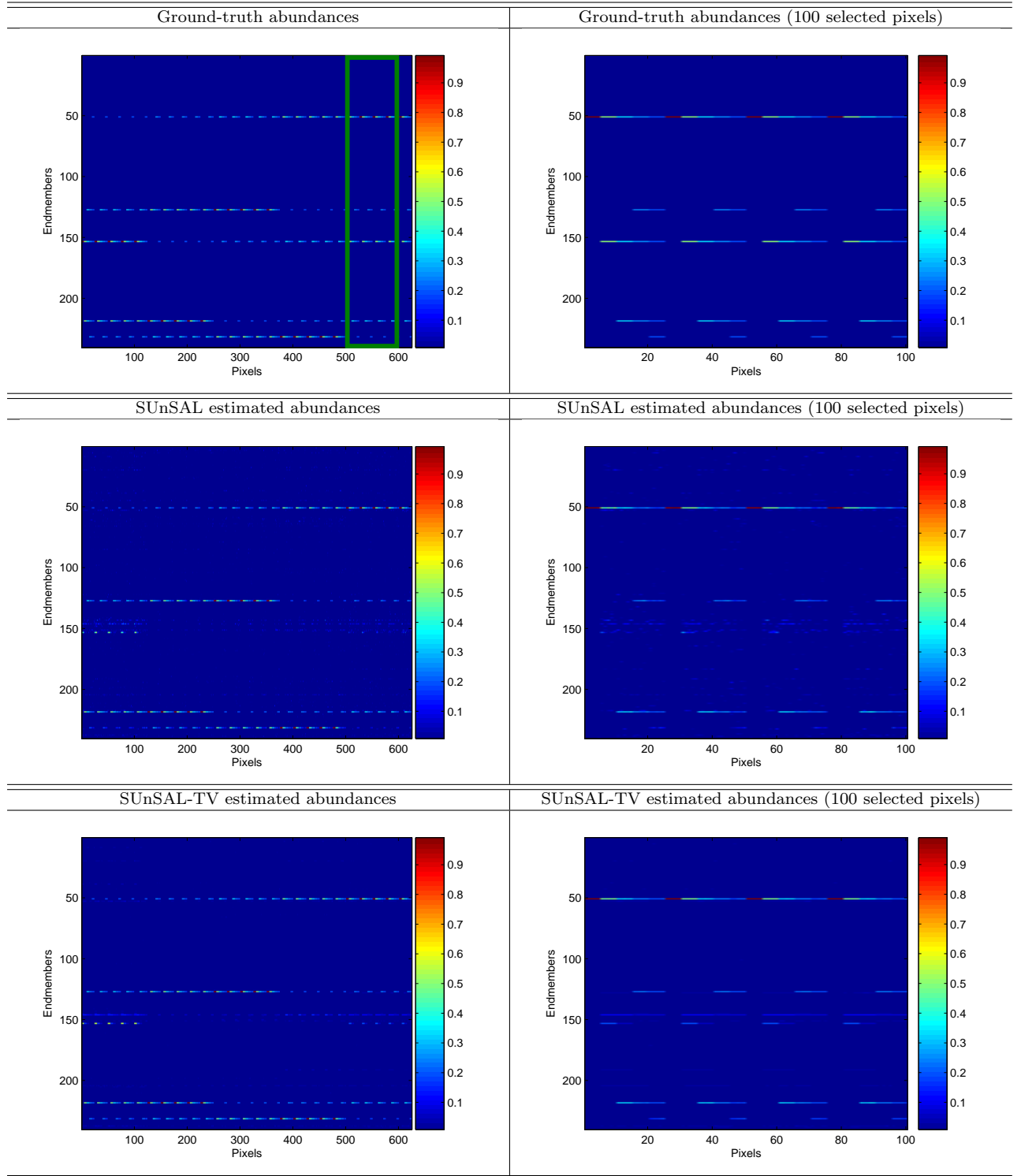


Figure 3.7: Ground-truth, SUnSAL and SUnSAL-TV estimated abundances obtained for each endmember material in the  $\mathbf{A}_1$  library in the the scene DC1, simulated with SNR of 30dB (leftmost column), and the same results for 100 selected pixels marked in a green rectangle in the upper-leftmost plot (rightmost column).

To conclude this subsection Table 3.3 illustrates the per-pixel execution times for the algorithms compared in this section. The values reported correspond to the average times, measured after processing 600 pixels randomly chosen from DC1 and DC2 (300 pixels from each datacube, 100 for each noise level), while the spectral libraries used were the ones shown in subsection 3.4.1). The algorithms were implemented using Matlab7 on a desktop PC equipped with an Intel Core 2 Quad CPU (at 2.33GHz) and 4GB of RAM memory.

Table 3.3: Average per-pixel processing times (in seconds) measured after applying the considered unmixing algorithms to 600 randomly chosen pixels from simulated images DC1 and DC2, on a desktop PC equipped with an Intel Core 2 Quad CPU (at 2.33 GHz) and 4GB of RAM memory.

	NCLS	NCLS-TV	SUnSAL	SUnSAL-TV
Time [s]	0.026	1.614	0.028	1.625

### Isotropic versus Non-Isotropic TV Regularizers

This subsection compares the two types of the TV regularizers implemented in the SUnSAL-TV algorithm: the non-isotropic version defined in Eq. (3.6), and the isotropic version defined in Eq. (3.7). The SUnSAL-TV algorithm was slightly changed in order to deal with this version of the TV regularizer, then applied to DC2. The performance was measured using the same indicators as for SUnSAL-TV with non-isotropic regularizer. The goal is to analyze the influence of the different types of the TV regularizer in the unmixing results, when the solutions are explicitly constrained to be sparse.

Table 3.4 shows the SRE(dB) results achieved by SUnSAL-TV with the considered simulated data set, using different SNR levels, for the two versions of the TV regularizer (isotropic and non-isotropic). On the other hand, Table 3.5 shows the  $p_s$  results achieved by SUnSAL-TV for the same data cube. In both tables, we only report the best scores obtained across the considered parameter range (the optimal parameters for which the reported values were obtained are indicated in the parentheses).

From Tables 3.4 and 3.5, we can conclude that there are no significant variations in the performance of the SUnSAL-TV algorithm when different types of TV regularizers (isotropic



Table 3.4: SRE(dB) values achieved after applying different unmixing methods to DC2 (the optimal parameters for which the reported values were achieved are indicated in the parentheses).

Data cube	SNR (dB)	SUnSAL-TV non-isotropic ( $\lambda \neq 0, \lambda_{TV} \neq 0$ )	SUnSAL-TV isotropic ( $\lambda \neq 0, \lambda_{TV} \neq 0$ )
DC2	20	5.912 ( $\lambda = 0.01; \lambda_{TV} = 0.01$ )	5.7196 ( $\lambda = 0.01; \lambda_{TV} = 0.01$ )
	30	11.186 ( $\lambda = 0.005; \lambda_{TV} = 0.005$ )	11.6832 ( $\lambda = 0.005; \lambda_{TV} = 0.005$ )
	40	14.6485 ( $\lambda = 0.001; \lambda_{TV} = 0.001$ )	14.4423 ( $\lambda = 0.001; \lambda_{TV} = 0.001$ )

Table 3.5:  $p_s$  values values achieved after applying different unmixing methods to DC2 (the optimal parameters for which the reported values were achieved are indicated in the parentheses).

Data cube	SNR (dB)	SUnSAL-TV non-isotropic ( $\lambda \neq 0, \lambda_{TV} \neq 0$ )	SUnSAL-TV isotropic ( $\lambda \neq 0, \lambda_{TV} \neq 0$ )
DC2	20	0.6458 ( $\lambda = 0.01; \lambda_{TV} = 0.01$ )	0.6279 ( $\lambda = 0.01; \lambda_{TV} = 0.01$ )
	30	0.9558 ( $\lambda = 0.005; \lambda_{TV} = 0.005$ )	0.9742 ( $\lambda = 0.001; \lambda_{TV} = 0.005$ )
	40	0.9998 ( $\lambda = 0.001, \lambda_{TV} = 0.001$ )	1 ( $\lambda = 0.001; \lambda_{TV} = 0.001$ )

versus non-isotropic) are used. Moreover, the optimal parameters are equal for the two versions of the TV regularizer. It seems that the non-isotropic version performs slightly better in highly noisy environment (for instance, in the case with SNR=20dB), but the isotropic version achieves slightly better results in terms of  $p_s$  when the noise is not significant. Note the remarkable values achieved for the probability of success with the isotropic regularizer when the SNR=40dB.

Despite the similarities observed in the two versions of SUnSAL-TV algorithm (isotropic and non-isotropic) in terms of the considered performance discriminators, there are obvious qualitative differences. In order to illustrate this observation, Fig. 3.8 shows the abundance maps obtained for the ninth endmember present in the considered simulated dataset with the two versions of the TV regularizer, both when the sparsity of the solution is imposed explicitly (SUnSAL-TV) and when it is not (NCLS-TV), for all the considered noise levels. From Fig. 3.8, it can be seen that the unmixing results are qualitatively different when different types of

TV regularizers are used. Specifically, the isotropic version enforces the presence of regions with non-zero abundances in the scene, while the non-isotropic version tends to remove small areas in the scene dominated by non-zero abundances.

### 3.5 Experiments with Real Data

The scene used in our real data experiments is the dataset described in subsection 2.5 of the previous chapter. The classification maps obtained with the Tricorder 3.3 software product [34] were again used in our qualitative evaluation of the results provided by the SUnSAL-TV algorithm. Before unmixing the AVIRIS Cuprite hyperspectral data, we addressed possible calibration mismatches between the real image spectra and the spectra available in the library. This is because, even though we are working with atmospherically corrected data in reflectance units, these calibration interferers are still present due to the rather different acquisition conditions of the two data types. In order to minimize these mismatches, we applied the band-dependent correction strategy described in subsection 2.5 of the previous chapter to the original data set, which amounts at replacing the data set  $\mathbf{Y}$  with  $\mathbf{CY}$ , where  $\mathbf{C}$  is a diagonal matrix that minimizes the modeling error, i.e.:

$$\hat{\mathbf{C}} = \arg \min_{\mathbf{C}, \mathbf{X} \geq \mathbf{0}, \mathbf{1}_m^T \mathbf{X} = \mathbf{1}_n^T} \|\mathbf{A}_1 \mathbf{X} - \mathbf{CY}\|_2, \quad (3.13)$$

where  $\mathbf{X} \geq \mathbf{0}$  is the fractional abundance matrix. The problem in (3.13) is non-convex and, thus, very hard to solve exactly. As described in subsection 2.5, we have computed a sub-optimal solution to this problem by alternating the minimization with respect to  $\mathbf{C}$  and to  $\mathbf{X}$  [58]. In our experiments, we used the matrix  $\mathbf{A}_1$  described in subsection 3.4.1 and also a library (denoted by  $\mathbf{A}$ ) which contains 498 minerals randomly selected from the USGS library. The correction matrices corresponding to  $\mathbf{A}_1$  and  $\mathbf{A}$  are respectively displayed in Figs. 3.9(a) and 3.9(b).

Fig. 3.10 shows a visual (qualitative) comparison between the fractional abundance maps

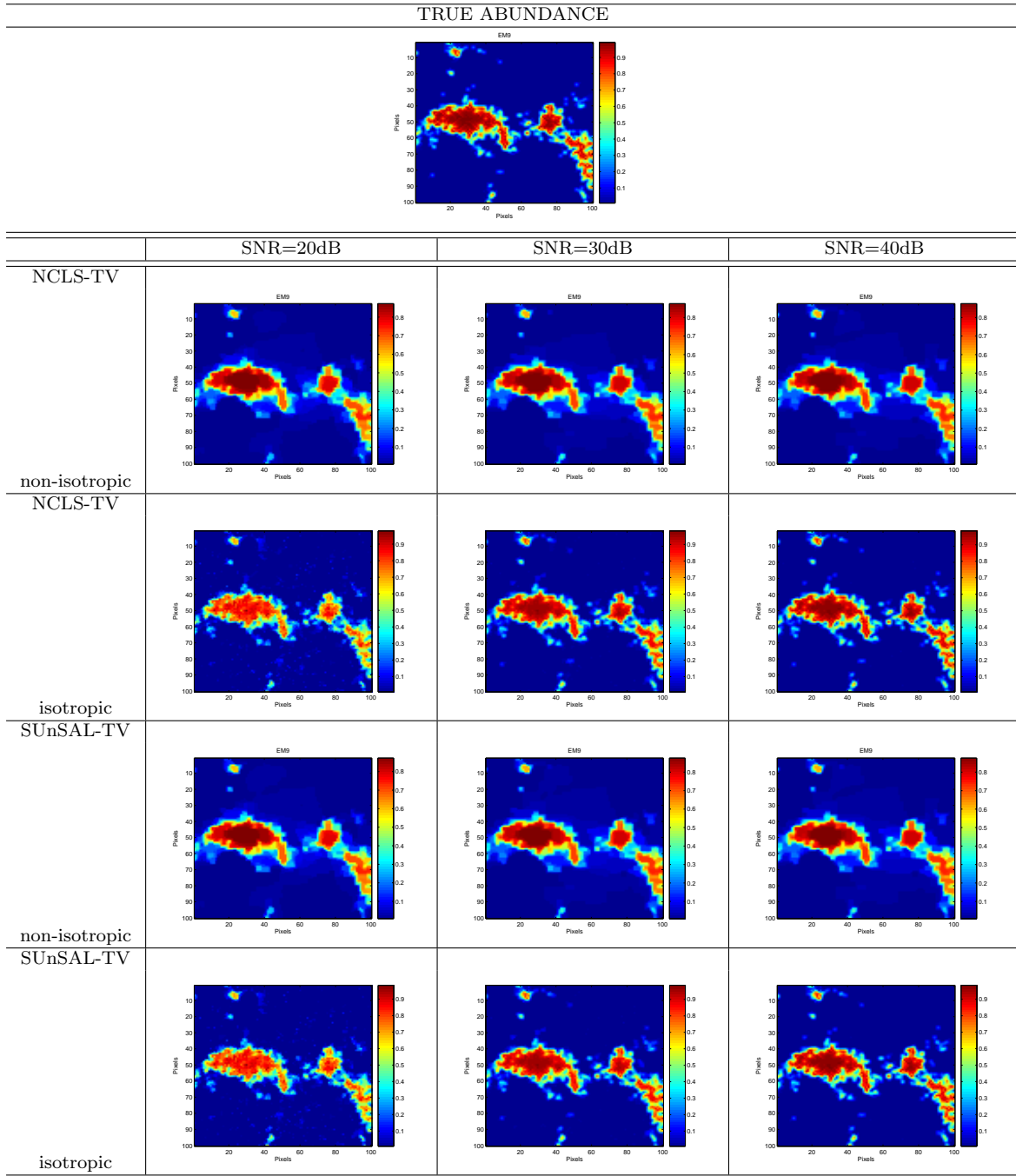


Figure 3.8: Abundance maps obtained by NCLS-TV and SUnSAL-TV for endmember #9 in DC2 and for the two variants of the TV regularizer.

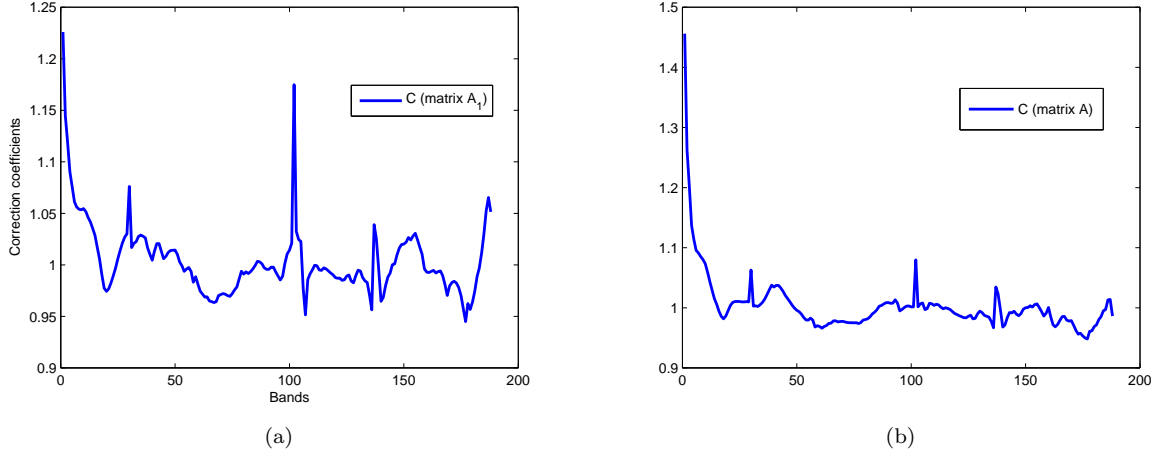


Figure 3.9: Plot of diagonal values of the correction matrix  $\mathbf{C}$  for the following spectral libraries: (a)  $\mathbf{A}_1$ , and (b)  $\mathbf{A}$ .

estimated for the minerals: *alunite*, *buddingtonite* and *chalcedony* by applying the NCLS, NCLS-TV, SUnSAL and SUnSAL-TV algorithms to the AVIRIS Cuprite scene using the library  $\mathbf{A}_1$ . These minerals are known to be present (in prominent fashion) in the Cuprite mining district. For comparative purposes, the spatial distribution maps of these materials extracted from the Tricorder software product in Fig. 2.15 are also displayed in Fig. 3.10. On the other hand, Fig. 3.11 displays the abundance maps estimated for the same minerals using the different unmixing algorithms considered in this work and the spectral library  $\mathbf{A}$ . The parameters used in all cases (after empirical optimization) were  $\lambda = \lambda_{TV} = 10^{-3}$  for NCLS-TV, SUnSAL and SUnSAL-TV. For the NCLS, both  $\lambda$  and  $\lambda_{TV}$  were set to zero.

From Figs. 3.10 and 3.11, it can be observed that the abundance maps obtained by the methods with the TV spatial regularizer exhibit good spatial consistency of minerals of interest and less outliers than the maps without such regularizer. This can be appreciated, for instance, in the *buddingtonite* maps in both figures. In this particular mineral, the TV term helps both NCLS-TV and SUnSAL-TV reduce towards zero some outlier values of high abundance of the mineral in isolated regions of the image that can be observed for the NCLS and SUnSAL results. In this case, the TV term allows obtaining a better characterization of the *buddingtonite* mineral (which appears as an anomaly in the scene) in accordance with the Tricorder 3.3 software product.

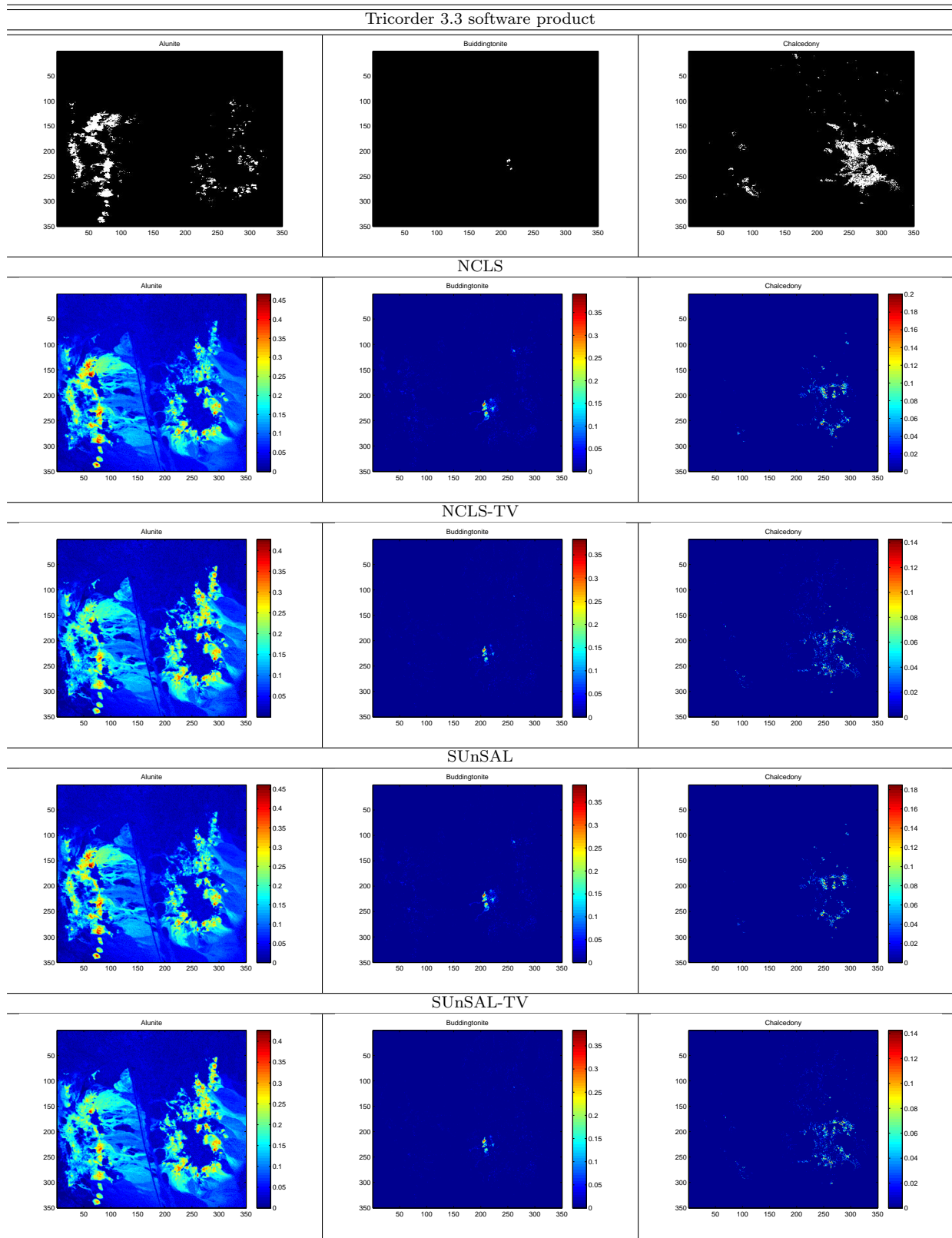


Figure 3.10: Abundance maps estimated for the minerals: *alunite*, *buddingtonite* and *chalcedony* by applying the NCLS, NCLS-TV, SUnSAL and SUnSAL-TV algorithms to the AVIRIS Cuprite scene using the library  $\mathbf{A}_1$ .

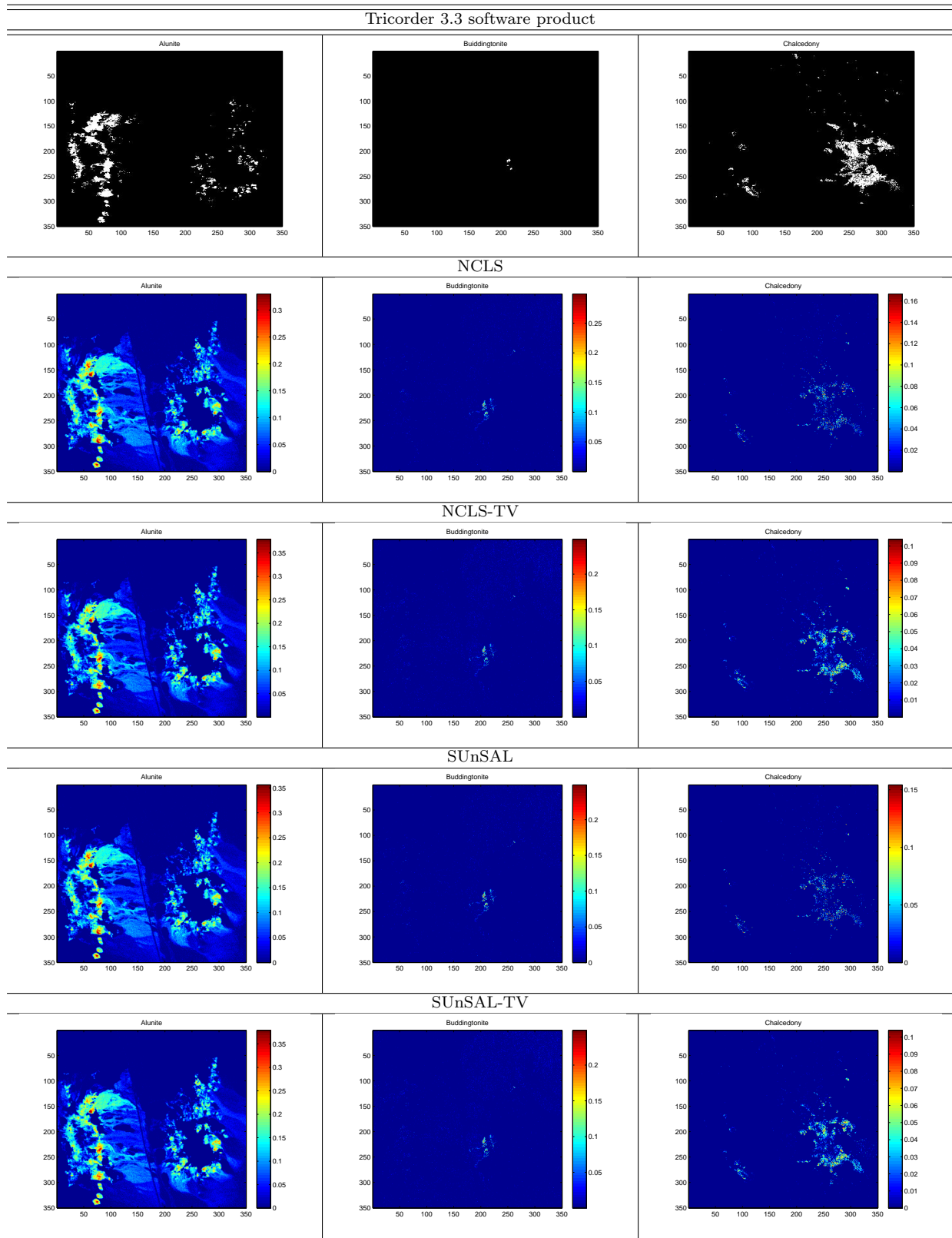


Figure 3.11: Abundance maps estimated for the minerals: *alunite*, *buddingtonite* and *chalcedony* by applying the NCLS, NCLS-TV, SUnSAL and SUnSAL-TV algorithms to the AVIRIS Cuprite scene using the library **A**.

Another important observation from Figs. 3.10 and 3.11 is that the results obtained by sparse unmixing methods using  $\mathbf{A}_1$  and  $\mathbf{A}$  are very similar, indicating that sparse unmixing is quite insensitive to the number of spectra in the reference library, and regardless of the inclusion of the TV term in the solution of the sparse unmixing problem. Although the effect of the TV regularizer is not as apparent in the real image experiments as in the simulated image experiments (which is probably due to the fact that the AVIRIS Cuprite image used in experiments is characterized by high SNR), the behavior observed is in line with the results obtained for the experiments carried out on simulated data, indicating that the inclusion of spatial information in sparse unmixing by means of the proposed TV regularizer can assist in obtaining piecewise smooth abundance maps with less outliers and high spatial consistency. Further experiments with additional hyperspectral scenes and libraries should be conducted in future work in order to fully objectify our findings.

### 3.6 Conclusions and future work

Sparse unmixing has been recently introduced as a powerful methodology to solve the spectral unmixing problem by taking advantage of spectral libraries of materials measured on the ground, thus reducing the dependency of unmixing methods on the availability of pure spectral signatures in the input data or on the ability of an endmember extraction algorithm to identify the number and spectra of such pure signatures. Despite the success of sparse unmixing in different applications, a limitation of this approach has been the fact that it does not consider the spatial correlation between the image features in the unmixing process. To circumvent this limitation, in this work we have revisited the sparse unmixing formulation and introduced a TV regularizer term aimed at imposing spatial consistency in hyperspectral sparse unmixing solutions. A new algorithm, called *sparse unmixing via variable splitting augmented Lagrangian and total variation* (SUnSAL-TV) has been specifically developed for this purpose. Our experimental results (conducted using both simulated and real hyperspectral data sets) indicate that the inclusion of the TV regularizer offers the potential to improve unmixing performance in two different

analysis scenarios, i.e. when the sparsity is imposed explicitly (SUnSAL), and also when it is not enforced (NCLS). This is particularly the case for scenarios with high noise levels. In this way, the limitations of sparse unmixing approaches related with the high coherence of spectral signatures or the lack of spatial-contextual information when solving the unmixing problem have been significantly mitigated. Our future work will focus on a full evaluation of isotropic versus non-isotropic TV regularization, defined in the spatial dimension, and also on the development of fast parallel algorithms able to cope with the high computational complexity of the proposed approach. It should be noted that this issue is subject to further improvements related with the inherently parallel nature of sparse unmixing algorithms combined with the TV regularizer, which are expected to scale linearly on parallel systems such as multi-core processors or graphics processing units (GPUs).

## Appendix –

In this appendix, we detail the SUnSAL-TV algorithm introduced in Section 3.3. We start by expanding the augmented Lagrangian introduced in (3.12):

$$\begin{aligned} \mathcal{L}(\mathbf{U}, \mathbf{V}_1, \mathbf{V}_2, \mathbf{V}_3, \mathbf{V}_4, \mathbf{V}_5, \mathbf{D}_1, \mathbf{D}_2, \mathbf{D}_3, \mathbf{D}_4, \mathbf{D}_5) = & \quad (3.14) \\ & \frac{1}{2} \|\mathbf{V}_1 - \mathbf{Y}\|_F^2 + \lambda \|\mathbf{V}_2\|_{1,1} + \lambda_{TV} \|\mathbf{V}_4\|_{1,1} + \iota_{R+}(\mathbf{V}_5) + \\ & \frac{\mu}{2} \|\mathbf{A}\mathbf{U} - \mathbf{V}_1 - \mathbf{D}_1\|_F^2 + \frac{\mu}{2} \|\mathbf{U} - \mathbf{V}_2 - \mathbf{D}_2\|_F^2 + \frac{\mu}{2} \|\mathbf{U} - \mathbf{V}_3 - \mathbf{D}_3\|_F^2 + \\ & \frac{\mu}{2} \|\mathbf{H}\mathbf{V}_3 - \mathbf{V}_4 - \mathbf{D}_4\|_F^2 + \frac{\mu}{2} \|\mathbf{U} - \mathbf{V}_5 - \mathbf{D}_5\|_F^2. \end{aligned}$$

The pseudocode of SUnSAL-TV is shown in Algorithm 3.2. It is the expansion of the ADDM algorithm presented in Algorithm 3.1, with a single optimization with respect to  $\mathbf{V}_3$  and with respect to  $\mathbf{V}_4$ , per iteration.

We give now details about step 3 of Algorithm 3.2. The goal of this step is to determine the value of the variable  $\mathbf{U}$  at each iteration. Given that we run an optimization over the variable  $\mathbf{U}$ , the terms of the objective function (3.9) which do not contain this variable are not taken into



---

**Algorithm 3.2** Pseudocode of the SUnSAL-TV algorithm.

---

1. **Initialization:** set  $k = 0$ , choose  $\mu \geq 0, \mathbf{U}^{(0)}, \mathbf{V}_1^{(0)}, \dots, \mathbf{V}_5^{(0)}, \mathbf{D}_1^{(0)}, \dots, \mathbf{D}_5^{(0)}$
2. **repeat:**
  3.  $\mathbf{U}^{(k+1)} \leftarrow \arg \min_{\mathbf{U}} \mathcal{L}(\mathbf{U}, \mathbf{V}_1^{(k)}, \dots, \mathbf{V}_5^{(k)}, \mathbf{D}_1^{(k)}, \dots, \mathbf{D}_5^{(k)})$
  4. **for**  $i = 1, \dots, 5$ 
    5.  $\mathbf{V}_i^{(k+1)} \leftarrow \arg \min_{\mathbf{V}_i} \mathcal{L}(\mathbf{U}^{(k)}, \mathbf{V}_1^{(k)}, \dots, \mathbf{V}_i, \dots, \mathbf{V}_5^{(k)})$
  6. **end for**
  7. **Update Lagrange multipliers:**

$$\begin{aligned} \mathbf{D}_1^{(k+1)} &\leftarrow \mathbf{D}_1^{(k)} - \mathbf{A}\mathbf{U}^{(k+1)} + \mathbf{V}_1^{(k+1)} \\ \mathbf{D}_2^{(k+1)} &\leftarrow \mathbf{D}_2^{(k)} - \mathbf{U}^{(k+1)} + \mathbf{V}_2^{(k+1)} \\ \mathbf{D}_3^{(k+1)} &\leftarrow \mathbf{D}_3^{(k)} - \mathbf{U}^{(k+1)} + \mathbf{V}_3^{(k+1)} \\ \mathbf{D}_4^{(k+1)} &\leftarrow \mathbf{D}_4^{(k)} - \mathbf{H}\mathbf{V}_3^{(k+1)} + \mathbf{V}_4^{(k+1)} \\ \mathbf{D}_5^{(k+1)} &\leftarrow \mathbf{D}_5^{(k)} - \mathbf{U}^{(k+1)} + \mathbf{V}_5^{(k+1)} \end{aligned}$$
  8. **Update iteration:**  $k \leftarrow k + 1$
  9. **until** some stopping criterion is satisfied.

---

account. The reduced optimization function becomes, then:

$$\begin{aligned} \mathbf{U}^{(k+1)} \leftarrow \arg \min_{\mathbf{U}} \frac{\mu}{2} \|\mathbf{A}\mathbf{U} - \mathbf{V}_1^{(k)} - \mathbf{D}_1^{(k)}\|_F^2 + \frac{\mu}{2} \|\mathbf{U} - \mathbf{V}_2^{(k)} - \mathbf{D}_2^{(k)}\|_F^2 + \\ \frac{\mu}{2} \|\mathbf{U} - \mathbf{V}_3^{(k)} - \mathbf{D}_3^{(k)}\|_F^2 + \frac{\mu}{2} \|\mathbf{U} - \mathbf{V}_5^{(k)} - \mathbf{D}_5^{(k)}\|_F^2. \end{aligned} \quad (3.15)$$

The solution of (3.15) is simply:

$$\mathbf{U}^{(k+1)} \leftarrow (\mathbf{A}^T \mathbf{A} + 3\mathbf{I})^{-1} (\mathbf{A}^T \xi_1 + \xi_2 + \xi_4 + \xi_5), \quad (3.16)$$

where  $\mathbf{I}$  is the identity matrix,  $\mathbf{A}^T$  represents the transpose of  $\mathbf{A}$  and:  $\xi_1 = \mathbf{V}_1^{(k)} + \mathbf{D}_1^{(k)}$ ,  $\xi_2 = \mathbf{V}_2^{(k)} + \mathbf{D}_2^{(k)}$ ,  $\xi_3 = \mathbf{V}_3^{(k)} + \mathbf{D}_3^{(k)}$ ,  $\xi_5 = \mathbf{V}_5^{(k)} + \mathbf{D}_5^{(k)}$ . Notice that matrix  $\mathbf{A}$  acts only on the spectral domain.

On the other hand, step 5 of SUnSAL-TV computes the values of the variables  $\mathbf{V}_1, \dots, \mathbf{V}_5$  at the current iteration. To compute  $\mathbf{V}_1$ , the optimization problem to be solved is:

$$\mathbf{V}_1^{(k+1)} \leftarrow \arg \min_{\mathbf{V}_1} \frac{1}{2} \|\mathbf{V}_1 - \mathbf{Y}\|_F^2 + \frac{\mu}{2} \|\mathbf{A}\mathbf{U}^{(k)} - \mathbf{V}_1 - \mathbf{D}_1^{(k)}\|_F^2, \quad (3.17)$$

whose solution is:

$$\mathbf{V}_1^{(k+1)} \leftarrow \frac{1}{1+\mu} [\mathbf{Y} + \mu(\mathbf{A}\mathbf{U}^{(k)} - \mathbf{D}_1^{(k)})]. \quad (3.18)$$

To compute  $\mathbf{V}_2$ , the optimization problem to be solved is:

$$\mathbf{V}_2^{(k+1)} \leftarrow \arg \min_{\mathbf{V}_2} \lambda \|\mathbf{V}_2\|_{1,1} + \frac{\mu}{2} \|\mathbf{U}^{(k)} - \mathbf{V}_2 - \mathbf{D}_2^{(k)}\|_F^2, \quad (3.19)$$

whose solution is the well-known *soft threshold* [35]:

$$\mathbf{V}_2^{(k+1)} \leftarrow \text{soft}(\xi_2, \lambda/\mu), \quad (3.20)$$

where  $\xi_2 = \mathbf{V}_2^{(k)} + \mathbf{D}_2^{(k)}$  and  $\text{soft}(\cdot, \tau)$  denotes the component-wise application of the soft-threshold function  $y \mapsto \text{sign}(y) \max\{|y| - \tau, 0\}$ .

In order to compute  $\mathbf{V}_3$ , we solve the optimization problem:

$$\mathbf{V}_3^{(k+1)} \leftarrow \arg \min_{\mathbf{V}_3} \frac{\mu}{2} \|\mathbf{U}^{(k)} - \mathbf{V}_3 - \mathbf{D}_3^{(k)}\|_F^2 + \frac{\mu}{2} \|\mathbf{H}\mathbf{V}_3 - \mathbf{V}_4^{(k)} - \mathbf{D}_4^{(k)}\|_F^2, \quad (3.21)$$

having the solution:

$$\mathbf{V}_3^{(k+1)} \leftarrow (\mathbf{H}^T \mathbf{H} + \mathbf{I})^{-1} (\mathbf{U}^{(k)} - \mathbf{D}_3^{(k)} + \mathbf{H}^T \xi_4), \quad (3.22)$$

where  $\xi_4 = \mathbf{V}_4^{(k)} + \mathbf{D}_4^{(k)}$ . Note that  $\mathbf{H}^T \mathbf{H} + \mathbf{I}$  acts only on the spatial domain and can be applied independently, in band-by-band fashion. Since, for each band,  $\mathbf{H}$  is a convolution, it can be computed efficiently using the discrete Fourier transform (DFT) diagonalization.

$\mathbf{V}_4$  is computed by solving the optimization problem:

$$\mathbf{V}_4^{(k+1)} \leftarrow \arg \min_{\mathbf{V}_4} \lambda_{TV} \|\mathbf{V}_4\|_{1,1} + \frac{\mu}{2} \|\mathbf{H}\mathbf{V}_3^{(k)} - \mathbf{V}_4 - \mathbf{D}_4^{(k)}\|_F^2. \quad (3.23)$$

As for (3.19), the solution of (3.23) is the *soft threshold*:

$$\mathbf{V}_4^{(k+1)} \leftarrow \text{soft}(\mathbf{D}_4^{(k)} - \mathbf{H}\mathbf{V}_3^{(k)}, \lambda_{TV}/\mu). \quad (3.24)$$

Finally,  $\mathbf{V}_5$  is computed by solving the following optimization problem:

$$\mathbf{V}_5^{(k+1)} \leftarrow \arg \min_{\mathbf{V}_5} \iota_{R+}(\mathbf{V}_5) + \frac{\mu}{2} \|\mathbf{U}^{(k)} - \mathbf{V}_5 - \mathbf{D}_5^{(k)}\|_F^2. \quad (3.25)$$

In (3.25), the role of the  $\iota_{R+}$  term is to project the solution onto the nonnegative orthant and the value of  $\mathbf{V}_5$  is given by:

$$\mathbf{V}_5^{(k+1)} \leftarrow \max(\mathbf{U}^{(k)} - \mathbf{D}_5^{(k)}, 0). \quad (3.26)$$

Concerning the computational complexity of the SUnSAL-TV algorithm, the most costly steps are the calculus of  $\mathbf{U}$ , which has the order of complexity  $\mathcal{O}(nL^2)$ , and of  $\mathbf{V}_3$ , with the order  $\mathcal{O}(Ln \log n)$ , while the others have computational complexity  $\mathcal{O}(n)$ , where  $L$  is the number of spectral bands and  $n$  is the number of pixels in the image. The overall order of complexity per iteration is given then by  $(nL \cdot \max\{L, \log n\})$ . It should be noted that, in real images,  $L$  is very likely to be higher than  $\log n$  leading to complexity of the order  $\mathcal{O}(nL^2)$  for the SUnSAL-TV algorithm.



## Chapter 4

# Hyperspectral Unmixing with Sparse Group Lasso and Collaborative Hierarchical Lasso

**Abstract** – Sparse unmixing has been introduced in this document as a mechanism to characterize mixed pixels in remotely sensed hyperspectral images. It assumes that the observed image signatures can be expressed in the form of linear combinations of a number of pure spectral signatures known in advance (e.g., spectra collected on the ground by a field spectroradiometer). Unmixing then amounts to finding the optimal subset of signatures in a (potentially very large) spectral library that can best model each mixed pixel in the scene. In available spectral libraries, it is observed that the spectral signatures appear organized in the form of groups (e.g. different alterations of a single mineral in the U.S. Geological Survey spectral library). On the other hand, in real images there are only a few endmembers present out of a very large library. In this chapter, we present two refinements of the sparse unmixing methodology which take advantage of the two aforementioned properties. First, we analyze the potential of the sparse group lasso technique to take advantage of the inherent group structure of available spectral libraries. Second, we study the impact of a so-called collaborative hierarchical sparse modeling framework in order to take advantage of the fact that only a few spectral endmembers should appear in a given scene. Our introspection is that, when the spectral signatures appear in groups, the Sparse Group Lasso technique has the potential to yield better results than the standard sparse regression approach. Further, the collaborative hierarchical lasso is able to improve the unmixing results by assuming that only a few endmembers will be likely present in the hyperspectral

image. Experimental results using both synthetic and real hyperspectral data sets are performed in order to confirm the aforementioned observations.

## 4.1 Introduction

Sparse linear regression [70], [39] has recently been introduced in hyperspectral unmixing [58] to circumvent the need to obtain image-derived endmembers, which is often a difficult and ill-posed problem. In sparse linear regression, the observed vectors (hyperspectral vectors) are approximated with a linear combination of a “small” number of regressors (spectral signatures). The regressors weights (fractional abundances) are obtained by minimizing an objective function, often containing a quadratic data term and a sparsity-inducing regularizer, usually the  $\ell_1$ -norm. If we recall the adopted formulation for the linear mixing model (LMM) in terms of a spectral library  $\mathbf{A}$ , we have the following expression:

$$\mathbf{y} = \mathbf{Ax} + \mathbf{n}, \quad (4.1)$$

where  $\mathbf{y}$  is the observed spectrum,  $\mathbf{x}$  is a vector of fractional abundances, and  $\mathbf{n}$  is a vector collecting the errors that affect the measurement process (e.g., noise). The model can be completed with the ANC and ASC constraints, as explained in detail in Chapter 2. Starting from these assumptions, the work presented in this chapter is focused on two main research directions which are described next:

1) In many hyperspectral applications, the linear combinations of spectral signatures tend to be organized in the form of groups. This is so either because not all combinations of materials are possible, or because the spectral library (the collection of spectral signatures) is built in order to account for variability. In the latter case, a single spectral signature may be replaced with a few slightly different ones such that small spectral variations can be modeled by linear combinations of these spectral signatures. In this work we are interested in the latter case. When the spectral signatures appear in groups, then the group lasso [96] and the sparse group lasso

[48] regression techniques have the potential to yield better results than the standard sparse regression approach, as the former methods enforce sparseness on the groups instead of the singleton variables.

2) On the other hand, a hyperspectral image always contains a small number of endmembers compared to the number of members present in the spectral library. This means that, if the fractional abundances of the library members are collected in a matrix with the number of columns equal to the number of pixels, there should be only a few lines with non-zero entries. In simple words, the non-zero abundance lines should appear in a few distinct lines, which implies the sparsity along the pixels. In this work, we use the collaborative hierarchical sparse modeling [88] in order to comply with this requirement.

With the above rationale in mind, the aim of this work is twofold: i) to illustrate the potential of the sparse group lasso technique [48] and of the collaborative hierarchical sparsity technique [88] in hyperspectral unmixing problems; ii) to introduce a new optimization algorithms to solve efficiently the convex optimization problem underlying the sparse group lasso regression technique. In order to test the collaborative sparsity technique, we will use an algorithm recently introduced by Bioucas-Dias and Figueiredo [11]. These algorithms constitute generalizations of the sparse unmixing by variable splitting and augmented Lagrangian (SUnSAL) introduced in [10]. Both SUnSAL and the two algorithms that we test in this work are instances of the methodology introduced in [3].

The remainder of the Chapter is organized as follows. Section 4.2 introduces the objective functions to minimize and the corresponding new algorithms. Section 4.3 shows a comparison between the new algorithms and previous ones with respect to their performances in simulated environments. Section 3.5 shows unmixing results obtained by the two algorithms in a real environment. The chapter ends with a section dedicated to conclusions and to pointers to the future work.

## 4.2 Algorithms

This section introduces the optimization functions to be solved and the two new corresponding algorithms.

### 4.2.1 Group Sparse Regression

Let assume that our library is a  $L \times m$  matrix which can be partitioned into  $G$  groups with  $m_i$  elements in the group  $i$ . The notations  $\mathbf{A}_i$  and  $\mathbf{x}_i$  denote, respectively, the spectral signatures and the fractional abundances corresponding to the group  $i$ . The groups do not overlap. With this notation in place, the sparse group lasso (SGL) criterion adapted to our problem is

$$\begin{aligned} \min_{\mathbf{x}} \quad & \left\| \mathbf{y} - \sum_{g=1}^G \mathbf{A}_g \mathbf{x}_g \right\|_2^2 + \lambda_G \sum_{g=1}^G \|\mathbf{x}_g\|_2 + \lambda_{1,G} \|\mathbf{x}\|_1, \\ \text{s.t:} \quad & \mathbf{x} \geq 0. \end{aligned} \quad (4.2)$$

where  $\lambda_G$  and  $\lambda_{1,G}$  are regularization parameters attached to the mixed  $\ell_{2,1}$  norm  $\sum_{g=1}^G \|\mathbf{x}_g\|_2$  and to the  $\ell_1$  norm  $\|\mathbf{x}\|_1$ , respectively. Compared with the sparse group lasso introduced in [48], we add the ANC. Accordingly, we designate the criterion (4.2) non-negative constrained sparse group lasso (NCSGL). Notice that the classical non-negative constrained least squares (NCLS) and the lasso subject to non-negativity, which we name non-negative constrained lasso (NCL) correspond, respectively, to setting  $(\lambda_G = 0, \lambda_{1,G} = 0)$  and  $(\lambda_G = 0, \lambda_{1,G} > 0)$ .

To solve the optimization problem (4.2), we use the group SUnSAL (GSUnSAL) algorithm which is an elaboration of the SUnSAL algorithm, introduced in [10]. GSUnSAL accounts for the  $\ell_{2,1}$  regularizer in addition to the  $\ell_1$  and the non-negativity regularizers. In fact, GSUnSAL is an instance of the methodology introduced in [3] for solving  $\ell_2$  plus a linear combination of convex regularizers, based on the alternative direction method of multipliers (ADMM) [44]. For libraries not larger than a few thousand spectral signatures, GSUnSAL is very fast because the linear systems that appear in the ADMM iterations are solved efficiently by pre-computing the inverse of the system matrix.



As a final note we emphasize that, by proper selection of the regularization parameters  $\lambda_G$  and  $\lambda_1$ , GSUnSAL can be used to solve not only NCSGL, but also NCLS and NCL optimization problems.

#### 4.2.2 Collaborative Hierarchical Sparse Regression

We keep, here, the same structure of the library  $\mathbf{A}$  as in subsection 4.2.1. As in Chapter 3, let  $\mathbf{X} \in \mathbb{R}^{m \times n}$  be the fractional abundances matrix; let  $\|\mathbf{X}\|_F \equiv \sqrt{\text{trace}\{\mathbf{X}\mathbf{X}^T\}}$  be the Frobenius norm of  $\mathbf{X}$ ; let  $\|\mathbf{X}\|_{1,1} \equiv \sum_{i=1}^n \|\mathbf{x}_i\|_1$  ( $\mathbf{x}_i$  denotes the  $i^{th}$  column of  $\mathbf{X}$ ) and  $\lambda_C$ ,  $\lambda_{1,C}$  regularization parameters. The collaborative hierarchical sparse regression (CHSR) approach can be written, for one pixel, as the following optimization problem:

$$\begin{aligned} \min_{\mathbf{X}} \quad & \left\| \mathbf{Y} - \sum_{g=1}^G \mathbf{A}_g \mathbf{X}_g \right\|_F^2 + \lambda_C \sum_{g=1}^G \|\mathbf{X}_g\|_F + \lambda_{1,C} \|\mathbf{X}\|_{1,1}, \\ \text{s.t:} \quad & \mathbf{x} \geq 0. \end{aligned} \quad (4.3)$$

where  $\mathbf{A}_g$  and  $\mathbf{X}_g$  denote the sub-matrix of  $\mathbf{A}$  containing the spectral signatures of the materials in group  $g$  and the fractional abundances corresponding to the same group, respectively (see Fig. 4.1 for a suggestive representation). Compared with the CHSR introduced in [88], we add the ANC. Accordingly, we designate the criterion (4.3) non-negative constrained collaborative hierarchical lasso (NCCHL). Notice that the classical non-negative constrained least squares (NCLS) and the collaborative lasso subject to non-negativity, which we name non-negative constrained hierarchical lasso (NCHL), respectively correspond to setting  $(\lambda_C = 0, \lambda_{1,C} = 0)$  and  $(\lambda_C > 0, \lambda_{1,C} = 0)$ .

To solve the optimization problem (4.3), we use the collaborative hierarchical SUnSAL (CHSUnSAL) algorithm [11] which is also an elaboration of the SUnSAL algorithm, introduced in [10]. CHSUnSAL accounts for the  $\ell_{2,1}$  regularizer in addition to the  $\ell_1$  and the non-negativity regularizers. As GSUnSAL, CHSUnSAL is an instance of the methodology introduced in [3] for solving  $\ell_2$  plus a linear combination of convex regularizers, based on the alternative direction

method of multipliers (ADMM) [44].

As a final note we emphasize that, by proper selection of the regularization parameters  $\lambda_C$  and  $\lambda_{1,C}$ , CHSUnSAL can be used to solve not only NCCHL, but also NCLS and NCHL optimization problems.

### 4.2.3 Short illustration of the regularization processes

This subsection is devoted to a graphical illustration of the action of the regularizers in Eq. 4.3 and 4.4, before inspecting results obtained in a simulated environment. The difference between the two regularizers is that the SGL acts over individual pixels and does not impose the homogeneity of the selected groups or members for all the pixels, while the CHSR constraints the solutions corresponding to different pixels to share the same active groups, as it acts along the pixels in the image. A suggestive graphical illustration of these differences is shown in Fig. 4.1.

As it can be seen in Fig. 4.1, both optimization problems 4.3 and 4.4 have the role of obtaining sparse solutions at individual and group level. Please note that SGL does not enforce homogeneity in the solutions of neighboring pixels, which means that two neighbors are allowed to have different active groups and/or members. On the other hand, CHL constraints the pixels to share the same active groups, but not necessarily the same active members. This means that two pixels which are neighbors can contain the same material with distinct signatures contained in the respective group.

## 4.3 Results with Synthetic Data

In this section we give an illustration of the performances of the two new unmixing approaches in a simulated environment. We will compare the results to the ones obtained with the SUnSAL algorithm, which solves the  $l_2 - l_1$  norm optimization problem. We use SUnSAL to infer the NCLS solution by setting  $\lambda = 0$ .

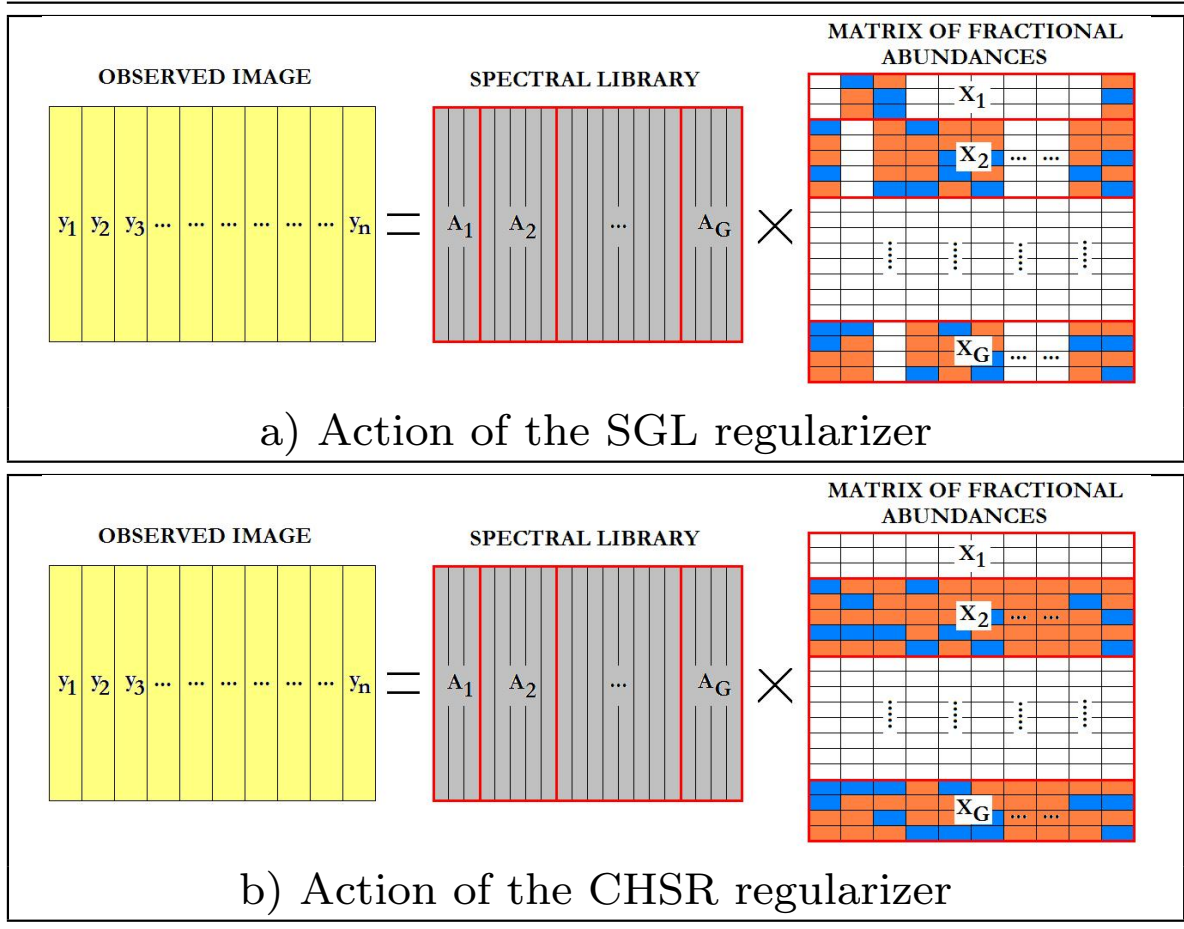


Figure 4.1: Graphical example of the actions of SGL and CHSR regularizers over the inferred abundance matrices; the colors have the following meaning: orange – active group, blue – active member, white – non-active groups.

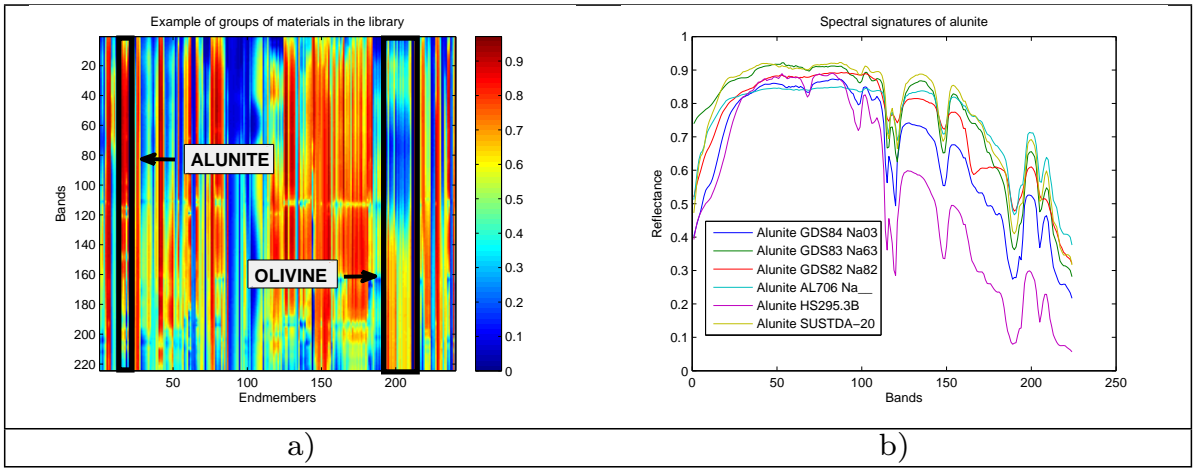


Figure 4.2: (a) The position of two material groups in library  $\mathbf{A}$  (delimited by black rectangles) and (b) example of different spectral signatures corresponding to the same material (alunite) included in one group

#### 4.3.1 Simulated datacubes

The library that we use in our experiments is a dictionary of minerals extracted from the USGS library, denoted by  $\mathbf{A}$ , with  $L = 224$  bands and  $m = 240$  members. The signatures are organized in  $G = 17$  groups, each group containing between one and 17 endmembers. The mutual coherence of the library is very close to one. As an example, we show, in Fig. 4.2, the position of two groups of materials in this library (see Fig. 4.2.[a]) and the spectral signatures corresponding to different variations of the same material (alunite) collected in one group (see Fig. 4.2.[b]). Using the library  $\mathbf{A}$ , we generated various datacubes of 500 pixels, each containing a different number of endmembers  $k$ :  $k_1 = 2$  (generically denoted by DC1),  $k_2 = 4$  (DC2) and  $k_3 = 6$  (DC3). The endmembers were randomly chosen from the library. In each pixel, the fractional abundances of the endmembers follow a Dirichlet distribution. From each group of materials, at most one endmember from each group is used for the generation of the images. The obtained datacubes were then contaminated both with i.i.d gaussian noise and correlated noise having different levels of the signal-to-noise ratio ( $\text{SNR}(\text{dB}) = \mathbb{E}\|\mathbf{A}\mathbf{f}\|^2 / \mathbb{E}\|\mathbf{n}\|^2$ ): 20, 30 and 40dB. Each noise level corresponds to different sets of endmembers.

The performance discriminators are the same ones described in subsection 2.4.2: the signal to reconstruction error:  $\text{SRE} \equiv E[\|\mathbf{x}\|_2^2] / E[\|\mathbf{x} - \hat{\mathbf{x}}\|_2^2]$ , measured in dB:  $\text{SRE}(\text{dB}) \equiv 10 \log_{10}(\text{SRE})$ ,

		SRE(dB) <i>per member</i>				$p_s$ <i>per member</i>			
		NCLS	SUnSAL	GSUnSAL	CHSUnSAL	NCLS	SUnSAL	GSUnSAL	CHSUnSAL
DC1 ( $k_1 = 2$ )	$SNR = 20dB$	0.69	2.37	3.05	4.85	0.16	0.18	0.24	0.44
	$SNR = 30dB$	7.75	8.76	9.05	11.48	0.8	0.8	0.82	1
	$SNR = 40dB$	16.80	18.22	18.23	21.47	1	1	1	1
DC2 ( $k_2 = 4$ )	$SNR = 20dB$	0.08	2.16	2.58	3.81	0.06	0.18	0.18	0.22
	$SNR = 30dB$	5.2	5.22	5.46	5.93	0.56	0.56	0.56	0.58
	$SNR = 40dB$	10.62	11.06	11.12	13.96	0.98	0.98	0.98	1
DC3 ( $k_3 = 6$ )	$SNR = 20dB$	-2.59	1.06	1.81	2.22	0.02	0.1	0.1	0.12
	$SNR = 30dB$	2.87	3.26	3.26	5.31	0.36	0.36	0.38	0.56
	$SNR = 40dB$	3.14	5.63	5.67	8.79	0.38	0.56	0.56	0.98

Table 4.1: Performance different unmixing algorithms *per member* when the observations are affected by white noise

		SRE(dB) <i>per group</i>				$p_s$ <i>per group</i>			
		NCLS	SUnSAL	GSUnSAL	CHSUnSAL	NCLS	SUnSAL	GSUnSAL	CHSUnSAL
DC1 ( $k_1 = 2$ )	$SNR = 20dB$	4.97	5.46	5.58	7.58	0.5	0.5	0.54	1
	$SNR = 30dB$	9.34	9.5	9.72	11.36	0.86	0.86	0.88	1
	$SNR = 40dB$	18.04	20.23	20.34	23.15	1	1	1	1
DC2 ( $k_2 = 4$ )	$SNR = 20dB$	2.79	3.48	3.61	4.89	0.1	0.24	0.26	0.3
	$SNR = 30dB$	6.21	6.05	6.05	6.89	0.62	0.64	0.64	0.74
	$SNR = 40dB$	15.2	15.28	15.92	17.14	1	1	1	1
DC3 ( $k_3 = 6$ )	$SNR = 20dB$	-2.00	2.89	3.24	4.64	0.04	0.16	0.26	0.28
	$SNR = 30dB$	5.9	6.84	6.84	7.95	0.66	0.74	0.74	0.82
	$SNR = 40dB$	3.97	6.91	6.96	9.52	0.5	0.8	0.82	0.98

Table 4.2: Performance different unmixing algorithms *per group* when the observations are affected by white noise

and the probability of success  $p_s \equiv P(\|\hat{x} - x\|^2 / \|x\|^2 \leq threshold)$ , where the considered threshold was set (as justified in previous chapters) to 5. In addition, we use the same discriminators applied for groups of materials, i.e. by considering that one group represents an endmember and the sum of the abundances of the group members represent the abundance of the respective endmember. Moreover, we count the non-zero inferred abundances in the two situations: per member (i.e., considering each member of the library as a potential endmember) and per group (i.e., considering each group of materials as a potential endmember). The unmixing problem is solved by NCLS, SUnSAL, GSUnSAL and CHSUnSAL. For all the algorithms, the parameters were carefully hand-tuned for optimal performance.

### 4.3.2 Performance in datasets affected by white noise

This subsection shows the performances of the algorithms when the observations are affected by white noise.

Table 4.1 shows the SRE(dB) and the  $p_s$  *per member* obtained in the datacubes, while Table 4.2 shows the same performance indicators computed *per group*.

		Average number of non-zero endmembers				Average number of non-zero groups			
		NCLS	SUnSAL	GSUnSAL	CHSUnSAL	NCLS	SUnSAL	GSUnSAL	CHSUnSAL
DC1 ( $k_1 = 2$ )	$SNR = 20dB$	60.1	42.64	18.36	12.6	19.86	16.4	11.32	10.6
	$SNR = 30dB$	40.8	37.5	17.72	11.63	13.82	13.48	9.06	8.63
	$SNR = 40dB$	30.8	37.5	17.72	9.62	11.98	11.9	8.26	8.12
DC2 ( $k_2 = 4$ )	$SNR = 20dB$	75.06	40.86	20.84	11.06	21.44	15.04	10.64	10.06
	$SNR = 30dB$	41.72	41.62	20.7	14.28	15.48	15.42	10.98	10.28
	$SNR = 40dB$	34.88	34.7	12.56	9.48	13.12	13.02	8.96	8.48
DC3 ( $k_3 = 6$ )	$SNR = 20dB$	92.66	39.56	18.56	11.96	23.3	14.94	9.9	9.46
	$SNR = 30dB$	43.74	31.76	12.5	9.68	14.84	12.44	8.26	8.18
	$SNR = 40dB$	40.82	26.32	10.18	8.2	14.4	10.46	6.06	6.02

Table 4.3: Average number of non-zero member and of non-zero group abundances when the observations are affected by white noise

From Tables 4.1 and 4.2, it can be seen that the CHSUnSAL technique outperforms the other techniques, both in terms of unmixing accuracy *per pixel* and per group. In other words, CHSUnSAL attains the highest SRE(dB) and  $p_s$  values in all the cases. GSUnSAL improves the performance of SUnSAL, especially in noisy scenarios. As expected, NCLS does not exhibit good performance. The accuracy of all algorithms decreases when the cardinality of the solution increases, which is in line with our observations in Chapter 2. This indicated that the sparsity of the solution mitigates the difficulties encountered in unmixing because of the high mutual coherence of the libraries. In all cases, the performance *per group* is superior to the one corresponding to individual endmembers.

Table 4.3 shows the average number of non-zero fractional abundances obtained by each algorithm when calculating the performance metrics reported in Tables 4.1 and 4.2, both for individual endmembers and for groups of materials (we will denote the fractional abundances larger than 0.001 by “non-zero abundances”, in order to avoid counting negligible values). From this table, we can see that, although in terms of SRE(dB) and  $p_s$  GSUnSAL did not improve dramatically the performance of SUnSAL, it uses less non-zero endmembers and group fractional abundances. In turn, NCLS provides solutions containing many non-zero entries, especially with high noise. Finally, CHSUnSAL not only provides the most accurate SRE(dB) and  $p_s$ , but also proves to be the algorithm with the sparsest solutions as it uses a low number of individual endmembers and groups to explain the data. Although GSUnSAL uses a higher number of individual endmembers to explain the data, the average number of groups, per pixel, is very close that of CHSUnSAL.

		SRE(dB) <i>per member</i>				$p_s$ <i>per member</i>			
		NCLS	SUnSAL	GSUnSAL	CHSUnSAL	NCLS	SUnSAL	GSUnSAL	CHSUnSAL
DC1 ( $k_1 = 2$ )	$SNR = 20dB$	2.87	5.92	6.13	9.95	0.32	0.74	0.74	0.98
	$SNR = 30dB$	6.18	6.78	6.79	10.69	0.74	0.8	0.8	1
	$SNR = 40dB$	12.27	12.51	15.1	15.9	0.98	0.98	1	1
DC2 ( $k_2 = 4$ )	$SNR = 20dB$	2.09	3.05	3.21	4.03	0.12	0.12	0.14	0.3
	$SNR = 30dB$	5.11	5.92	5.92	6.13	0.44	0.46	0.46	0.58
	$SNR = 40dB$	7.97	7.97	8.03	8.29	0.76	0.76	0.78	0.8
DC3 ( $k_3 = 6$ )	$SNR = 20dB$	1.68	2.07	2.12	2.88	0.12	0.12	0.12	0.14
	$SNR = 30dB$	2.5	4.37	4.48	7.28	0.3	0.38	0.4	0.76
	$SNR = 40dB$	6.2	6.11	8.4	9.59	0.7	0.72	0.92	1

Table 4.4: Performance of the algorithms *per member* when the observations are affected by correlated noise

		SRE(dB) <i>per group</i>				$p_s$ <i>per group</i>			
		NCLS	SUnSAL	GSUnSAL	CHSUnSAL	NCLS	SUnSAL	GSUnSAL	CHSUnSAL
DC1 ( $k_1 = 2$ )	$SNR = 20dB$	3.79	6.66	6.72	10.76	0.5	0.78	0.78	0.98
	$SNR = 30dB$	11.49	12.03	12.78	13.12	1	1	1	1
	$SNR = 40dB$	12.5	12.7	15.25	16.12	1	1	1	1
DC2 ( $k_2 = 4$ )	$SNR = 20dB$	3.09	3.39	3.41	5.27	0.22	0.22	0.22	0.4
	$SNR = 30dB$	5.29	6.45	6.46	6.48	0.58	0.72	0.72	0.72
	$SNR = 40dB$	8.46	8.53	8.59	10.98	1	1	1	1
DC3 ( $k_3 = 6$ )	$SNR = 20dB$	1.16	2.17	2.21	2.73	0.14	0.18	0.18	0.18
	$SNR = 30dB$	3	5.94	6.16	8.29	0.34	0.58	0.6	0.84
	$SNR = 40dB$	10.02	10.12	10.61	11.45	1	1	1	1

Table 4.5: Performance of the algorithms *per group* when the observations are affected by white noise

### 4.3.3 Performance in datasets affected by correlated noise

This subsection shows the performances of the algorithms when the observations are affected by correlated noise. This results from low-pass filtering i.i.d. Gaussian noise, using a normalized cut-off frequency of  $5\Pi/L$ . Table 4.4 shows the SRE(dB) and the  $p_s$  (*per member*) obtained in the datacubes affected by correlated noise, while Table 4.5 shows the same performance indicators computed *per group*.

From Tables 4.4 and 4.5, it can be seen that CHSUnSAL outperforms the other algorithms in terms of SRE(dB) and  $p_s$ , both computed *per member* and *per group*. This was already the case in the experiments reported with white noise. Again, the results provided by SUnSAL and GSUnSAL are generally similar, except in the scenarios dominated by low noise levels in which GSUnSAL is able to perform better, as it was already evidenced in the white noise cases. As expected, NCLS does not provide optimal performance although it shows high probabilities of success when the noise is low.

On the other hand, Table 4.6 shows the average number of non-zero members and groups used by each of the algorithms to attain the performance scores reported in Tables 4.4 and 4.5. From

		Average number of non-zero endmembers				Average number of non-zero groups			
		NCLS	SUnSAL	GSUnSAL	CHSUnSAL	NCLS	SUnSAL	GSUnSAL	CHSUnSAL
DC1 ( $k_1 = 2$ )	$SNR = 20dB$	76.48	17.54	8.22	9.5	20.9	10.5	7.22	7.04
	$SNR = 30dB$	17	16.54	9.28	9.3	10.44	8.98	8.4	8.22
	$SNR = 40dB$	17.28	17.14	9.36	9.4	10.14	9.5	8	7.8
DC2 ( $k_2 = 4$ )	$SNR = 20dB$	97.92	51.76	18.18	10.1	34.88	25.7	11.12	10.12
	$SNR = 30dB$	16.38	13.4	8.46	8.48	10.5	8.4	8	7.88
	$SNR = 40dB$	15.34	15.4	9.32	9.34	10.08	9.84	8.18	7.84
DC3 ( $k_3 = 6$ )	$SNR = 20dB$	66.68	17.22	9.24	9.26	18.4	10.34	7.38	7.14
	$SNR = 30dB$	33.72	20.82	11.4	11.38	13.76	12.6	10.26	9.64
	$SNR = 40dB$	15.7	15.66	8.62	8.64	10.94	10.48	8.1	7.84

Table 4.6: Average number of non-zero member and of non-zero group abundances when the observations are affected by correlated noise

this table, it can be seen that both GSUnSAL and CHSUnSAL use a much lower number of non-zero abundances than the other two algorithms. SUnSAL reduces significantly the cardinality of the solution compared to NCLS, but it still needs a larger number of members/groups to explain the observed data as compared to GSUnSAL and CHSUnSAL.

Finally, we show, in Fig. 4.3, a graphical comparison of the performances of the aforementioned algorithms, in a simulated datacube containing 50 pixels. The endmembers used to generate the datacube are randomly extracted from the library  $\mathbf{A}$ , their number is  $k = 4$ , and the datacube was contaminated with correlated noise having SNR=30dB. The algorithms were applied after tuning their corresponding parameters in order to obtain the most accurate solution for each of them. The abundance maps shown in Fig. 4.3 are in line with our previous observations. Note that GSUnSAL allows generally more endmembers from the same group (i.e., the abundance lines are not very clearly delimited, they seem to be "thicker", which means that neighboring members, from the same group, were selected, instead of the exact member), while CHSUnSAL produces more clear maps, as the pixels are constrained to share the same set of endmembers. Even visually, the superiority of CHSUnSAL with respect to the other algorithms is visible.

#### 4.3.4 Discussion

In this subsection, we tested the performances of the proposed algorithms in simulated environments. We considered observations affected by white noise, on the one hand, and by correlated noise, on the other. Our experiments revealed that the two methodologies analyzed in this



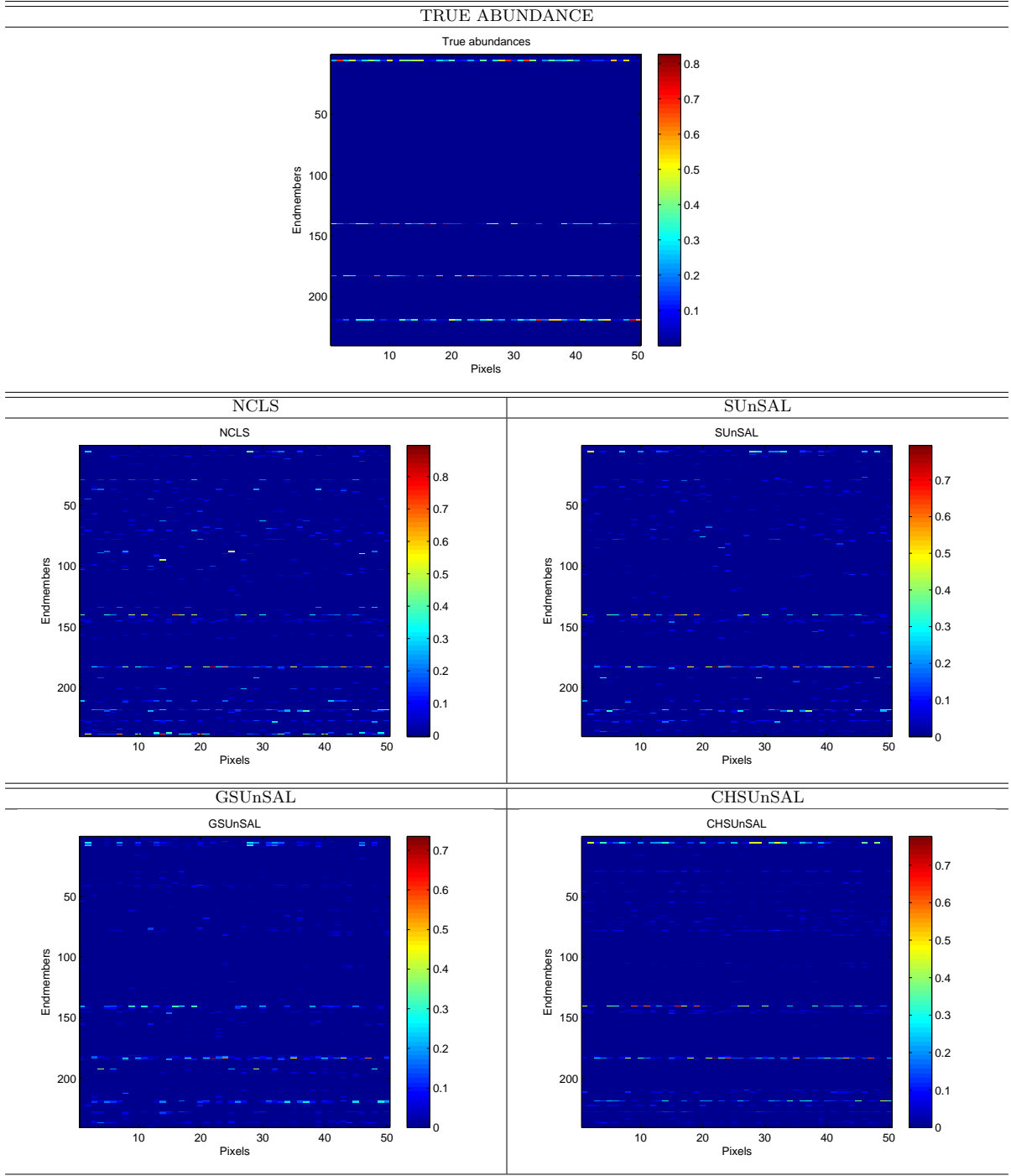


Figure 4.3: Abundance maps obtained by NCLS, SUnSAL, GUnSAL and CHSUnSAL in a toy datacube.

work (GSUnSAL and CHSUnSAL) improve significantly the cardinalities of the solutions by decreasing the number of non-zero components used to explain the observed data. Further, it is important to emphasize that GSUnSAL shows small improvements in terms of performance compared to SUnSAL, but CHSUnSAL improves significantly the accuracy over the aforementioned algorithms. In all cases, the performances are higher when entire groups of materials are considered as endmembers. This is a consequence of the fact that, due to the noise affecting the scenes, the algorithms are not always able to correctly identify the endmember. Instead, they often identify variations of the respective endmember present in the spectral library. The results obtained in this subsection are very encouraging, but further evaluation with real hyperspectral scenes is highly desirable. This will be accomplished in the following section.

## 4.4 Results with real data

The scene used in our real data experiments is the AVIRIS Cuprite<sup>1</sup> data set described in subsection 2.5. The portion used in experiments corresponds to a  $204 \times 151$ -pixel subset of the sector labeled as f970619t01p02\_r02\_sc03.a.rfi in the online data. The scene comprises 224 spectral bands between 0.4 and  $2.5 \mu\text{m}$ , with nominal spectral resolution of 10 nm. Prior to the analysis, bands 1–2, 105–115, 150–170, and 223–224 were removed due to water absorption and low SNR in those bands, leaving a total of 188 spectral bands. The spectral library used in this experiment is the library **A** used in the previous section, dedicated to simulated data. We remind that it was built using signatures from the USGS library<sup>2</sup> and it contains 240 materials (minerals) organized in 55 groups. Each group contains a number of spectra varying between 1 and 17. As for the considered image, we removed the (same) noisy bands prior to the unmixing process.

For comparative purposes, we use the Tetracorder 3.3 software product [34] described in subsection 2.5 of Chapter 2, which was used to map different minerals present in the Cuprite mining

---

<sup>1</sup><http://aviris.jpl.nasa.gov/html/aviris.freedata.html>

<sup>2</sup><http://speclab.cr.usgs.gov/spectral.lib06>

district<sup>3</sup>. We remind that the Tetracorder map is only available for hyperspectral data collected in 1995, while the publicly available AVIRIS Cuprite data was collected in 1997. Therefore, a direct comparison between the 1995 USGS map and the 1997 AVIRIS data is not possible. However, the USGS map serves as a good indicator for qualitative assessment.

Fig. 4.4 shows a qualitative comparison between the classification maps extracted from the Tetracorder map and the fractional abundances inferred by the proposed algorithms, GSUnSAL and CHSUnSAL in the considered image, for four different minerals (alunite, buddingtonite, chalcedony and montmorillonite). The parameters used in this experiment were empirically set to:  $\lambda_G = 0.05$ ,  $\lambda_{1,G} = 0.01$ ,  $\lambda_C = 0.001$  and  $\lambda_{1,C} = 0.001$ . As it can be seen in Fig. 4.4, the unmixing results show a good distribution of the minerals of interest. The fractional abundances obtained with GSUnSAL and CHSUnSAL are generally higher in the regions assigned to the respective materials. Additionally, we emphasize that the average number of endmembers with abundances higher than 0.05 (per pixel) in the unmixing results of GSUnSAL is 4.16, while the average number of groups with (total) abundances higher than 0.05 is 4.90. In the case of CHSUnSAL, the average number of endmembers with abundances higher than 0.05 is 5.07 (per pixel), while the average number of groups with total abundances higher than 0.05 is 5.53. The small difference between these two values is due to the fact that GSUnSAL and CHSUnSAL methods enforce the sparseness both at group and individual levels. This means that, inside the selected groups, the algorithm uses a minimum number of members to explain the data. This result is in line with the information provided by the Tetracorder classification map, in which the four selected endmembers are quite dominant in the scene. Overall, these qualitative endmembers indicate the possibilities that the newly developed algorithms GSUnSAL and CHSUnSAL provide when taking advantage of the special characteristics of available spectral libraries and hyperspectral images when conducting the sparse unmixing process.

---

<sup>3</sup>[http://speclab.cr.usgs.gov/PAPERS/tetracorder/FIGURES/fig9b.cuprite95.tgif.2.2um\\_map.gif](http://speclab.cr.usgs.gov/PAPERS/tetracorder/FIGURES/fig9b.cuprite95.tgif.2.2um_map.gif)

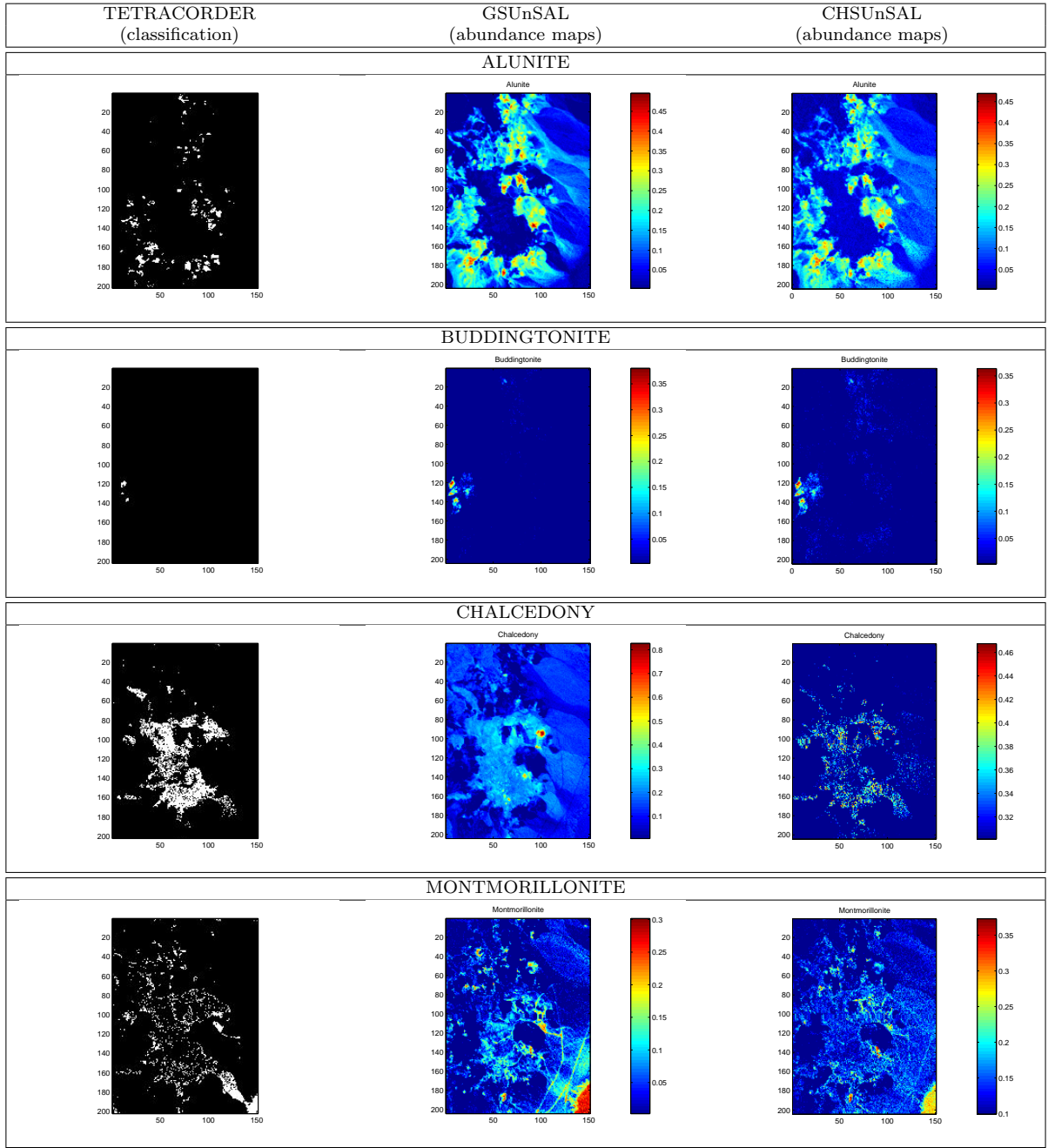


Figure 4.4: Qualitative comparison between the fractional abundance maps estimated by GSUnSAL and CHSUnSAL and the classification maps produced by USGS Tetracorder for the  $204 \times 151$ -pixel AVIRIS Cuprite scene.

## 4.5 Conclusions and future work

In this chapter, we gave experimental evidence of the potential of the sparse group lasso and collaborative hierarchical lasso techniques in solving sparse hyperspectral unmixing problems. The idea is to take advantage of the special characteristics of the spectral libraries and the hyperspectral data sets used in the process. On the one hand, spectral libraries are organized in the form of groups of materials, and this group structure can be inherently exploited in the unmixing process. On the other hand, the number of endmembers in a given hyperspectral scene is generally low. This fact can also be exploited in order to further refine sparse unmixing solutions. To exploit the inherent group structure of available spectral libraries we introduced GSUnSAL, a new algorithm to solve the NCGSL optimization problem. To exploit the fact that the number of endmembers in a given scene is generally low, we used the recently introduced algorithm CHSUnSAL, which solves the CHSR problem. The difference between the two algorithms is that GSUnSAL acts over individual pixels, while CHSUnSAL applies sparsity across the pixels. Both GSUnSAL and CHSUnSAL are able to infer with good accuracy the abundance fractions in simulated and real environments, concurrently decreasing the number of endmembers used to explain the data and providing more robust solutions by taking into account the group organization of the reference library used for unmixing purposes. Although the experimental results obtained in this chapter are very encouraging, further experimentation with additional hyperspectral scenes is needed in order to fully substantiate our contributions. Also, despite the fact that the algorithms are fast compared to other methods, a possible direction in our future research is the computationally efficient implementation of these algorithms on high performance computing infrastructure.



## Chapter 5

# Conclusions and Future Work

Spectral unmixing is an important technique in hyperspectral image exploitation. Available approaches for spectral unmixing are limited by the unavailability of pure spectral signatures in the hyperspectral image data, which prevents the commonly used linear mixture model to perform properly as the endmembers (pure spectral components) used by the model generally do not correspond to pure spectral signatures, and hence the abundance estimation based on such endmembers may not be accurate. In this thesis we have presented a new direction to address the unmixing problem in hyperspectral imaging. Our proposed approach is based on the use of (potentially very large) spectral libraries available *a priori*, which are collections of pure spectral signatures measured in the field or in a laboratory. In this context, we reformulate the unmixing as a sparse regression problem. Once this highly innovative framework is established, we derive new directions such as the incorporation of the spatial information contained in the hyperspectral image, or the consideration of the intrinsic group structure of the spectral libraries. Combined, these advances provide a completely innovative approach for spectral unmixing of hyperspectral data that represents a significant step forward with regards to existing approaches for the same purpose as it sidesteps most of the problems that have been traditionally associated to spectral unmixing of hyperspectral data. More specifically, the main developments of this innovative thesis work can be summarized as follows:

- First of all, we addressed the unmixing problem in a semi-supervised fashion, by relying on the use of large spectral libraries. This approach puts the unmixing problem under a new light, as it was never used before in the literature. Moreover, the use of spectral libraries

raises challenges related to their intrinsic mutual coherence, which is always very high in real scenarios, and to the different environments of acquisition (i.e., airborne/spaceborne hyperspectral sensors *versus* laboratory sensors). These difficulties were analyzed and there were developed solutions, in order to cope with them, in our work.

- Second, we have introduced the *sparse unmixing* methodology as a new standard in hyperspectral unmixing. Since 2008, when we introduced this idea in our community, many efforts have been devoted to this approach in the area, indicating the quick consolidation of this strategy in our community. As mixed pixels usually contain only a few endmembers compared to the number of spectral signatures contained in the (large) spectral library, we exploited this *sparse* characteristic of the mixtures by constraining the solutions to contain a large number of null abundances, i.e. to be also *sparse*, by solving optimization problems containing sparsity regularizers (e.g., the  $\ell_1$  norm).
- Another development achieved in the area is the introduction of fast sparse regression algorithms, based on the Alternating Direction Method of Multipliers (ADMM). These algorithms appeared as an important need in order to cope with the high computational complexity of the proposed methods, arising from the huge dimensionality of the hyperspectral data.
- Next, we exploited the rich spatial information offered by the hyperspectral images, by adding a Total Variation (TV) term, counting as a spatial regularizer, in the original objective function. We proposed a new fast algorithm, based on ADMM, called Sparse Unmixing by variable Splitting and Augmented Lagrangian with Total Variation (SUnSAL-TV), to solve the new optimization problem. Also, this new algorithm offers the possibility of choosing between two versions of the proposed TV regularizer: isotropic and non-isotropic. These versions have been inter-compared in our experiments.
- The next step in our developments was the exploitation of the intrinsic group structure of spectral libraries. These libraries usually contain many similar pure spectral signatures



(variants of the same material, including scalings), so they can be structured in groups of materials. In this case, the sparsity acts not only at individual (endmember) level, but also at group level. In this area, we proposed new objective functions derived from the original sparse formulation and based on the Sparse Group Lasso, to enforce the sparsity at group level. A new fast algorithm was developed in this sense, called Group Sparse Unmixing by variable Splitting and Augmented Lagrangian (GSUnSAL). On the other hand, we have also applied a recently introduced technique to impose sparsity across the pixels in the image (while accounting for the group structure of the spectral library) using the Collaborative Hierarchical Lasso: the new algorithm called Collaborative Hierarchical Sparse Unmixing by variable Splitting and Augmented Lagrangian (CHSUnSAL) [11].

- It is worth mentioning that, although the aforementioned techniques were developed with the idea of exploiting available spectral libraries of ground constituents, the proposed methods can also be applied when an *a priori* spectral library is not present. In other words, the proposed methods can also be applied after the traditional endmember extraction step conducted by many algorithms in the literature, so that the inferred endmembers can be collected in the form of a library and then the proposed strategies can be applied. An experiment has been also included in this thesis to support this observation, which enhances the applicability of the proposed sparse regression formulations in different contexts.
- Last, but not least, a very important contribution of the thesis is the introduction in the area of the fast algorithms based on the Alternating Direction Method of Multipliers. The hyperspectral applications raise problems related to the high dimensionality of the data and, often, the systems to be solved have a huge number of variables. The algorithms used and proposed in the thesis, based on the ADMM, are tailored to this type of applications and are able to deal with hundreds of thousands to tens of millions of variables, after splitting the original optimization problems in sub-problems easier to solve. This is a very important contribution to the area, as it opens new directions in the ability of dealing with such highly dimensional problems.

After describing the general contributions of the thesis, we detail here the developments achieved in each of the three main chapters:

- In Chapter 2, we reviewed the formulation of the unmixing problem, the methods already used in unmixing and the Linear Mixing Model (LMM) used to model the mixtures. Then, we have formulated the unmixing as a sparse regression problem, relying on the increasing availability of the spectral libraries. The problem to be solved appears, then, in the form of an  $\ell_1$  or  $\ell_2 - \ell_1$  norm optimization problem. The goal of this formulation is to avoid the endmember extraction step widely used in the literature, based on assumptions which are not always fulfilled in real environments: the presence of at least one pure pixel for each endmember present in the image, or the presence of at least one observed spectrum on each of the facets of the simplex generated by the points in the image. We presented also a detailed analysis of the difficulties encountered in the unmixing process when the spectral libraries are used, namely the high mutual coherence which characterize them (mitigated by the low cardinality of the solutions), the different environments of acquiring the data (for which we developed a simple method to cope with the mismatches between the pure signatures and the ones at sensor) and the appearance of non-smooth terms in the objective functions which leads to high computational complexity (solved by developing efficient sparse regression algorithms). An exhaustive performance comparison to the state-of-the-art methods proves the competitiveness and accuracy of the proposed methods. A test case which shows their performances when the library is formed by image-derived endmembers is also shown. Finally, the proposed methods were applied successfully in a real scenario, showing their ability to generate realistic and consistent abundance maps.
- In Chapter 3, we developed a methodology to consider the rich spatial information contained in the hyperspectral images in the sparse unmixing process. The original objective function was extended by including a Total Variation (TV) term, which accounts for spatial homogeneity. The algorithm developed in this sense, SUnSAL-TV, is based on the ADMM and all the iterative steps inside are detailed in an appendix. There were made

insightful observations regarding the complexity of the algorithm and the setting-up of the parameters. The algorithm proved his high performances both in simulated and real experiments. We included also a comparison between the actions of two types of TV regularizer over the sparse solutions: non-isotropic and isotropic. We concluded that both versions perform similarly in terms of accuracy, but there are qualitative differences in the solutions. The isotropic version allows the appearance of more regions of non-zero abundances, while the non-isotropic version has a strong vanishing action over small areas of non-zero abundances. While the non-isotropic TV regularizer offers a better delimitation of the abundance areas, the isotropic one preserves better small areas in which an endmember is present. Both quantitatively and qualitatively, the TV regularizer (in both versions) improve the sparse unmixing results.

- In Chapter 4 we developed a new methodology for sparse hyperspectral unmixing, this time taking into account the intrinsic structure of the spectral libraries. As the libraries usually contain many signatures corresponding to the same material (due to variability, scalability etc.), they can be structured in groups, each group corresponding to variants of the same material. In this case, the sparsity of the mixture does not refer anymore only to a certain material, but to all the variants of the respective material, i.e. to the groups of materials. To address this issue we have developed several new methods. The first one is based based on the Sparse Group Lasso and adds a new term to impose sparsity at group level. The new (fast) algorithm developed to solve the resulting objective function, GSUnSAL, is able to consider both specific members of the library and groups of materials when providing the final abundance estimation. In our simulated experiments, we showed that GSUnSAL reduces considerably the cardinality of the solutions, decreasing the estimation error. GSUnSAL was also successfully applied in real environments, showing a great potential to provide accurate abundance distributions. Another direction exploited in this chapter is based on the Collaborative Hierarchical Lasso. This method imposes sparsity across the pixels in the image and takes advantage of the characteristic group

structure of available spectral libraries. A new algorithm, CHSUnSAL, proposed recently by Bioucas-Dias and Figueiredo [11], has been successfully tested and proved to improve the cardinality of the unmixing solutions while exhibiting very good performance as compared to other state-of-the art methods.

All the aforementioned methods have been proved to be accurate and exhibit the potential to improve the state-of-the-art unmixing methods. However, although the developed (ADMM-based) optimizations can significantly improve their computational performance, their implementation in parallel computing environments will be considered in future developments in order to accelerate these algorithms even more. For instance, many research efforts are dedicated nowadays to the implementation of hyperspectral unmixing algorithms for fast performance in specialized hardware devices such as graphics processing units (GPUs) or field programmable gate arrays (FPGAs), which can be installed onboard hyperspectral imaging instruments. Moreover, as the accuracy of the under-determined systems of equations depend on the mutual coherence of the libraries, new methodologies to improve the sensitivity of the proposed methods to this issue are highly desirable and will also be explored in future developments.

# References

- [1] J. Adams, M. Smith, and P. Johnson. Spectral mixture modeling: a new analysis of rock and soil types at the Viking Lander 1 site. *Journal of Geophysical Research*, 91:8098–8112, 1986.
- [2] M. Afonso, J. Bioucas-Dias, and M. Figueiredo. A fast algorithm for the constrained formulation of compressive image reconstruction and other linear inverse problems. *IEEE International Conference on Acoustics, Speech, and Signal Processing - ICASSP'2010*, March. 2010.
- [3] M. Afonso, J. Bioucas-Dias, and M. Figueiredo. An augmented Lagrangian approach to the constrained optimization formulation of imaging inverse problems. *IEEE Transactions on Image Processing*, 20(3):681–695, 2011.
- [4] C. Bateson, G. Asner, and C. Wessman. Endmember bundles: a new approach to incorporating endmember variability into spectral mixture analysis. *IEEE Transactions on Geoscience and Remote Sensing*, 38(2 Part 2):1083–1094, 2000.
- [5] C. Bateson and B. Curtiss. A tool for manual endmember selection and spectral unmixing. *Remote Sensing of Environment*, pages 3–6, 1993.
- [6] C. Bateson and B. Curtiss. A method for manual endmember selection and spectral unmixing. *Remote Sensing of Environment*, 55(3):229–243, 1996.
- [7] M. Berman, H. Kiveri, R. Lagerstrom, A. Ernst, R. Dunne, and J. Huntington. ICE: a statistical approach to identifying endmembers in hyperspectral images. *IEEE Transactions on Geoscience and Remote Sensing*, 42(10):2085–2095, 2004.

- [8] J. Bioucas-Dias. A variable splitting augmented Lagrangian approach to linear spectral unmixing. *Hyperspectral Image and Signal Processing: Evolution in Remote Sensing, 2009. WHISPERS '09. First Workshop on*, pages 1–4, August 2009.
- [9] J. Bioucas-Dias. A variable splitting augmented Lagrangian approach to linear spectral unmixing. *Proceedings of the 1st IEEE Workshop on Hyperspectral Image and Signal Processing: Evolution in Remote Sensing (WHISPERS)*, pages 1–4, Grenoble, France, Aug. 26–28, 2009.
- [10] J. Bioucas-Dias and M. Figueiredo. Alternating direction algorithms for constrained sparse regression: application to hyperspectral unmixing. *2nd Workshop on Hyperspectral Image and Signal Processing: Evolution in Remote Sensing (WHISPERS)*, 2010.
- [11] J. Bioucas-Dias and M. Figueiredo. An alternating direction algorithm for collaborative hierarchical sparse regularization. *Technical Report, IST*, 2011.
- [12] J. Bioucas-Dias and J. Nascimento. Hyperspectral subspace identification. *IEEE Transactions on Geoscience and Remote Sensing*, 46(8):2435–2445, 2008.
- [13] J. Bioucas-Dias and J. Nascimento. Hyperspectral unmixing based on mixtures of Dirichlet components. *IEEE Transactions on Geoscience and Remote Sensing*, 2011, in press.
- [14] J. Boardman, F. Kruse, and R. Green. Mapping target signatures via partial unmixing of Aviris data. *Proc. JPL Airborne Earth Science Workshop*, pages 23–26, 1995.
- [15] C. Borel and S. Gerstl. Nonlinear spectral mixing model for vegetative and soil surfaces. *Remote Sensing of Environment*, 47(3):403–416, 1994.
- [16] J. Bowles, P. Palmadesso, J. Antoniadis, M. Baumback, and L. Rickard. Use of filter vectors in hyperspectral data analysis. *Proc. SPIE Infrared Spaceborne Remote Sensing III*, 2553:148–157, 1995.
- [17] A. Bruckstein, D. Donoho, and M. Elad. From sparse solutions of systems of equations to sparse modeling of signals and images. *SIAM Review*, 51:34–81, 2009.

- [18] A. Bruckstein, M. Elad, and M. Zibulevsky. On the uniqueness of nonnegative sparse solutions to underdetermined systems of equations. *Information Theory, IEEE Transactions on*, 54(11):4813–4820, 2008.
- [19] E. Candès, J. Romberg, and T. Tao. Stable signal recovery from incomplete and inaccurate measurements. *Communications on Pure and Applied Mathematics*, 59(8):1207, 2006.
- [20] E. Candès and T. Tao. Decoding by linear programming. *IEEE Transactions on Information Theory*, 51(12):4203–4215, 2005.
- [21] A. Chambolle. An algorithm for total variation minimization and applications. *Journal of Mathematical Imaging and Vision*, 20:89–97, 2004.
- [22] A. Chambolle. Total variation minimization and a class of binary MRF models. *Proc. Int. Workshop on Energy Minimization Methods in Computer Vision and Pattern Recognition*, pages 136–152, Springer Verlag, 2005.
- [23] T.-H. Chan, C.-Y. Chi, Y.-M. Huang, and W.-K. Ma. A convex analysis-based minimum-volume enclosing simplex algorithm for hyperspectral unmixing. *IEEE Transactions on Signal Processing*, 57:4418–4432, 2009.
- [24] C.-I. Chang. *Hyperspectral imaging: techniques for spectral detection and classification*. Kluwer Academic/Plenum Publishers: New York, 2003.
- [25] C.-I. Chang and Q. Du. Estimation of number of spectrally distinct signal sources in hyperspectral imagery. *IEEE Transactions on Geoscience and Remote Sensing*, 42(3):608–619, 2004.
- [26] C.-I. Chang and D. Heinz. Constrained subpixel target detection for remotely sensed imagery. *IEEE Transactions on Geoscience and Remote Sensing*, 38:1144–1159, 2000.
- [27] C.-I. Chang and A. Plaza. A fast iterative algorithm for implementation of pixel purity index. *IEEE Geoscience and Remote Sensing Letters*, 3(1):63–67, 2006.

- [28] C.-I. Chang, C.-C. Wu, and H.-M. Chen. Random pixel purity index. *IEEE Geoscience and Remote Sensing Letters*, 7(2):324–328, 2010.
- [29] C.-I. Chang, C.-C. Wu, W. Liu, and Y.-C. Ouyang. A new growing method for simplex-based endmember extraction algorithm. *IEEE Transactions on Geoscience and Remote Sensing*, 44(10):2804–2819, 2006.
- [30] C.-I. Chang, C.-C. Wu, C.-S. Lo, and M.-L. Chang. Real-time simplex growing algorithms for hyperspectral endmember extraction. *IEEE Transactions on Geoscience and Remote Sensing*, 48(4):1834–1850, 2010.
- [31] J. Chen, X. Jia, W. Yang, and B. Matsushita. Generalization of subpixel analysis for hyperspectral data with flexibility in spectral similarity measures. *IEEE Transactions on Geoscience and Remote Sensing*, 47(7):2165–2171, 2009.
- [32] S. Chen, D. Donoho, and M. Saunders. Atomic decomposition by basis pursuit. *SIAM review*, 43(1):129–159, 2001.
- [33] X. Chen, J. Chen, X. Jia, B. Somers, J. Wu, and P. Coppin. A quantitative analysis of virtual endmembers’ increased impact on the collinearity effect in spectral unmixing. *IEEE Transactions on Geoscience and Remote Sensing*, 49(8):2945–2956, 2011.
- [34] R. Clark, G. Swayze, K. Livo, R. Kokaly, S. Sutley, J. Dalton, R. McDougal, and C. Gent. Imaging spectroscopy: Earth and planetary remote sensing with the USGS Tetracorder and expert systems. *Journal of Geophysical Research*, 108 [E12], 5131, 2003.
- [35] P. Combettes and V. Wajs. Signal recovery by proximal forward-backward splitting. *SIAM J. Multiscale Model*, pages 1168–1200, 2005.
- [36] M. Craig. Minimum-volume transforms for remotely sensed data. *IEEE Transactions on Geoscience and Remote Sensing*, 32:542–552, 1994.
- [37] P. Dennison and D. Roberts. Endmember selection for multiple endmember spectral mix-



- ture analysis using endmember average RMSE. *Remote Sensing of Environment*, 87:123–135, 2003.
- [38] D. Donoho and M. Elad. Optimal sparse representation in general (non-orthogonal) dictionaries via  $l_1$  minimization. *Proceedings of the National Academy of Sciences*, 100:2197–2202, 2003.
- [39] D. Donoho, M. Elad, and V. Temlyakov. Stable recovery of sparse overcomplete representations in the presence of noise. *IEEE Transactions on Information Theory*, 52(1):6–18, 2006.
- [40] S. Dowler and M. Andrews. On the convergence of N-FINDR and related algorithms: to iterate or not to iterate? *IEEE Geoscience and Remote Sensing Letters*, 8(1):4–8, 2011.
- [41] Q. Du, N. Raksuntorn, N. Younan, and R. King. End-member extraction for hyperspectral image analysis. *Applied Optics*, 47:77–84, 2008.
- [42] Q. Du, H. Ren, and C.-I. Chang. A comparative study for orthogonal subspace projection and constrained energy minimization. *IEEE Transactions on Geoscience and Remote Sensing*, 41(6):1525–1529, 2003.
- [43] O. Duran and M. Petrou. Robust endmember extraction in the presence of anomalies. *IEEE Transactions on Geoscience and Remote Sensing*, 49(6):1986–1996, 2011.
- [44] J. Eckstein and D. Bertsekas. On the DouglasRachford splitting method and the proximal point algorithm for maximal monotone operators. *Mathematical Programming*, 5:293–318, 1992.
- [45] E. Esser. Applications of Lagrangian-based alternating direction methods and connections to split-Bregman. Technical Report 09-31, Univ. California, 2009.
- [46] M. Figueiredo, J. Bioucas-Dias, and M. Afonso. Fast frame-based image deconvolution using variable splitting and constrained optimization. Cardiff, Wales, 2009.

- [47] S. Foucart and M. Lai. Sparsest solutions of underdetermined linear systems via  $\ell_q$ -minimization for  $0 < q < 1$ . *Applied and Computational Harmonic Analysis*, 26(3):395–407, 2009.
- [48] J. Friedman, T. Hastie, and R. Tibshirani. A note on the group Lasso and a sparse group Lasso. *arXiv:1001.0736v1 [math.ST]*, 2010.
- [49] A. Goetz, G. Vane, J. Solomon, and B. Rock. Imaging spectrometry for Earth remote sensing. *Science*, 228:1147–1153, 1985.
- [50] I. Gorodnitsky and B. Rao. Sparse signal reconstruction from limited data using FO-CUSS: A re-weighted minimum norm algorithm. *IEEE Transactions on Signal Processing*, 45(3):600–616, 1997.
- [51] A. Green, M. Berman, P. Switzer, and M. Craig. A transformation for ordering multispectral data in terms of image quality with implications for noise removal. *IEEE Transactions on Geoscience and Remote Sensing*, 26:65–74, 1988.
- [52] R. Green, M. Eastwood, C. Sarture, T. Chrien, M. Aronsson, B. Chippendale, J. Faust, B. Pavri, C. Chovit, M. Solis, et al. Imaging spectroscopy and the airborne visible/infrared imaging spectrometer (AVIRIS). *Remote Sensing of Environment*, 65(3):227–248, 1998.
- [53] Z. Guo, T. Wittman, and S. Osher. L1 unmixing and its application to hyperspectral image enhancement. *Proceedings of SPIE Conference on Algorithms and Technologies for Multispectral, Hyperspectral, and Ultraspectral Imagery XV, Orlando, Florida*, 7334:73341–73449, 2009.
- [54] J. Harsanyi and C.-I. Chang. Hyperspectral image classification and dimensionality reduction: an orthogonal subspace projection. *IEEE Transactions on Geoscience and Remote Sensing*, 32(4):779–785, 1994.
- [55] D.C. Heinz and C.-I. Chang. Fully constrained least squares linear mixture analysis for material quantification in hyperspectral imagery. *IEEE Trans. on Geoscience and Remote Sensing*, 39:529–545, 2001.

- [56] A. Ifarraguerri and C.-I. Chang. Multispectral and hyperspectral image analysis with convex cones. *IEEE Transactions on Geoscience and Remote Sensing*, 37(2):756–770, 1999.
- [57] D. Iordache, J. Bioucas-Dias, and A. Plaza. Hyperspectral unmixing with Sparse Group Lasso. *IEEE International Geoscience and Remote Sensing Symposium IGARSS2011, Vancouver, Canada*, 2011.
- [58] D. Iordache, J. Bioucas-Dias, and A. Plaza. Sparse unmixing of hyperspectral data. *IEEE Transactions on Geoscience and Remote Sensing*, 49(6):2014–2039, 2011.
- [59] D. Iordache, J. Bioucas-Dias, and A. Plaza. Total variation spatial regularization for sparse hyperspectral unmixing. *IEEE Transactions on Geoscience and Remote Sensing*, 2011 (submitted).
- [60] S. Jia and Y. Qian. Spectral and spatial complexity-based hyperspectral unmixing. *IEEE Transactions on Geoscience and Remote Sensing*, 45:3867–3879, 2007.
- [61] N. Keshava and J. Mustard. Spectral unmixing. *IEEE Signal Processing Magazine*, 19(1):44–57, 2002.
- [62] D. Landgrebe. *Signal theory methods in multispectral remote sensing*. John Wiley & Sons: New York, 2003.
- [63] J. Li and J. Bioucas-Dias. Minimum volume simplex analysis: a fast algorithm to unmix hyperspectral data. volume 3, pages 250–253, july 2008.
- [64] W. Liu and E. Wu. Comparison of non-linear mixture models. *Remote Sensing of Environment*, 18:1976–2003, 2004.
- [65] G. Martin and A. Plaza. Region-based spatial preprocessing for endmember extraction and spectral unmixing. *IEEE Geoscience and Remote Sensing Letters*, 8:745–749, 2011.

- [66] S. Mei, M. He, Z. Wang, and D. Feng. Spatial purity based endmember extraction for spectral mixture analysis. *IEEE Transactions on Geoscience and Remote Sensing*, 48(9):3434–3445, 2010.
- [67] L. Miao and H. Qi. Endmember extraction from highly mixed data using minimum volume constrained nonnegative matrix factorization. *IEEE Transactions on Geoscience and Remote Sensing*, 45:765–777, 2007.
- [68] J. Nascimento and J. Bioucas-Dias. Does independent component analysis play a role in unmixing hyperspectral data? *IEEE Transactions on Geoscience and Remote Sensing*, 43(1):175–187, 2005.
- [69] J. Nascimento and J. Bioucas-Dias. Vertex component analysis: a fast algorithm to unmix hyperspectral data. *IEEE Transactions on Geoscience and Remote Sensing*, 43(4):898–910, 2005.
- [70] B. Natarajan. Sparse approximate solutions to linear systems. *SIAM journal on computing*, 24(2):227–234, 1995.
- [71] R. Neville, K. Staenz, T. Szeredi, J. Lefebvre, and P. Hauff. Automatic endmember extraction from hyperspectral data for mineral exploration. *Proc. 21st Canadian Symp. Remote Sens.*, pages 21–24, 1999.
- [72] Y. Pati, R. Rezaifar, and P. Krishnaprasad. Orthogonal matching pursuit: recursive function approximation with applications to wavelet decomposition. *Proceedings of the 27th Annual Asilomar Conference on Signals, Systems and Computers*, Los Alamitos, CA, USA, 2003.
- [73] A. Plaza, J. Benediktsson, J. Boardman, J. Brazile, L. Bruzzone, G. Camps-Valls, J. Chanussot, M. Fauvel, P. Gamba, A. Gualtieri, M. Marconcini, J. Tilton, and G. Trianni. Recent advances in techniques for hyperspectral image processing. *Remote Sensing of Environment*, 113:110–122, September 2009.

- [74] A. Plaza and C.-I. Chang. Impact of initialization on design of endmember extraction algorithms. *IEEE Transactions on Geoscience and Remote Sensing*, 44(11):3397–3407, 2006.
- [75] A. Plaza, G. Martin, J. Plaza, M. Zortea, and S. Sanchez. Recent developments in spectral unmixing and endmember extraction. In S. Prasad, L. M. Bruce, and J. Chanussot, editors, *Optical Remote Sensing*, chapter 12, pages 235–267. Springer-Verlag, Berlin, Germany, 2011.
- [76] A. Plaza, P. Martinez, R. Perez, and J. Plaza. Spatial/spectral endmember extraction by multidimensional morphological operations. *IEEE Transactions on Geoscience and Remote Sensing*, 40(9):2025–2041, 2002.
- [77] A. Plaza, P. Martinez, R. Perez, and J. Plaza. A quantitative and comparative analysis of endmember extraction algorithms from hyperspectral data. *IEEE Transactions on Geoscience and Remote Sensing*, 42(3):650–663, 2004.
- [78] N. Raksuntorn and Q. Du. Nonlinear spectral mixture analysis for hyperspectral imagery in an unknown environment. *IEEE Geoscience and Remote Sensing Letters*, 7(4):836–840, 2010.
- [79] H. Ren and C.-I. Chang. Automatic spectral target recognition in hyperspectral imagery. *IEEE Transactions on Aerospace and Electronic Systems*, 39(4):1232–1249, 2003.
- [80] D. Rogge, B. Rivard, J. Zhang, and J. Feng. Iterative spectral unmixing for optimizing per-pixel endmember sets. *IEEE Transactions on Geoscience and Remote Sensing*, 44(12):3725–3736, 2006.
- [81] D. Rogge, B. Rivard, J. Zhang, A. Sanchez, J. Harris, and J. Feng. Integration of spatial–spectral information for the improved extraction of endmembers. *Remote Sensing of Environment*, 110(3):287–303, 2007.

- [82] L. Rudin, S. Osher, and E. Fatemi. Nonlinear total variation based noise removal algorithms. *Physica D: Nonlinear Phenomena*, 60(1-4):259–268, 1992.
- [83] F. Schmidt, A. Schmidt, E. Treandguier, M. Guiheneuf, S. Moussaoui, and N. Dobigeon. Implementation strategies for hyperspectral unmixing using Bayesian source separation. *IEEE Transactions on Geoscience and Remote Sensing*, 48(11):4003–4013, 2010.
- [84] J. Settle. On the effect of variable endmember spectra in the linear mixture model. *IEEE Transactions on Geoscience and Remote Sensing*, 44:389–396, 2006.
- [85] J.J. Settle and N.A. Drake. Linear mixing and the estimation of ground cover proportions. *International Journal of Remote Sensing*, 14:1159–1177, 1993.
- [86] M. Shoshany, F. Kizel, N. Netanyahu, N. Goldshlager, T. Jarmer, and G. Even-Tzur. An iterative search in end-member fraction space for spectral unmixing. *IEEE Geoscience and Remote Sensing Letters*, 8(4):706–709, 2011.
- [87] B. Somers, G. Asner, L. Tits, and P. Coppin. Endmember variability in spectral mixture analysis: a review. *Remote Sensing of Environment*, 115(7):1603–1616, 2011.
- [88] P. Sprechmann, I. Ramirez, G. Sapiro, and Y. Eldar. C-hilasso: a collaborative hierarchical sparse modeling framework. *IEEE Transactions on Signal Processing*, 59(9):4183–4198, September 2011.
- [89] X. Tao, B. Wang, and L. Zhang. Orthogonal bases approach for the decomposition of mixed pixels in hyperspectral imagery. *IEEE Geoscience and Remote Sensing Letters*, 6:219–223, 2009.
- [90] D. Thompson, L. Mandrake, M. Gilmore, and R. Castano. Superpixel endmember detection. *IEEE Transactions on Geoscience and Remote Sensing*, 48(11):4023–4033, 2010.
- [91] J. Tropp. Just relax: convex programming methods for subset selection and sparse approximation. *ICES report*, pages 04–04, 2004.

- [92] J. Tropp and A. Gilbert. Signal recovery from random measurements via orthogonal matching pursuit. *IEEE Transactions on Information Theory*, 53(12):4655, 2007.
- [93] J. Wang and C.-I. Chang. Applications of independent component analysis in endmember extraction and abundance quantification for hyperspectral imagery. *IEEE Transactions on Geoscience and Remote Sensing*, 44(9):2601–2616, 2006.
- [94] L. Wang and X. Jia. Integration of soft and hard classifications using extended support vector machines. *IEEE Geoscience and Remote Sensing Letters*, 6:543–547, 2009.
- [95] M. Winter. N-FINDR: An algorithm for fast autonomous spectral endmember determination in hyperspectral data. *Proceedings of SPIE*, 3753:266–277, 1999.
- [96] M. Yuan and M. Lin. Model selection and estimation in regression with grouped variables. *Journal of the Royal Statistical Society: Series B*, 68(1):49–67, 2006.
- [97] A. Zare and P. Gader. Sparsity promoting iterated constrained endmember detection for hyperspectral imagery. *IEEE Geoscience and Remote Sensing Letters*, 4(3):446–450, 2007.
- [98] A. Zare and P. Gader. Hyperspectral band selection and endmember detection using sparsity promoting priors. *IEEE Geoscience and Remote Sensing Letters*, 5(2):256–260, 2008.
- [99] A. Zare and P. Gader. PCE: Piecewise convex endmember detection. *IEEE Transactions on Geoscience and Remote Sensing*, 48(6):2620–2632, 2010.
- [100] M. Zortea and A. Plaza. A quantitative and comparative analysis of different implementations of N-FINDR: a fast endmember extraction algorithm. *IEEE Geoscience and Remote Sensing Letters*, 6:787–791, 2009.
- [101] M. Zortea and A. Plaza. Spatial preprocessing for endmember extraction. *IEEE Transactions on Geoscience and Remote Sensing*, 47:2679–2693, 2009.

- [102] A. Zymnis, S. Kim, J. Skaf, M. Parente, and S. Boyd. Hyperspectral image unmixing via alternating projected subgradients. *Proc. Asilomar Conference on Signals, Systems and Computers*, pages 1164–1168, 2008.